NORTHWESTERN UNIVERSITY

Charge Transport across Single Grain Boundaries in Oxide Electrolytes

A DISSERTATION

SUBMITTED TO THE GRADUATE SCHOOL

IN PARTIAL FULFILLMENT OF THE REQUIREMENTS

for the degree

DOCTOR OF PHILOSOPHY

Field of Applied Physics

By

Xin Xu

EVANSTON, ILLINOIS

September 2019

Abstract

Transport along and across the grain boundaries of solid-state electrolytes has implications for a broad range of materials and in an equally broad range of technologies. Over the past 2-3 decades, a substantial body of literature has been developed to explain grain boundary transport properties within the context of space charge theory. This theory holds that the grain boundaries in ionic materials are inherently charged due to the difference in energetics between creating point defects in the bulk and at their interface surfaces. While generally effective at predicting material properties, two aspects of this approach have remained unsatisfactory. The first is the assumption that every grain boundary is approximately the same, with the same level of grain boundary charge imbalance (which generates a space charge potential of given magnitude), and the second is the difficulty in fundamentally predicting why a charge imbalance occurs. In this study we employ electron holography to study several individual/isolated grain boundaries in lightly doped, high-purity ceria. We find a remarkable variation in the electric field perturbation from one grain boundary to the next, suggesting orders of magnitude differences in the transport properties. Similarly, 3 orders of difference are observed in grain boundary conductivity by impedance measurement on single grain boundaries in ceria fibers. Using atom probe tomography (APT) and secondary ion mass spectroscopy, we are able to identify the chemical nature of essentially every atom in the grain boundary region. Here we find that trace impurities, < 25 ppm Si and Al, are concentrated at the grain boundary core, and are the apparent cause of the interfacial charge. These tetra and trivalent species, located within interstitial sites, generate a positive charge at the interface that is balanced by a depletion of oxygen vacancies in the neighboring space charge zone, in a manner analogous to conventional space charge theory. The APT studies further reveal that the

dopant element, Sm, is enhanced in the grain boundaries, which has the effect of screening the impurity charge. Our definitive demonstration of the origins of the space charge effect in ceria provides clear guidance on how to tune interfacial charge transport at will. Our work further clarifies why introduction of alkaline earth dopants or simply increasing the concentration of conventional rare earth element dopants so dramatically increases the grain boundary ionic conductivity.

Acknowledgements

First and foremost, I would like to thank my advisor Prof. Sossina Haile for having me in the group and continuous guidance in the past five years. She is a wonderful and knowledgeable mentor, teacher and friend not only in the research but in daily life. Without her kind help, I wouldn't have survived my PhD. Now I am very proud to be her first Northwestern PhD! I would also like to thank my supervisor Dr. Charudatta Phatak at Argonne National Laboratory. He is very intelligent and responsive to help me get through those experimental difficulties at Argonne. I would thank Prof. Vinayak P. Dravid and Prof. Scott Barnett as members of my proposal and defense committee. They provide very insightful ideas to guide my research. I acknowledge the funding resources for this work from the National Science Foundation under Grant No. DMR-1720139, and by the Northwestern-Argonne Early Career Investigator Award for Energy Research.

I would thank my collaborators and coauthors Dr. Yuzi Liu for his ample experience on electron holography, Jie (Joyce) Wang for the kind help on TEM-EDX, Frank Barrows for in-situ electron holography and simulation work, Dr. Dieter Isheim for professional knowledge about atom probe tomography, Dr. Xinqi Chen for the guidance on secondary ion mass spectroscopy, Dr. Bruce Buchholz for pulsed laser deposition and Dr. Benjamin Daniel Myers for focused ion beam.

I acknowledge and thank so many people who have provide technical support to my research. I thank the team of NUANCE who are Prof. Jinsong Wu (TEM Characterization), Wenyun Li (TEM sample preparation), Karl Hagglund (EBSD), Eric Miller (SEM), Tirzah Abbott (Thermal Sputtering) and the team of NUFAB who are Dr. Nasir Basit (Wet etching), Dr. Ying Jia

(Photolithography and general help), Dr. Serkan Butun (Photolithography), Dr. Anil Dhote (E-beam deposition) and John Ciraldo (Sputtering Deposition).

I am grateful to my research group who have supported me both experimentally and mentally along the way. Prof. Sihyuk Choi taught me a lot about ceramics sample synthesis especially those valuable experience summarized from many years' research. Dr. Chris Kucharczyk was very warmhearted, and he put the lab in a very organized way. Whenever I was stuck in my experiments and talked to him, he could contribute many ideas. Dr. HoIl Ji was patient, kind and had a very good sense of humor. I really enjoyed the time talking with him. Dr. Haemin Paik was a very supportive friend. Whenever I felt bad about my research and talked to her, I always received much encouragement and felt better. Dr. Xinbing Chen was my office mate. But he was more like an older brother to me. He helped me a lot even though we only spent one year together. I couldn't forget those valuable time when we worked together, sometimes till very late night. Dr. Timothy Davenport was an expert on thermochemical properties on ceria and he answered all my questions about ceria. Austin Plymill sat next to me in the office and became my daily English teacher (I also taught him some cool Chinese words as a return favor!). Whenever I had some difficult in understanding about emails or articles, he was always there (thank you bro!). I thank Sheel Sanghvi and Dr. Jill K. Wenderott for helping me edit the thesis. I know that I am not a native speaker but with their help I feel more confident. I thank Connor Carr for the discussion on ceria grain boundary. He was the only one in the group who might carry on my research topic in the future. We all know it is not easy and I wish him the best luck and fruitful results in the future. I thank my beloved office mates and life-long good friends Ruiyun Huang,

Weizi Yuan, Xin Qian and Shobhit Pandey for so many beautiful memories and fun time together. Your support and accompany made me feel the PhD life much more valuable.

I own a great deal of gratitude to the individuals who have taken care of me, shaped my career, and still mentoring me now. I thank Prof. Seungbum Hong who I was fortunate to meet at Argonne. His knowledge and spirits impressed and inspired me till now. I thank Dr. Mark Pucci for having me as an extern in his company when I learnt from him about career development. I thank Erin Leddon for teaching, improving and encouraging me on spoken English. I thank Dr. Charlie Chen and Dr. Amy Cui for their thoughtful care and mentoring from 5 year ago until now, never stop. I thank Wenfang (Monica) Shi for her tutoring on English, and endless support and encouragement to help me get through the most difficult time.

I would thank the team of Northwestern Werewolves Club who are Mingzheng Wu, Chenyang Li, Yiding Feng, Jinghe Zhang, Yangzi Jiang, Haishan (Sally) Gao, Wenyuan (Tony) Huang. Without you we couldn't have achieved so much in club development. We are happy to see Werewolves Club are helping more and more students at Northwestern and I give my best wishes to all of you and the future of the club.

I was lucky to have entered Nanjing University with a world-class physics department. I can never forget the knowledge and the experience which prepared me into a scientist. I thank my undergraduate advisor Prof. Hui Liu and Dr. Shuming Wang for guiding me to taste the first joy of research. I would specially thank Xueli (Shirley) Wang who was my spoken English teacher when I was fourth year. She gave me big support and encouragement to my English study. I still remember she was willing to give me extra tutoring after class which really helped me pass standard tests. I won't forget her kindness.

Finally, I would thank my parents and my younger sister. You are the biggest comfort behind me. It's you that give me a happy home and I promise to be with you forever. I would always cherish the sweet memories with Grandma and Grandpa and remember their love. May them have a happy life in the heaven and be together from now on to forever.

List of Symbols & Notations

$O_O^{\times}$	neutral oxygen atom at oxygen site in the Kröger-Vink notation
$V_O^{\cdot\cdot}$	oxygen vacancy in the Kröger-Vink notation
Sm'_{Ce}	dopant Sm sitting at Ce site in the Kröger-Vink notation
Ca''_{Ce}	dopant Ca sitting at Ce site in the Kröger-Vink notation
$\mathrm{Gd}'_{\mathrm{Ce}}$	dopant Gd sitting at Ce site in the Kröger-Vink notation
$\mu_i(x)$	electrochemical potential of species *i* at *x* in the space charge region
$\mu_i(\infty)$	electrochemical potential of species *i* in the bulk region
μ_i	chemical potential of species *i*
z_i	charge state of species *i*
e	elementary charge
φ	electric potential
°C	degree Celsius
K	degree Kelvin
$c_i(x)$	concentration of species *i* in the space charge region
$c_i(\infty)$	concentration of species *i* in the bulk region
c_d	dopant concentration
$c_d(\infty)$	dopant concentration in the bulk region
c_i^{gb}	concentration of species *i* in the grain boundary impurity enriched region

c_i^{bulk}	concentration of species *i* in the bulk region
z_d	charge state of dopant
k	Boltzmann constant
T	absolute temperature
$\Delta\varphi(x)$	space charge potential at *x*
$\Delta\varphi_0$	space charge potential at *x = 0*
$\Delta\varphi_{gb}$	space charge potential at grain boundary core
$\Delta\varphi_{scl}$	space charge potential in the space charge layer
φ_{bulk}	electric potential in bulk
ε_r	relative dielectric constant
ε_0	vacuum permittivity
ε	dielectric constant, $\varepsilon = \varepsilon_r\varepsilon_0$
ρ	charge density
λ	Debye Length in Gouy-Chapman Model; half-width of space charge zone in Mott-Schottky Model
ρ_{bulk}	charge density in bulk
ρ_{scl}	charge density in space charge layer
$\rho_{segregation}$	charge density of segregated species at grain boundary
$\tilde{\rho}_{gb}$	areal charge density of grain boundary core at Finite Core Model

$\tilde{\rho}_{core}$	areal charge density of grain boundary core at Mott-Schottky Model
$\rho(x)$	grain boundary resistivity at x in the space charge region
ρ_{bulk}	bulk resistivity
ρ_{gb}	grain boundary resistivity
σ_{bulk}	bulk conductivity
σ_{gb}	grain boundary conductivity
σ_i	conductivity of species i
$\overline{\mu}_i$	ionic mobility of species i
R_{gb}	grain boundary resistance
R_{bulk}	bulk resistance
C_{gb}	grain boundary capacitance
C_{bulk}	bulk capacitance
D	electric displacement field
L	macroscopic sample thickness
A	sample cross-sectional area
δ	grain boundary thickness
G	grain size
d	half-width of grain boundary core
d'	half-width of crystallographically visible core thickness,

TΩ	Terra-Ohm, $10^{12}\Omega$
GΩ	Giga-Ohm, $10^{9}\Omega$
pF	Pico-Farad, $10^{-15}F$
fA	Femto-Ampere, $10^{-15}A$
$-z''$	minus imaginary component of the impedance
z'	real component of the impedance
E_{bulk}	activation energy of bulk
E_{gb}	activation energy of grain boundary
$\Delta\theta(x, y)$	phase shift at (x, y)
C_E	interaction constant equal to 0.00728 $rad/(V \cdot nm)$ for 200 keV electrons
$V_p(x, y)$	projected average electric potential
t	sample thickness for electron holography
λ_e	inelastic mean free path of electrons
A_0	amplitude from the sample region in electron hologram
A_r	amplitude from the vacuum region in electron hologram
$\bar{V}(x')$	thickness-averaged electric potential
$\{x_i'\}$	coordinates in the experimental reference frame
$\{x_i\}$	coordinates in the grain boundary reference frame
α	grain boundary tilt angle
$\Delta\varphi_o^{raw}$	tilt corrected space charge potential

$\Delta\theta_{leak}$	phase shift of leakage
σ_{φ}	phase detection limit
C	electron hologram fringe contrast
N_e	number of detected electrons
I_{max}	maximum density in electron hologram
I_{min}	minimum density in electron hologram
V_{MIP}	mean inner potential
$f_j(0)$	electron scattering factor of element j
h	Planck's constant
m_e	rest mass of the electron
n_j	number of atoms of element j that are in the unit cell
Ω	unit cell volume
MHz	Mega-Hertz, $10^6\,Hz$
mHz	Milli-Hertz, $10^{-3}\,Hz$
V_{gb}	electric bias across grain boundary
V_{th}	thermal voltage
I_{gb}	electric current through grain boundary
ppm	particles per million

List of Acronyms

ACIS	alternating current impedance spectroscopy
APT	atom probe tomography
CCD	charge-coupled device
EBSD	electron backscatter diffraction
EDS	energy dispersive spectroscopy
FFT	fast fourier transform
FIB	focused ion beam
FWHM	full width at half maximum
GB	grain boundary
GDC	gadolinia-doped ceria
LEAP	local electrode atom probe
MIECs	mixed ionic-electronic conductors
MIP	mean inner potential
OAEH	off-axis electron holography
PLD	pulsed laser deposition
RE	reference electrode
SAED	selected area electron diffraction
SCN20	$SrCo_{0.8}Nb_{0.2}O_{3-\delta}$
SDC	samarium-doped ceria
SDC02	0.2 at% Sm-doped ceria, $Sm_{0.002}Ce_{0.998}O_{2-\delta}$
SEM	scanning electron microscopy

SIMS	secondary ion mass spectroscopy
SPL	space charge layer
SST 316	stainless steel 316
TEM	transmission electron microscopy
WE	working electrode
YSZ	yttria-stabilized zirconia

Table of Contents

List of Figures

List of Tables

1 Introduction

1.1 Motivation

In many ionic conductors charge transport across and along internal interfaces dominates the overall properties. Such boundaries may serve as high conductivity pathways or, as is often observed, as high impedance barriers.[1] Because the activation energy for transport across grain boundaries is often large, the impact of such boundaries are pronounced at ambient temperatures, a factor frustrating efforts to develop all solid state batteries and intermediate temperature solid oxide fuel cells. Several causes for high ionic impedance at grain boundaries have been discussed. For the particular case of oxygen ion conductors, these include (i) the presence of blocking impurity phases, in particular siliceous material that wets the entire grain boundary,[2] (ii) constriction effects,[3] (iii) dopant segregation,[4,5] and (iv) excess positive charge at the grain boundary core, balanced by a negative space charge region in the near vicinity of the grain boundary, in which positively charged ionic carriers, i.e. oxygen vacancies, are depleted.[6–8] Although these phenomena do not necessarily occur in isolation (for example, dopant segregation may lead to interfacial charge imbalance,[5] or impurity phases may constrict grain-to-grain contact),[9] space charge effects have come to be accepted as the primary cause of high grain boundary impedance in high-purity electrolytes.[10–12]

However, the vast majority of studies aimed at uncovering the origin of grain boundary behavior have relied on macroscopic measurements that yield ensemble-averaged properties. Thus, the questions of how the properties of individual grain boundaries contribute to the global average, and indeed how wide a range of properties occur within a single polycrystalline sample remain unanswered. Recognition of this gap in understanding has driven efforts to study the

electrochemistry of individual grain boundaries,[13,14] with recent efforts directed at measuring even anion concentrations,[15] from which charge imbalance has been inferred. Nevertheless, *direct* evidence of electrical perturbations at the grain boundaries of ionic conductors, much less the variability of such perturbations within the macroscopic average, has rarely been presented. In this work, we study electrical properties, chemical composition and misorientation of single grain boundaries to address this need, focusing in particular on ceria, a material of widespread interest to the materials community.[16,17]

1.2 Oxide Electrolytes

Oxide electrolytes are mixed conductors with predominate ionic conductivity and minor electronic conductivity. The study on mixed conductors can date back to the year of 1834 when Michael Faraday discovered high electrical conductivity of PbF_2 at high temperatures.[18] The initial studies on oxygen ion conducting materials were from Nernst in 1899 who observed high ionic conductivity in doped zirconia due to the fast transport of oxide ions.[19] Nowadays, many mixed conductors have been studied under a wide range of temperatures and atmospheres for various applications.

Cerium oxide (ceria), as a leading mixed conductor, has been investigated extensively for application in a range of energy technologies due to: (1) its easy nonstoichiometric change allowing for oxygen deficiency even without acceptor doping, $O_O^{\times} \rightleftharpoons \frac{1}{2}O_2 + V_O^{\bullet\bullet} + 2e'$, and (2) a large oxygen vacancy concentration resulting from heavily acceptor doping, e.g. $Sm_2O_3 \xrightarrow{CeO_2} 2Sm'_{Ce} + 3O_O^{\times} + V_O^{\bullet\bullet}$. The defect reactions are described by the Kröger-Vink notation.

The energy technologies related to ceria include oxygen storage materials for solar thermochemical dissociation of water and carbon dioxide to fuels[20–22], and more importantly, as in fuel cells where they can serve as electrolyte and composite of electrode material due to fast oxygen-ion conduction[16,17].

Before ceria-based electrolyte gained interest as an electrolyte for the solid oxide fuel cell, yttria-stabilized zirconia (YSZ) had long been recognized as the most reliable candidate due to its high phase stability and satisfying conductivity at high operating temperature 900 °C. But when the fuel cell system reaches this high of a temperature, it becomes unstable. Some sources of the

instability include the solid electrolyte/electrode and the electrode/interconnector interfaces. Continuously working under high temperature environment would speed up the degradation process, giving poor stability of the fuel cell. Besides, in order to keep elevated operating temperature, additional thermal energy has to be supplied to the fuel cell system increasing the energy costs. Therefore, many studies have been performed to seek for alternative materials as an electrolyte for reduced temperature solid oxide fuel cells.

Doped ceria has long been studied for the electrical conductivity since the 1970s. In 1975, Tuller and Nowick determined the electrolytic domain of divalent and trivalent doped ceria[23]. The result indicated that doped ceria may become an attractive candidate for the fuel cells at temperatures below those at which doped zirconia is used due to higher conductivity, lower activation energy and absence of polarization effects to lower temperatures. Recently, ceria based electrolyte has been selected for study because of increasingly interest in this material as an electrolyte for reduced temperature solid oxide fuel cells, which can decrease the traditional operating temperature from 800-1000 °C to 500-800 °C. Ceria-based electrolyte such as samarium-doped ceria (SDC) and gadolinia-doped ceria (GDC) exhibit higher conductivity than YSZ at intermediate temperature. Specifically, electrical conductivity of GDC is about one order of magnitude larger than that of YSZ with about 0.1S/cm at 800°C[24]. Fuel cell operation at this reduced temperature regime has the potential for substantially lowering the auxiliary component costs and increasing the thermochemical stability of the system.

1.3 Grain Boundary Transport Theory in Oxide Electrolytes

Resistive grain boundary in undoped and acceptor doped ceria has been observed dating back to 1980.[25] The same grain boundary effect was also observed earlier in stabilized zirconia [26–28], which was associated with the blocking impurity phases, in particular siliceous materials. The impurities in the vicinity of grain boundaries heavily reduced ionic conduction. It was found in acceptor doped ceria when nearly silicon-free starting materials were used, the grain boundary resistivity was greatly reduced.[29] However, when further study was performed on electrical conductivity in nanocrystalline ceria, the observed electronic conductivity was significantly enhanced despite the grain boundary number density increased.[30–32] It was realized that blocking impurity phases was not able to explain all the experimental results. Then space charge effects have gradually come to be accepted as the primary cause of high grain boundary impedance.[11]

In the space charge theory, a charged grain boundary core is balanced by a space charge region with the opposite charge in the near vicinity of the grain boundary, in which the carriers that has the same charge as with the core are depleted. In acceptor doped ceria, the grain boundary core has excess positive charge which repels positive oxygen vacancies in the space charge region. The region with depleted oxygen vacancies gives low ionic conductivity through grain boundaries. In contrast, the positive grain boundary core will cause negative electronic defects enriched in the space charge region, which explains well the greatly enhanced electronic conductivity in nanocrystalline ceria when the grain size is comparable or even smaller than space charge region.

In the space charge region, the concentration profile is governed by the constancy of the electrochemical potential, which is $\mu_i(x) = \mu_i(\infty)$ with x in the space charge region and ∞

representing the bulk, where $\mu_i = \mu_i + z_i e\varphi$ with μ_i as chemical potential of species *i*, z_i as charge state, *e* as the elementary charge and φ as electric potential. With the dilute limit/ideal solution and one-dimensional model, the concentration profile of species *i* dependence of *x* can be determined by:

$$\frac{c_i(x)}{c_i(\infty)} = \exp\left(-\frac{z_i e}{kT}\Delta\varphi(x)\right) \tag{1.1}$$

where $c_i(x)$ is concentration of species *i* in the space charge region, $c_i(\infty)$ is the concentration in the bulk region (far away from grain boundary core), *k* is Boltzmann's constant, *T* is temperature, and $\Delta\varphi(x)$ is the electric potential relative to the bulk. Based on Poisson's equation $\nabla^2\varphi = -\frac{\rho}{\varepsilon_r\varepsilon_0}$, the electric space charge potential can be determined to be:

$$\frac{\partial^2}{\partial x^2}\Delta\varphi(x) = -\frac{\sum_i z_i e c_i(\infty)}{\varepsilon_r\varepsilon_0}\exp\left(-\frac{z_i e}{kT}\Delta\varphi(x)\right) \tag{1.2}$$

where ε_r is relative dielectric constant, ε_0 is vacuum permittivity, ρ is the total charge concentration.

To get the analytical solution of Poisson's equation, the knowledge of species concentration and boundary conditions are required. Two primary models, Gouy-Chapman Model and Mott-Schottky Model are used to describe profiles of space charge potential and carrier concentration distribution. The two models have slightly different assumptions to obtain analytical solutions of the Eq. (1.2).

1.3.1 Gouy-Chapman Model

The Gouy-Chapman Model was first proposed for study on the thermal motion of ions near a charged surface.[33,34] In this model, there is a diffuse double layer consisting of charges in a dielectric continuum in response to the electric field built by charged surface, which is described by Poisson's differential equation. This model is used to explain the space charge effect in polycrystalline solid state materials.[6,11,12,35,36]

In the Gouy-Chapman Model as shown in Figure 1.1, concentration profiles of all charged carriers follow from Eq. (1.1). Even though doped cations are difficult to move at intermediate temperature, the concentration profiles are formed at high sintering temperature and stay unchanged at lower temperature (assuming space charge potential constant).

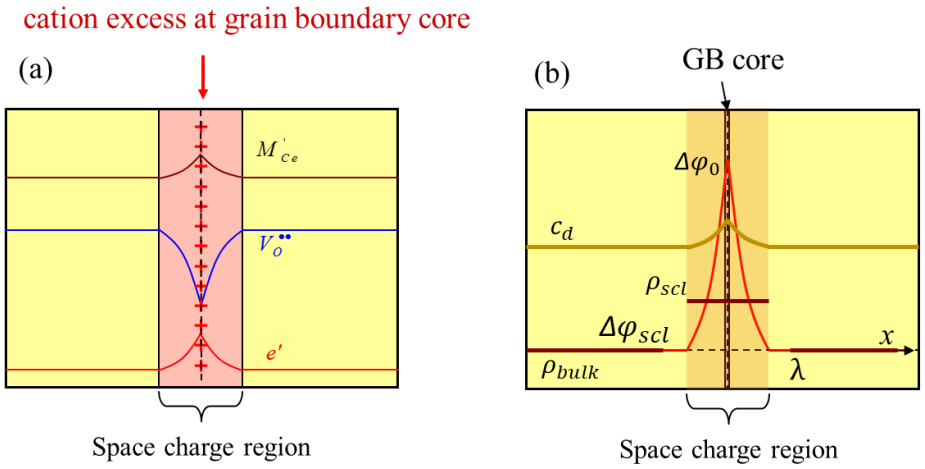

Figure 1.1 Schematic of Gouy-Chapman Model : (a) carrier concentration in space charge region and bulk, and (b) charge density and potential profile.

The Poisson's equation can be solved only analytically for the situation of two charge carriers with $z_+ = -z_- = z$ (e.g., Ca doped CeO_2, Ca''_{Ce} is an immobile charged carrier with effective charge state $z_{Ca'_{Ce}} = -2$, oxygen vacancy is a mobile charged carrier with $z_{V_o^{\cdot\cdot}} = +2$, $z_{V_o^{\cdot\cdot}} = -z_{Ca'_{Ce}} = +2$).[6,12] The bulk concentrations are equal due to electroneutrality $c_+(\infty) = c_-(\infty) = c_\infty$. The screening length is approximately Debye length:

$$\lambda = \sqrt{\frac{\varepsilon_r \varepsilon_0 kT}{2z^2 e^2 c_\infty}} \tag{1.3}$$

The Gouy-Chapman profile with semi-infinite boundary conditions is determined to be:

$$\Delta\varphi(x) = -\frac{2kT}{z_\pm e}\ln\left(\frac{1+\vartheta_\pm \exp(-x/\lambda)}{1-\vartheta_\pm \exp(-x/\lambda)}\right) \tag{1.4}$$

with $\vartheta_\pm = \frac{\zeta_\pm^{1/2}-1}{\zeta_\pm^{1/2}+1} = -\vartheta_\mp$ and $\zeta_\pm = \frac{c_\pm(x)}{c_\pm(\infty)} = \exp\left(-\frac{z_\pm e\Delta\varphi(x)}{kT}\right)$. The carrier concentration profiles are determined by inserting Eq. (1.4) to Eq. (1.1) giving:

$$\frac{c_\pm(x)}{c_\pm(\infty)} = \left(\frac{1+\vartheta_\pm \exp(-x/\lambda)}{1-\vartheta_\pm \exp(-x/\lambda)}\right)^2 \tag{1.5}$$

However, this analytical solution doesn't apply for the case of trivalent dopant in ceria (e.g., Sm doped CeO_2, Sm'_{Ce} is an immobile charged carrier with effective charge state $z_{Sm'_{Ce}} = -1$, and oxygen vacancy $V_O^{\cdot\cdot}$ is a mobile charged carrier with $z_{V_o^{\cdot\cdot}} = +2$, $z_{V_o^{\cdot\cdot}} \neq -z_{Sm'_{Ce}}$). But by appropriate approximation that only dopant concentration c_d is taken into consideration and all other carriers

are omitted (such as ignoring oxygen vacancies due to the depletion in the space charge region if the space charge potential is positive), a simpler analytical solution can be determined.

Poisson's equation is now:

$$\frac{\partial^2}{\partial x^2}\Delta\varphi(x) = -\frac{z_d e c_d(\infty)}{\varepsilon_r \varepsilon_0}\exp\left(-\frac{z_d e}{kT}\Delta\varphi(x)\right) \tag{1.6}$$

where z_d is the charge state of the dopant, $c_d(\infty)$ is the dopant concentration in the bulk. Applying the boundary conditions:

$$\begin{aligned}\Delta\varphi(0) &= \Delta\varphi_0 \\ \Delta\varphi(2\lambda) &= 0\end{aligned} \tag{1.7}$$

One analytical solution is:

$$\Delta\varphi(x) = \Delta\varphi_0 + \frac{2kT}{z_d e}\ln\left(1+\frac{x}{2\lambda}\exp(-\frac{z_d e\Delta\varphi_0}{2kT})\right), 0 < x < 2\lambda \tag{1.8}$$

$$\text{with } \lambda = \sqrt{\frac{\varepsilon_r \varepsilon_0 kT}{2z^2 e^2 c_d(\infty)}}$$

and the dopant concentration profile is:

$$\frac{c_d(x)}{c_d(\infty)} = \exp(-\frac{z_d e\Delta\varphi_0}{kT})\left(1+\frac{x}{2\lambda}\exp(-\frac{z_d e\Delta\varphi_0}{2kT})\right)^{-2} \tag{1.9}$$

All other carriers that are omitted in Poisson's equation now can be estimated with the known electric potential:

$$\frac{c_i(x)}{c_i(\infty)} = \exp(-\frac{z_i e\Delta\varphi(x)}{kT}) = \exp(-\frac{z_i e\Delta\varphi_0}{kT})\left(1+\frac{x}{2\lambda}\exp(-\frac{z_i e\Delta\varphi_0}{2kT})\right)^{-2} \qquad (1.10)$$

For example, the oxygen vacancy concentration is:

$$\frac{c_{V_o^{\bullet\bullet}}(x)}{c_{V_o^{\bullet\bullet}}(\infty)} = \exp(-\frac{2e\Delta\varphi_0}{kT})\left(1+\frac{x}{2\lambda}\exp(-\frac{e\Delta\varphi_0}{kT})\right)^{-2} \qquad (1.11)$$

1.3.2 Mott-Schottky Model

In the Mott-Schottky Model, the dopant concentration is assumed to be constant across grain boundaries which does not follow Eq. (1.1). All other carriers are omitted.

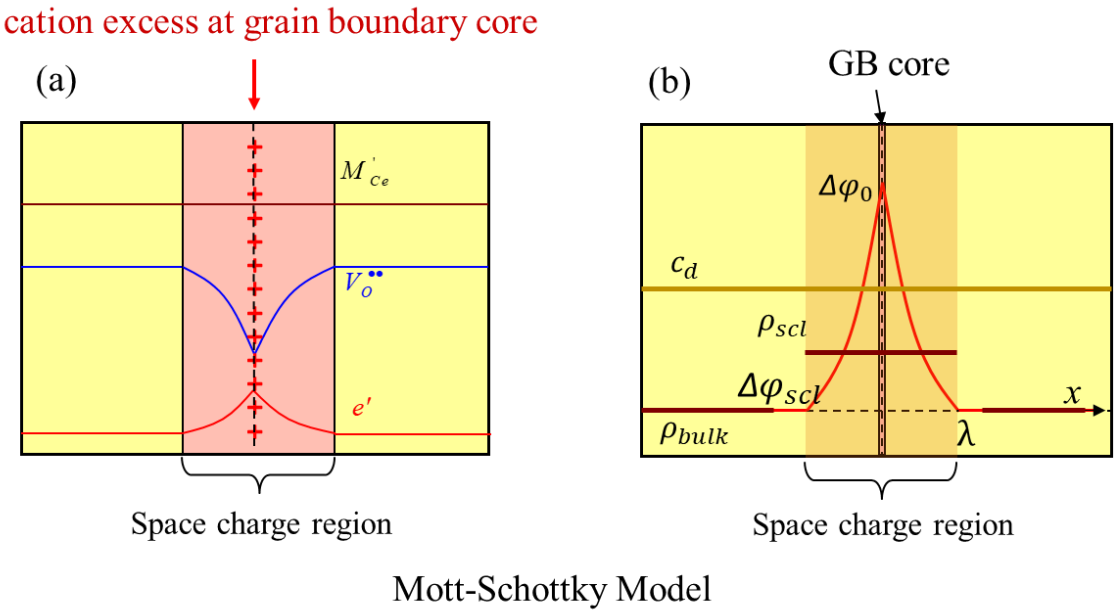

Figure 1.2 Schematic of Mott-Schottky Model : (a) carrier concentration in space charge region and bulk, and (b) charge density and potential profile.

Then Poisson's equation turns into:

$$\frac{\partial^2}{\partial x^2}\Delta\varphi(x) = -\frac{z_d e c_d}{\varepsilon_r \varepsilon_0} \tag{1.12}$$

where z_d is the charge state of the dopant, c_d is the dopant concentration in the bulk. Applying the boundary conditions:

$$\Delta\varphi(0) = \Delta\varphi_0, \quad \Delta\varphi(\lambda) = 0, \quad \left.\frac{\partial\Delta\varphi}{\partial x}\right|_{x=\lambda} = 0 \tag{1.13}$$

The analytical solution is determined to be:

$$\Delta\varphi(x) = \Delta\varphi_0\left(1-\frac{|x|}{\lambda}\right)^2, \quad x < \lambda \tag{1.14}$$

$$\lambda = \sqrt{-\frac{2\varepsilon_r \varepsilon_0 \Delta\varphi_0}{z_d e c_d}} \tag{1.15}$$

and the resulting carrier concentration profiles follow:

$$\frac{c_i(x)}{c_i(\infty)} = \exp\left(-\frac{z_i e\Delta\varphi(x)}{kT}\right) = \exp\left(-\frac{z_i e\Delta\varphi_0}{kT}\left(1-\frac{|x|}{\lambda}\right)^2\right) \tag{1.16}$$

which shows a direct relationship between space charge potential and ionic concentration which is also related to ionic conductivity due to $\sigma_i = z_i e c_i \bar{\mu}_i$ where σ_i is ionic conductivity and $\bar{\mu}_i$ is ionic mobility. In oxygen vacancy dominated ionic conductors, such as Sm-doped ceria in mild oxidizing environment at intermediate temperatures, the main carrier is oxygen vacancy. The oxygen vacancy profile due to space charge potential is:

$$\frac{c_{V_o^{\cdot\cdot}}(x)}{c_{V_o^{\cdot\cdot}}(\infty)} = \exp(-\frac{2e\Delta\varphi(x)}{kT}) \tag{1.17}$$

If the mobility of oxygen vacancy is assumed to be equal for space charge region and the bulk, then we have:

$$\frac{\rho(x)}{\rho_{bulk}} = \frac{c_{V_o^{\cdot\cdot}}(\infty)}{c_{V_o^{\cdot\cdot}}(x)} = \exp(\frac{2e\Delta\varphi(x)}{kT}) \tag{1.18}$$

where $\rho(x)$ is grain boundary resistivity at *x* and ρ_{bulk} is bulk resistivity. The grain boundary resistivity can be determined by:

$$\frac{\rho_{gb}}{\rho_{bulk}} = \frac{1}{\lambda}\int_0^{\lambda} \exp(\frac{2e\Delta\varphi(x)}{kT})dx \tag{1.19}$$

The integrating factor needs to change from dx to $d\Delta\varphi(x)$ following by Eq. (1.14):

$$dx = -\sqrt{\frac{\varepsilon_r\varepsilon_0}{2ec_d\Delta\varphi_0}}d\Delta\varphi(x) \tag{1.20}$$

The Eq. (1.19) turns into:

$$\begin{aligned}\frac{\rho_{gb}}{\rho_{bulk}} &= \frac{1}{\lambda}\int_0^{\Delta\varphi_0} \exp(\frac{2e\Delta\varphi(x)}{kT})\sqrt{\frac{\varepsilon_r\varepsilon_0}{2ec_d\Delta\varphi_0}}d\Delta\varphi(x) \\ &\approx \frac{\exp\left(2e\Delta\varphi_0 / kT\right)}{4e\Delta\varphi_0 / kT}\end{aligned} \tag{1.21}$$

For general carrier with charge state *z*, the equation becomes:

$$\frac{\rho_{gb}}{\rho_{bulk}} \approx \frac{\exp\left(ze\Delta\varphi_0 / kT\right)}{2ze\Delta\varphi_0 / kT} \tag{1.22}$$

Therefore, as long as the grain boundary and bulk resistivity are known, the space charge potential can be determined.

1.3.3 Finite Core Model

In either Gouy-Chapman Model or Mott-Schottky Model, the grain boundary core is a mathematically infinite thin area which introduces a singularity at $x = 0$, which is not physically true. High resolution transmission electron images and atom probe tomography show that grain boundary core has finite thickness (see Chapter 3). In order to explore the space charge effect, a more realistic model needs to be employed.

Here, we proposed a space charge model for a grain boundary with a core of finite width, $2d$, and position-independent charge density, ρ_{gb}, which was developed to aid in unveiling space charge origins. The coordinate system is such that $x = 0$ at the grain boundary core, $\Delta\varphi(x) = \varphi(x) - \varphi_{bulk}$ (where φ_{bulk} is the electric potential in bulk), $\Delta\varphi_0 = \Delta\varphi(x = 0)$, and all quantities are symmetric about x.

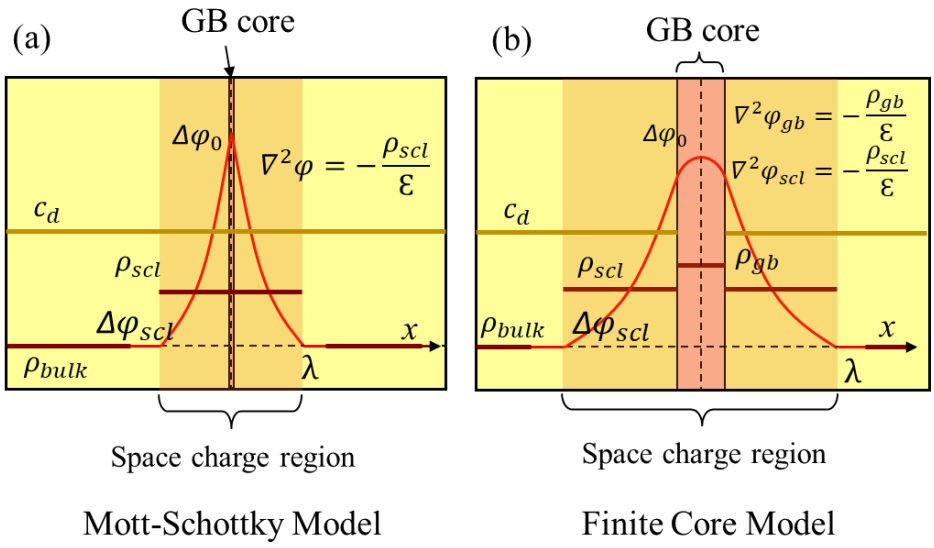

Figure 1.3 Compare Mott-Schottky Model and Finite Core Model in charge density and potential profiles : (a) Mott-Schottky Model, and (b) Finite Core Model.

For reference, it is noted that in the Mott-Schottky solution, in which mobile defects (taken here to be oxygen vacancies) are depleted in the space charge zone as a result of a charge at the grain boundary core, the following apply:

$$\rho_{scl} = ez_d c_d, \; |x| < \lambda \tag{1.23}$$

$$\rho_{bulk} = \sum ez_i c_i = 0, \; x \to \infty \tag{1.24}$$

and the solution to the potential profile is Eq. (1.14) where λ is given in Eq. (1.15). The area-specific charge density at the core, responsible for generating the space charge potential, is:

$$\tilde{\rho}_{core} = \sqrt{8e\varepsilon c_d \Delta\varphi_0} \tag{1.25}$$

Thus, the bulk dopant concentration (c_d, assumed to be the same in the bulk and space charge regions), the dielectric constant ($\varepsilon=\varepsilon_r\varepsilon_0$, also assumed to be the same in the bulk and space charge regions), and $\Delta\varphi_0$ fully define the electric field profile. From the latter and an assumption of electrochemical equilibrium, the oxygen vacancy concentration can be computed. (The Mott-Schottky solution is self-inconsistent in the transition region between the space charge layer and the bulk and hence the charge density in this region is not shown.)

For the finite core model developed here, three regions of charge density are defined:

$$\rho_{gb} = const = f(\Delta\varphi_0),\ |x| < d \tag{1.26}$$

$$\rho_{scl} = ez_d c_d^{bulk},\ d < |x| < \lambda \tag{1.27}$$

$$\rho_{bulk} = \sum ez_i c_i = 0,\ x \to \infty \tag{1.28}$$

Applying Poisson's equation to the GB core and the neighboring space charge layer gives:

$$\begin{aligned} \nabla^2(\Delta\varphi_{gb}) &= -\frac{\rho_{gb}}{\varepsilon},\ |x| < d \\ \nabla^2(\Delta\varphi_{scl}) &= -\frac{\rho_{scl}}{\varepsilon},\ d < |x| < \lambda \end{aligned} \tag{1.29}$$

where $\Delta\varphi_{gb}$ and $\Delta\varphi_{scl}$ are the electric potentials in the GB core and space charge layer, respectively. The boundary conditions are obtained recognizing that at $x = d$ both the electric potential field and the normal direction of electric displacement field (D). Taking the dielectric constant to be fixed, these requirements imply:

$$\Delta\varphi_{gb}(d) = \Delta\varphi_{scl}(d)$$
$$\left.\frac{\partial\Delta\varphi_{gb}}{\partial x}\right|_{x=d} = \left.\frac{\partial\Delta\varphi_{scl}}{\partial x}\right|_{x=d} \tag{1.30}$$

The symmetric properties of the potential profile and the definition of space charge potential $\Delta\varphi_0$ and space charge thickness λ give additional conditions, specifically:

$$\Delta\varphi_{gb}(0) = \Delta\varphi_0 \qquad \Delta\varphi_{scl}(\lambda) = 0$$
$$\left.\frac{\partial\Delta\varphi_{gb}(x)}{\partial x}\right|_{x=0} = 0 \qquad \left.\frac{\partial\Delta\varphi_{scl}(x)}{\partial x}\right|_{x=\lambda} = 0 \tag{1.31}$$

The solutions satisfying these boundary conditions are:

$$\Delta\varphi_{gb}(x) = -\frac{\rho_{gb}}{2\varepsilon}x^2 + \Delta\varphi_0, \ |x| < d$$
$$\Delta\varphi_{scl}(x) = -\frac{\rho_{scl}}{2\varepsilon}(|x| - \lambda)^2, \ d < |x| < \lambda \tag{1.32}$$

where the space charge potential $\Delta\varphi_0$ and the space charge thickness λ are respectively given as:

$$\lambda = (1 - \frac{\rho_{gb}}{\rho_{scl}})d$$
$$\Delta\varphi_0 = \frac{(\rho_{gb} - \rho_{scl})\rho_{gb}d^2}{-2\rho_{scl}\varepsilon} \tag{1.33}$$

The terms d and ρ_{scl} were taken as fixed input values, leaving only one free variable ($\Delta\varphi_0$ or λ) in the fitting of $\Delta\varphi(x)$ to the data. Again, the charge density approximation is not self-consistent at the boundaries between regions.

In the limit of an infinitesimally thin GB core ($d \to 0$), the expressions above for λ and $\Delta\varphi_0$ simplify to the Mott-Schottky result. This can be shown as defining the areal charge density of the GB core according to $\tilde{\rho}_{gb} \equiv \rho_{gb} d$, then evaluating the limiting values of λ and $\Delta\varphi_0$ in terms of this quantity:

$$\begin{aligned} \lim_{d\to 0}\left[\lambda\right] &= \lim_{d\to 0}\left[\left(1-\frac{\tilde{\rho}_{gb}}{d\,\rho_{scl}}\right)d\right] \;=\; -\frac{\tilde{\rho}_{gb}}{\rho_{scl}} \\ \lim_{d\to 0}\left[\Delta\varphi_0\right] &= \lim_{d\to 0}\left[=\frac{\left(\frac{\tilde{\rho}_{gb}}{d}-\rho_{scl}\right)\tilde{\rho}_{gb}d}{-2\rho_{scl}\varepsilon}\right] = \; -\frac{\tilde{\rho}_{gb}^{2}}{2\rho_{scl}\varepsilon} \end{aligned} \tag{1.34}$$

Inserting the limiting value of λ into the limiting value of $\Delta\varphi_0$, yields the familiar expression:

$$\lambda = \sqrt{\frac{2\varepsilon\Delta\varphi_0}{-\rho_{scl}}} \tag{1.35}$$

2 Experimental Methods

2.1 Lightly Doped High Purity CeO_2 Compact

2.1.1 Sample Synthesis & Characterization

Powders of 0.2% samarium (Sm) doped ceria (SDC02) were synthesized via solid state reaction from high purity cerium oxide (CeO_2, 99.995% Aldrich Chemistry, Inc) and samarium oxide (Sm_2O_3,99.999% Aldrich Chemistry, Inc). Dense compacts were prepared by conventional ceramics processing: the powder was first pressed under a uniaxial pressure of 100 MPa for 30 s, then compacted isostatically under a pressure of 250 MPa for 20 min, and finally sintered at 1500 °C for 10 hours under still air. The relative density of the resulting compacts, measured by the Archimedes method, exceeded 96% of the theoretical value. The surface microstructure of the as-sintered material was evaluated by scanning electron microscopy (SEM) (FEI Quanta 650 ESEM), and the grain size determined by the mean-intercept method[37].

Electrical conductivity was measured by impedance spectroscopy in a pseudo four-probe configuration. The ceria sample, 1.27 cm in diameter, was polished down to a thickness of 700 μm, from 1.2 mm to render conductance high enough to measure. This had the benefit of removing impurity contaminated surface regions. Au paste electrodes were applied to either side of the disc, and the structure was heat-treated at 600 °C for 1 hour to cure the contacts. Impedance spectra were collected under flowing synthetic air, supplied at a space velocity of 10 cm/min. The sample temperature was varied between 350 °C and 250 °C in 50 °C decrements. The combination of light doping and moderate temperatures resulted in extremely high impedance and necessitated the use of a Faraday cage to block electrical noise from the environment. In this configuration, impedance as high as several TΩ and capacitance as low as 0.01 pF could be measured. Impedance spectra

were recorded on cooling, after a dwell time of 4-8 hours at each temperature to reach equilibrium. Data were collected using a Modulab XM frequency response analyzer equipped with a Femto Ammeter card, at frequencies from 1 MHz to 0.001 Hz and at a zero-bias perturbation amplitude of 50 mV.

For the transmission electron microscopy (TEM) studies, a sintered pellet was mechanically cut and then polished down with a final stage using 1 μm polishing powder. Following polishing, the sample was dimpled to achieve a sample thickness of ~20 μm in the central region. Finally, Ar ion milling (the last step: 300 V for 1 hour at -120 °C) was used to polish the central region of the sample to minimize any possible damage during preparation. Samples were extracted from the interior portion of the sintered compact, with the expectation that these would be free of contaminants possibly incorporated during high temperature processing. The grain boundary crystallographic features were investigated by TEM (JEOL JEM-2100 FasTEM). The chemical composition was studied by energy dispersive spectroscopy (EDS) (SuperX EDS, FEI Talos F200X TEM/STEM) with an acceleration voltage of 200 keV.

2.1.2 Electron Holography

Off-axis electron holography was performed using a Tecnai F20 S/TEM operated at 200 keV at the Center for Nanoscale Materials, Argonne National Laboratory, using the samples previously prepared for TEM. A schematic of off-axis electron holography is shown in Figure 2.1 in which the Möllenstedt electron biprism is inserted between the back focal plane and the image plane by means of a modified selected-area aperture holder.[38] The electron hologram arising from the overlapping object wave and reference wave is in the image plane.

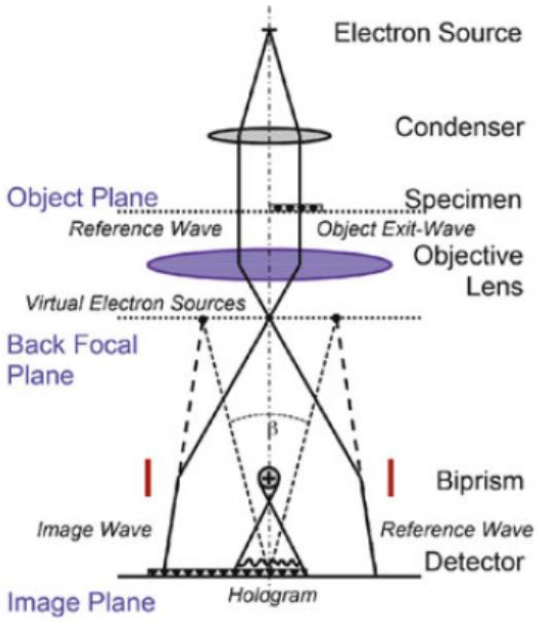

Figure 2.1 Schematic of the electron optical setup for off-axis electron holography.

During electron holography, the sample was maintained at an elevated temperature of 300 °C (consistent with impedance measurements under the same conditions) using a Gatan heating holder. Holograms with a field of view of 48 nm were acquired with a 5s exposure time at positive bias of 100 V applied to the biprism. This resulted in good fringe contrast, > 20% over the sample area and > 30% over vacuum, along with a typical fringe spacing of ~ 0.2 nm (= 6 pixels) (see Chapter 3.3.4). The latter implies a spatial resolution of ~ 0.6 nm. The detection limit for the phase shift in vacuum was determined to be ~ $2\pi/63$ rad, which implies a voltage detection limit of ~ 0.2 V (see Figure 3.12). The off-axis electron holograms were analyzed to reconstruct the phase shift and amplitude of the electrons using a standard Fast Fourier Transform algorithm in

the HoloWorks software in Gatan Digital Micrograph (Version 2.31.734.0). Selected area diffraction patterns were recorded in conventional TEM mode to determine the relative misorientation across grain boundaries. Grain boundaries with [110] zone axis aligned were sought out and examined for the study of $\Delta\varphi_o$ on tilt angle. Analyses were typically performed at regions of the sample ranging from 40 to 150 nm in thickness.

2.1.3 Atom Probe Tomography

For atom probe tomography (APT), a sintered compact was fractured to provide access to the interior. Sections of the material, ~700 μm from the sample surface, were cut and polished into sharp tips with a final tip radius < 50 nm using a focused ion beam (FIB) (FEI Helios Nanolab SEM / FIB). Tips were loaded into the APT buffer chamber immediately after preparation, and the temperature of the tips was held at 25K throughout the entire measurement. A local electrode atom probe (LEAP) (LEAP5000 XS, CAMECA) was used to perform APT characterization as shown by the schematic in Figure 2.2[39]. Bias up to 7 kV was applied to the tips with laser assistance using an energy of 20 pJ and frequency of 250 kHz. Using these conditions, the background level was kept at 10 ppm/ns. Over 20 million ions were collected for each tip examined. The 3-D atom map reconstruction and GB composition analysis were performed using the software package IVAS 3.8.2. Details of the conversion from 3-D maps to the 1-D projections are shown in Figure 3.16.

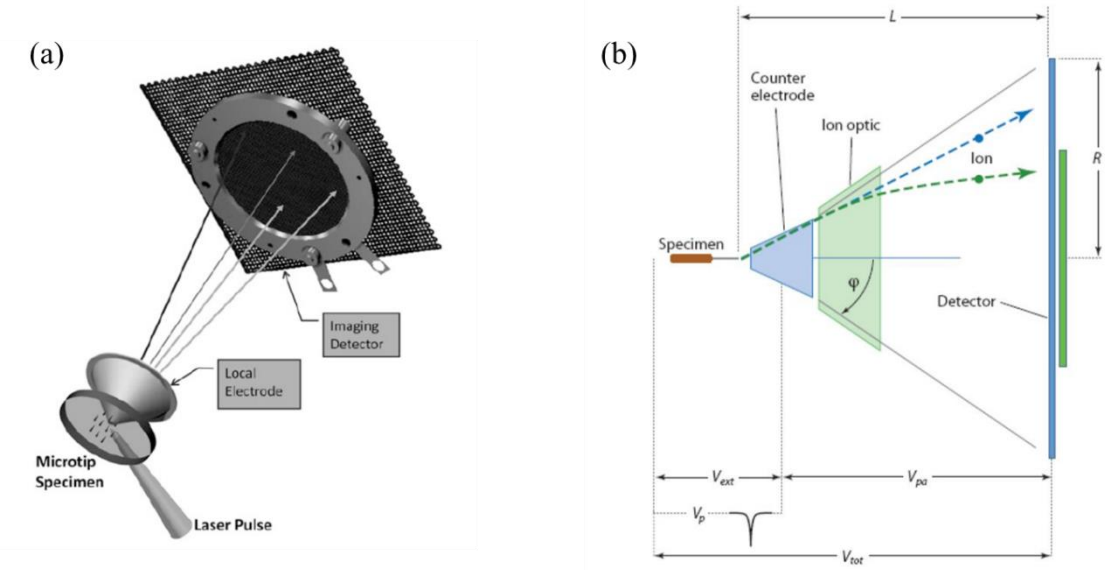

Figure 2.2 Schematic of the Local Electrode Atom Probe : (a) microtip specimen, local electrode, and detector geometry (b) geometry of an atom probe including V_{tot} = the total accelerating voltage of the system, V_{ext} = extraction voltage used with both static and dynamic fields, V_{pa} = post acceleration voltage that can range in value from zero to magnitudes comparable to V_{ext}, V_p = voltage pulse that is the time-varying component of dynamic fields, L = the flight path length to the center of the detector, R = the radius of the detector.

2.2 Undoped CeO_2 Fibers

2.2.1 Sample Preparation

The undoped CeO_2 fibers (purity > 99%, Zircar Zirconia, Inc), hereafter simply referred to as fibers, have diameters in the 3 – 10 μm range with a typical diameter of 6 μm selected for fiber study. The grain boundaries of the fibers lie normal to the axial direction and are spaced roughly at 10-40 μm internals along the length of the fiber, which is generally tens to over one hundred μm. Transport measurements of single fibers were made using eight fibers, six with normal grain boundaries and two without.

In addition to the fibers, a comparative bulk sample was prepared by sintering a CeO_2 fiberboard, hereafter simply referred to as fiberboard. The dense fiberboard was made of fibers from the same batch via a conventional sintering process: the fibers were ground and pressed under a uniaxial pressure of 100 MPa for 30 s, compacted isostatically under a pressure of 250 MPa for 20 min, and finally sintered at 1550 °C for 28 hours under still air with a heating rate of 3 °C/min. The relative density of the resulting compact, measured by the Archimedes method, exceeded 96% of the theoretical value (7.215 g/cm^3). Electrical conductivity of the fiberboard sample was characterized by electrochemical impedance spectroscopy with controlled temperatures and atmospheres. The sample was placed inside a continuous flow furnace to which gases were delivered via digital mass flow controllers, and a pseudo four-probe configuration was employed (3 Terminal configuration was employed to measure the impedance of fibers, see Chapter 2.2.4). Au paste electrodes were applied to both sides of the disc, and the structure was heat-treated at 600 °C for 1 hour to cure the contacts. Impedance spectra were collected with an AC amplitude of 50

mV under the flow of synthetic air, supplied at a space velocity of 10 cm/min. The sample temperature was varied from 700 °C to 300 °C in 50 °C decrements.

2.2.2 Structural and Chemical Analysis

Misorientation across grain boundaries in solid state polycrystalline materials can be precisely determined by electron backscatter diffraction (EBSD). Upon interacting with the sample, elastically backscattered electrons can undergo coherent Bragg scattering as they exit the sample. This generates a diffraction pattern formed of Kikuchi bands that is collected at a detector. The sample is held at a high tilt angle, Figure 2.3[40,41], to enhance the contrast in the diffraction pattern. Misorientation in terms of Euler angles can be calculated based on the electron backscatter patterns (EBSP) of two adjacent grains. Compared to selected area electron diffraction (SAED) in TEM, EBSD is non-destructive and can provide fast misorientation analysis without introducing damage. To study grain boundary misorientation in fibers, the Oxford Aztec EBSD system installed in FEI Quanta 650 ESEM was used to measure backscatter patterns at either side of grain boundaries. Samples were coated with ~5nm carbon film, which proved sufficient to reduce surface charging (CeO_2 and the MgO are poor electronic conductors) without interfering with the backscatter signal. Samples were mounted on a 70° sample holder relative horizontal plane specifically for analysis, which was operated at 30 kV with spot size 5 and aperture 3. The mapping step size was set to 0.02 μm. Results indicated that the mean angle deviation was less than 1° during the entire measurement.

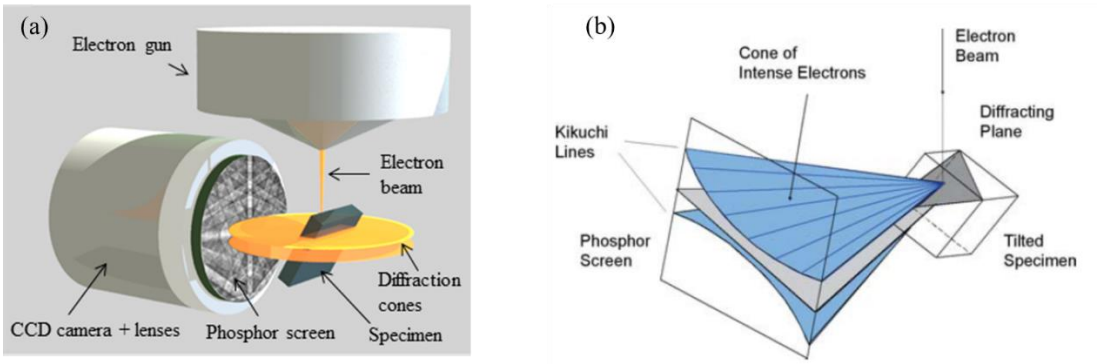

Figure 2.3 Schematic of Electron Backscatter Diffraction : (a) illustration of the detection geometry and a conventional detector. (b) schematic of the diffracting cones with respect to the reflecting plane, the specimen, and the phosphor screen.

Grain boundary composition was characterized by secondary ion mass spectroscopy (SIMS) due to its high sensitivity (~1 ppm), and more importantly, simplified sample preparation as compared to APT. SIMS is the mass spectrometry of ionized atoms or clusters that are emitted from the very top of the sample surface upon being bombarded with energetic primary particles as shown in the schematic, Figure 2.4[42]. The typical pulsed primary ion is Ga^+ with an energy range of 1-25 kV. The chemical composition, especially impurity level, in fibers was studied using 25 kV Ga source (PHI TRIFT III ToF-SIMS). Prior to measurement, the sample surface was cleaned by a Ga^+ source for 10 mins which approximately etched 1-2 μm of the sample surface to remove contaminants.

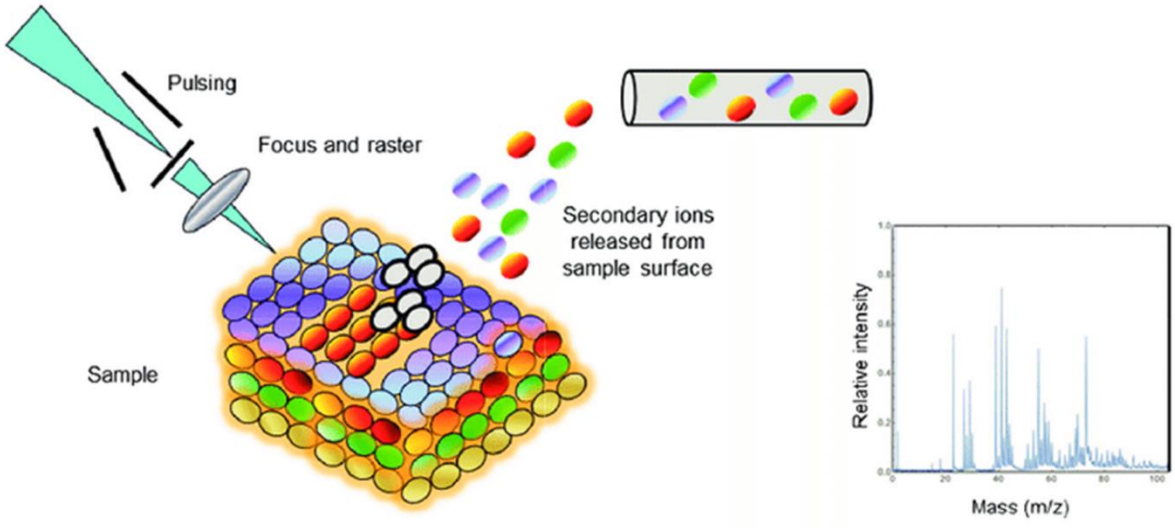

Figure 2.4 Schematic overview of the basic principle of time-of-flight secondary ion mass spectrometry with high-energy primary ions.

2.2.3 Device Fabrication

A novel device for in-plane high impedance measurement was developed for fibers. MgO (100) (10×10×5 mm, purity > 99.95%, MTI Corporation) was used as a high temperature insulating substrate on which a 200 nm Pt film and Pt posts were pre-patterned with a 200 nm $SrCo_{0.8}Nb_{0.2}O_{3-\delta}$ (referred to as SCN20 hereafter) coating to create two electrode contact regions as shown in Figure 2.5.

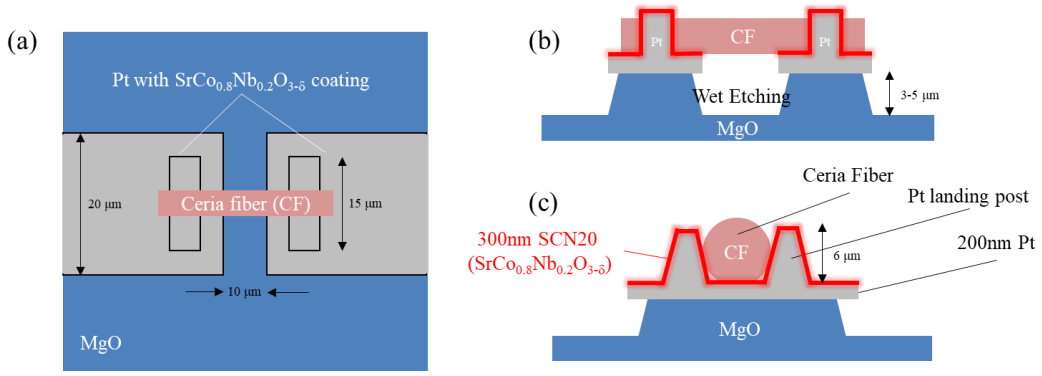

Figure 2.5 Schematic of the fabricated device for in-plane fiber measurement : (a) top-down view. (b)-(c) side view.

More specifically, the device was fabricated using the following steps:

(1) Pt film patterning: 200 nm thick Pt film was patterned by conventional photolithography to create a base structure by AJA Orion Sputter System using Pt target (purity 99.99%, AJA International, Inc) with a deposition rate of 1 Å / s. The Pt film was used as the base electrodes (a 10 μm gap between electrodes);

(2) Pt posts patterning: four Pt posts for securing the fiber sample (two posts on each side) were grown by ion beam induced deposition (FEI Helios Nanolab SEM / FIB) on the prepatterned Pt film. The dimension of each Pt post was 6×3 μm at the bottom and 3×1 μm at the top with a total height of more than 6 μm (deposition time ~13min, 93pA, 30 kV). A polymer mask (S1813) was used to protect the substrate, especially the gap between the electrodes, from Ga^+ contamination from deposition and imaging. To remove the polymer mask, subsequent to past fabrication, the whole device was soaked in Remover 1165 with sonication;

(3) Wet etching: the device was soaked in Nanostrip (90% Sulfuric acid and <1% Hydrogen peroxide) for 10 min, followed by 50 vol % H_3PO_4 for 10 min at 60 °C which caused the exposed MgO surface to be etched by 3-5 μm. By including this step, the leakage through the substrate between two electrodes was heavily reduced.

(4) SCN20 Coating: a 200 nm thick layer of SCN20 was deposited on the Pt posts and Pt film by photolithography and pulsed laser deposition (PLD) as a contact layer between Pt posts and fibers. SCN20, a mixed ionic and electronic conductor, has high activity for oxygen electroreduction and can reduce the electrode contribution to the impedance measurement[43–46].

After the device was fabricated, a single fiber was loaded into the device using an omniprobe in a FIB chamber. Prior to fiber measurement, the structure was annealed at 600 °C in air for 30 min. This step was taken to remove hydroxyl groups on the surface of the hygroscopic MgO substrate, as well as carbon impurities in the Pt posts. Such impurities are known to be incorporated into Pt during ion beam deposition and reduce its conductivity[47]. Au wires of 0.2 mm thickness were used to connect the device for impedance spectroscopy.

2.2.4 High Impedance Measurement

Alternating current impedance spectroscopy (ACIS) was used to probe the transport properties across single grain boundaries in 6 μm thick fibers. The impedance of a single fiber (20 μm long and 6 μm thick) is estimated to be 1.6 GΩ at 550 °C and increase rapidly to 1000 GΩ at 350 °C in air based on bulk and grain boundary conductivity from impedance measurement on the comparative fiberboard. The extremely high impedances measured across fibers have required

implementation of a Faraday cage, electronic upgrades to impedance system, and careful impedance measurements, which will be discussed below.

1. Faraday Cage

A Faraday cage is an enclosure made of conductive materials that block electric fields from the environment and minimize noise in sensitive electronic measurements. The screening mechanism is that the external electrical fields cause electric charges in the conductive materials to redistribute over the cage such that they cancel the field inside the cage. The cage is usually grounded to dissipate any electric currents generated from external or internal electromagnetic fields that would otherwise disrupt the measurement.

The fibers as-measured have extremely high impedance due to unfavorable geometry: large length and small cross-sectional area. When a voltage is applied to a fiber, the generated current is so small (~2 pA at 450°C) that the signal is overwhelmed by large electrical noise from the environment (~10^4 pA noise perturbation was detected when fibers were heated inside a furnace tube), usually giving an unreasonable result. Therefore, the Faraday cage is used to screen external electric noise.

In the experiment, samples were measured at elevated temperature by impedance analyzer with a Faraday cage. The Faraday cage had two parts (both grounded) connected to each as shown in Figure 2.6. The furnace part was made of stainless steel 316 (SST316) mesh, fully surrounding the sample inside the furnace tube to screen the electrical noise from heating elements. SST 316 mesh has high phase stability and satisfying conductivity at elevated temperature qualifying it as an appropriate screening material. In order to keep the mesh from touching the samples and causing

a short circuit, a dual-tube system was used in which another smaller tube was placed between the mesh and the sample. The wire connection part outside of the furnace was made of copper mesh which was used to block noise signals from the lab environment. According to electrical noise tests, the impedance modulus of several TΩ (Terra Ohm, 10^{12}Ω) and the capacitance of 0.01 pF (Pico Farad, 10^{-12}F) could be measured.

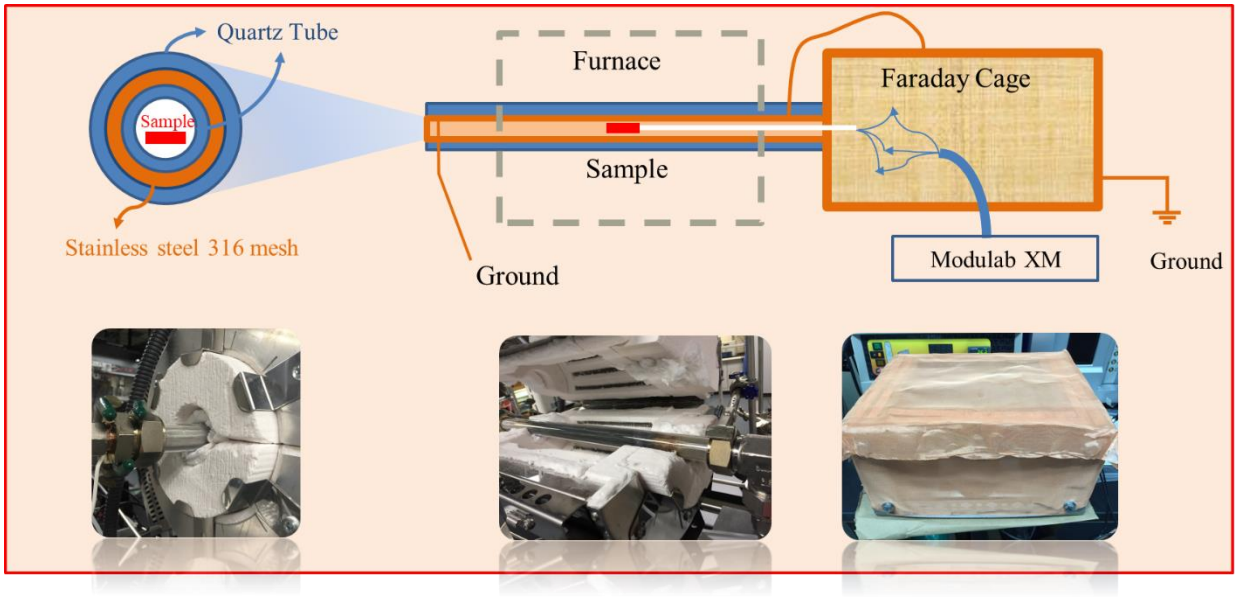

Figure 2.6 Schematic of Faraday Cage used in ultrahigh impedance station

2. Electronic Upgrade

An electronic upgrade was installed in our outdated instrument to improve the ability to measure ultrahigh impedance. According to calculation, fibers have an average 23 GΩ impedance at 450 °C in air which means they have 2 pA current travelling through them when 50 mV AC

amplitude is applied. To accurately measure such a low current through the samples, the impedance analyzer (Modulab XM, Solartron Analytical) is upgraded with the XM Femto Ampere card, which is able to detect current values as low as 1fA (=10^{-15} A) with the use of a Faraday cage.

A standard 100 GΩ resistor was tested with the upgraded XM Modulab, which showcased its superior measurement of ultrahigh impedance with high stability and accuracy as seen in Figure 2.7 (a) compared to the result from the outdated Modulab as seen in Figure 2.7 (b). It is clear from Figure 2.7 (b) that the outdated Modulab impedance results at high frequency range showed obvious artifacts.

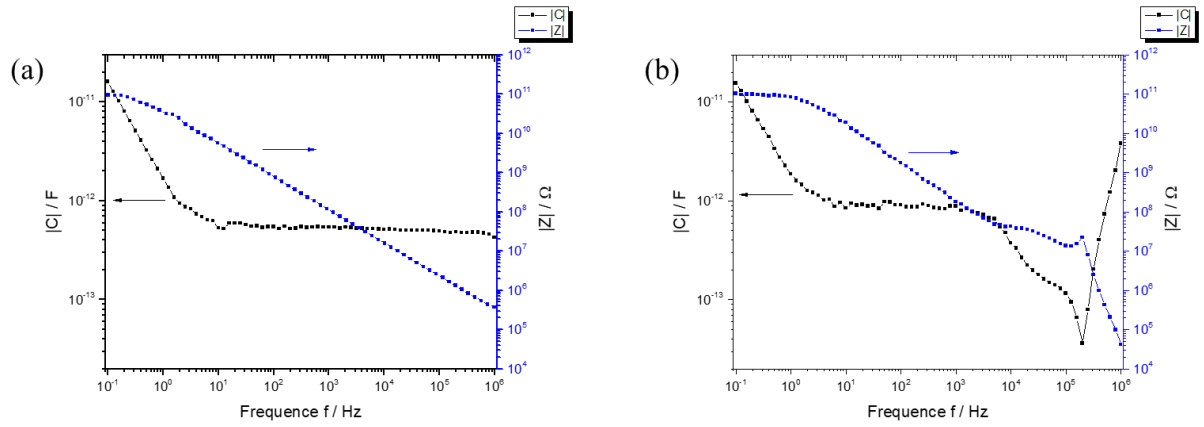

Figure 2.7 Impedance measurement on 100 GΩ standard resistor by (a) upgraded Modulab (b) outdated Modulab (AC amplitude=50 mV, Frequency range=1MHz to 0.1Hz, Integration time=1s, Cycle=1)

3. Impedance Spectroscopy

Impedance spectroscopy is usually employed to separately determine global grain boundary resistance and bulk resistance for polycrystalline samples. Impedance measurement requires a small sinusoidal voltage perturbation to be applied to an equilibrated system, and the corresponding current response is measured. The ratio of the voltage perturbation to the current response is the impedance.

Individual transport steps in multistep processes can be effectively characterized by impedance spectroscopy. Ideally each step has a unique time constant associated with it and can be separated in the frequency domain. A particularly useful way to represent impedance spectra is the Nyquist plot, which is a plot of the impedance in the complex plane, $-z''$ (minus imaginary component of the impedance) against z' (real component of the impedance), which are parametric functions of frequency. In the Nyquist plot, each transport step with a sufficiently different characteristic time constant is represented by a unique arc. Specifically, for an ideal polycrystalline sample, the responses from the bulk, the grain boundaries and the electrodes are well resolved and appear in the plot from high frequency (MHz) to low frequency range (mHz) in the sequence shown in Figure 2.8.

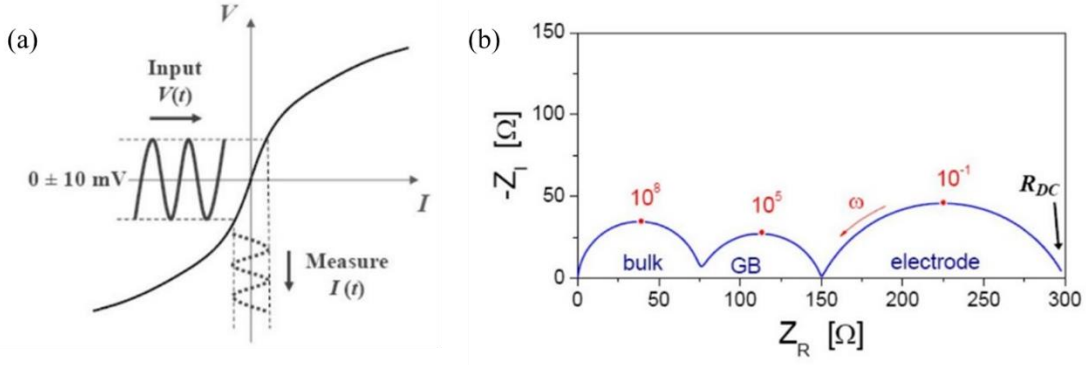

Figure 2.8 Impedance spectroscopy and Nyquist representation : (a) the depiction of an alternating voltage perturbation and current response in relation to a generic polarization curve, and (b) impedance spectrum sketch, in a Nyquist representation, for a polycrystalline material showing arcs for electrolyte processes (bulk and grain boundary) and electrode processes. Reproduced from Ref. [48].

Electrical conductivity of fiber samples was measured by impedance spectroscopy in a 3 Terminal (3T) configuration as shown in Figure 2.9[49]. The ModuLab XM system uses a feedback control loop where the contour electrode (CE) and the reference electrode 1 (RE1) are connected to one side of the electrodes while working electrode (WE) is connected to the other side. For low current electrochemistry, greater accuracy is obtained by using a modified version of the control loop where the reference electrode 2 (RE2) is disconnected from WE and connected to the ground (LO).

Impedance spectra were collected under the flow of synthetic air, supplied at a space velocity of 10 cm/min. The sample temperature was varied from 600 °C to 300 °C in 50 °C

decrements. The combination of undoping, unfavorable fiber geometry and moderate temperatures resulted in extremely high measured impedance, which necessitated the use of a Faraday cage to block electrical noise from the environment. Impedance spectra were recorded on cooling, after a dwell time of 1-2 hours at each temperature to reach equilibrium. Data were collected using a Modulab XM frequency response analyzer equipped with a Femto Ammeter mode, at frequencies from 1 MHz to 0.01 Hz and at a zero-bias perturbation amplitude of 50 mV.

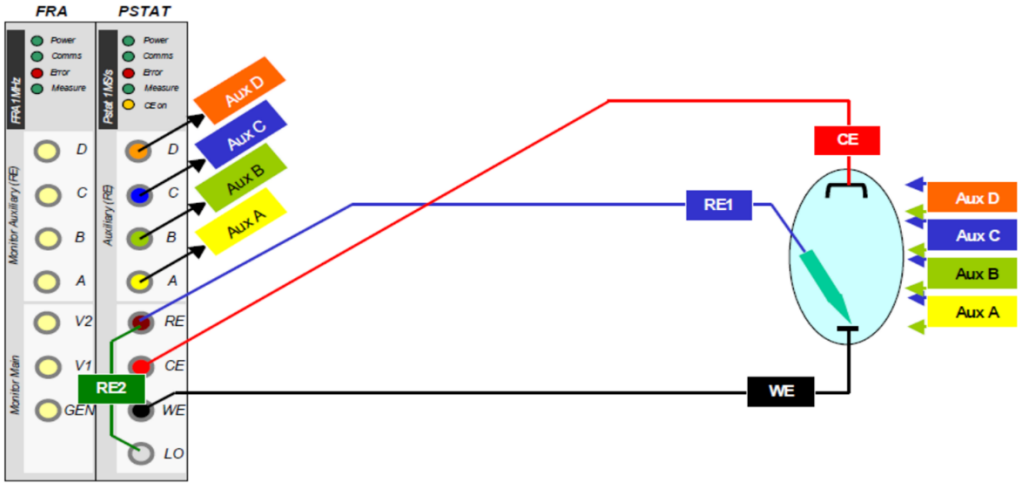

Figure 2.9 The 3T connection diagram for measuring low current in Modulab XM installed with Femto Ammeter card.

3 Direct Grain Boundary Study in Ceria Compact

3.1 Abstract

A number of grain boundary phenomena in ionic materials, in particular, both depressed and enhanced charge transport characteristics, have been attributed to space charge effects. Developing effective strategies to manipulate transport behavior requires deep knowledge of the origins of the interfacial charge, as well as its variability within a polycrystalline sample with millions of unique grain boundaries. Electron holography is a powerful technique uniquely suited for studying the electric potential profile at individual grain boundaries, whereas atom probe tomography provides exquisite access to the chemical identify of essentially every atom at individual grain boundaries. Using these two techniques, we show here that the space charge potential at grain boundaries in lightly doped, high purity ceria can vary by almost an order of magnitude. We further find that trace impurities (< 25 ppm), rather than inherent thermodynamic factors, may be the ultimate source of grain boundary charge, suggesting chemical tunability.

3.2 Electrical Properties of 0.2 at% Sm doped Ceria

3.2.1 Microstructure

To ensure a wide space charge zone and facilitate its detection, we employed ceria with a low dopant concentration, just 0.2 at% Sm. According to the Mott-Schottky model (which takes the dopant concentration profile to be flat and the grain boundary core to be infinitesimally thin)[12], the half-width of the space charge zone, extending from the grain boundary core at $x = 0$ into the adjacent grains, is

$$\lambda = \sqrt{-\frac{2\varepsilon_r \varepsilon_0 \Delta\varphi_0}{z_d e c_d}} \tag{3.1}$$

where $\Delta\varphi_0$ is the space charge potential (the difference between the potential at the grain boundary core and that in the bulk), ε_r is the relative dielectric constant, z_d is the effective valence of the dopant (= -1), e is the elementary charge, and c_d is the volumetric concentration of the trivalent dopant, which resides on the Ce site within the fluorite structure of ceria. For typical values of $\Delta\varphi_0$ and relative dielectric constant in doped ceria (0.2-0.5 V and 20-60, respectively, depending on composition)[50–52], the dopant concentration of 0.2 at% implies $\lambda =$ 3-8 nm, substantially larger than the spatial resolution of the electric potential measurements.

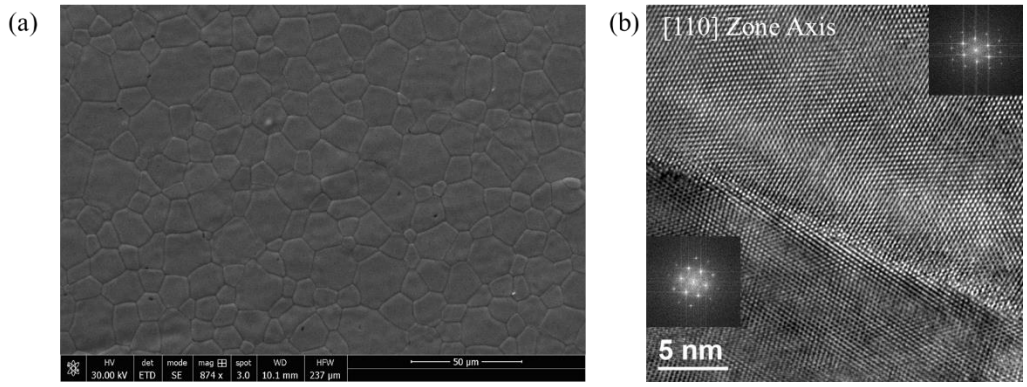

Figure 3.1 Microstructure of sintered 0.2 at% Sm doped ceria bulk and grain boundary : (a) scanning electron microscopy image of as-sintered of 0.2 at% Sm doped ceria; (b) transmission electron microscopy image of a representative grain boundary in 0.2 at% Sm doped ceria. Fast Fourier Transform (FFT) of adjacent grains shows the tilt is about the [110] zone axis.

Samples of 0.2 at% Sm-doped ceria, hereafter simply referred to as ceria, were prepared for this study from ultra-high purity starting materials using conventional ceramics processing techniques. After sintering, the grain size was measured to be 12.5 ± 1.2 μm, Figure 3.1 (a). The grain boundaries, as evident from the representative TEM image presented in Figure 3.1 (b), were sharply defined and free of any amorphous phases. The crystallographically visible thickness, which corresponds to the thickness of the grain boundary core, is 1-2 nm.

3.2.2 SuperX Energy Dispersive Spectroscopy

Grain boundary composition data were collected using a FEI Talos F200X TEM/STEM equipped with a Super-X EDS detector and operated at 200 keV. The sample was mounted on a

Molybdenum (Mo) grid (PELCO® Aperture Grids), selected to minimize the background signal from impurity elements. The Mo grid offers the lowest impurity level amongst the available choices, with Al < 20ppm, Ca < 20ppm, Mg < 20ppm, and Si < 50ppm; the only other significant impurities in the Mo grid, Fe < 50 ppm and Cr < 50 ppm, are not relevant to the present study. The elemental maps in Figure 3.2 (d)-(h) are collected for a counting period of 843 s and are featureless, indicating that impurities are below the detection level. The absence of a signal due to Sm in (i), even when the counting time is increased to 2147 s, indicates the detection limit must be higher than 0.07 at % (0.2 cation %). In this measurement the total number of counts exceeds the recommended value of 10^6 over the energy range of analysis for establishing the detection limit.[53] It is noted that the Sm-Lα1 peaks overlaps the Ce-Lβ2 peak, and accordingly, the Sm-Lβ1 peak is used for asserting Sm detectability.

Within the detection limits of conventional energy dispersive X-ray spectroscopy carried out in conjunction with the imaging, no impurities were found at the grain boundaries. As described below, however, greater sensitivity could be achieved by atom probe tomography.

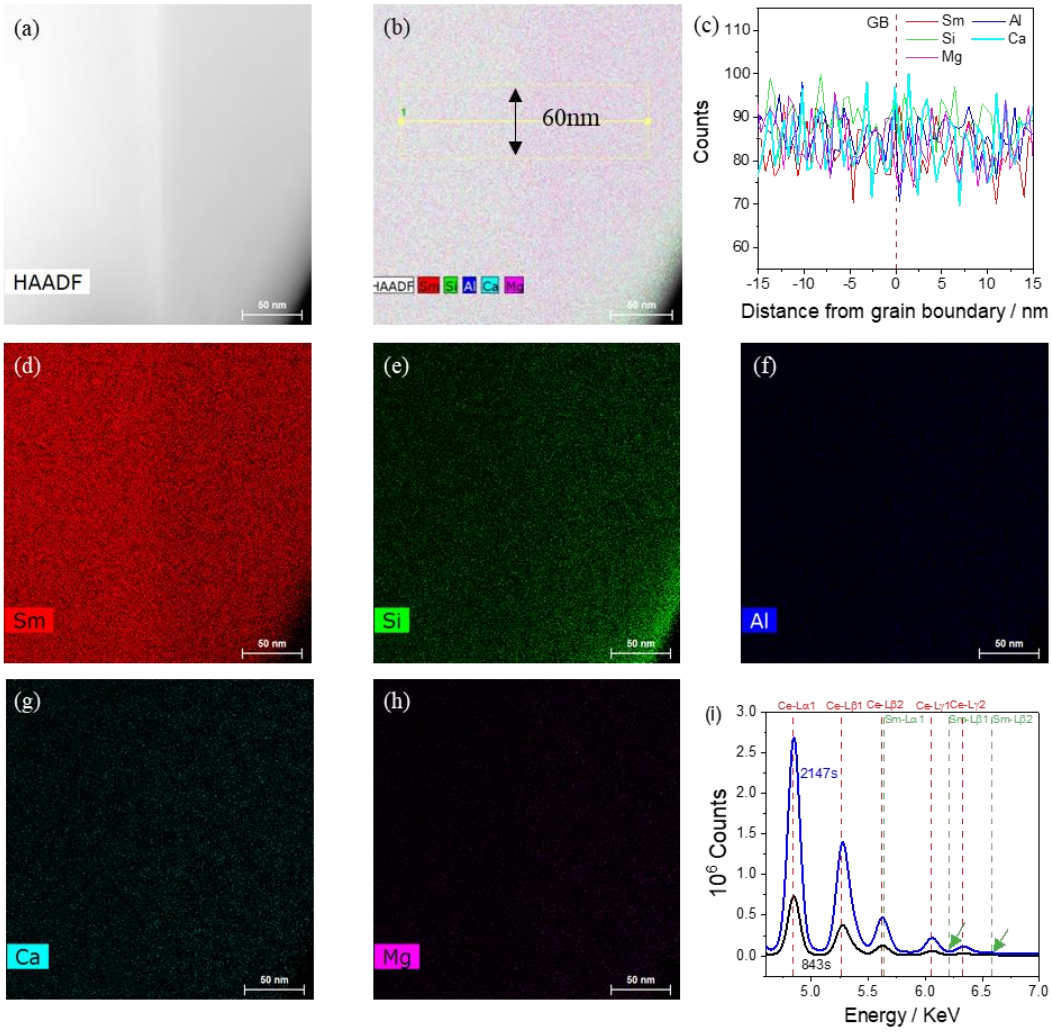

Figure 3.2 EDS analysis of a representative grain boundary, carried out in conjunction with transmission electron microscopy : (a) high-angle annular dark field image showing location of grain boundary; (b) composite elemental map for Sm, Si, Al, Ca, and Mg (c) integrated counts for these elements over the area shown in (b); (d)-(h) individual elemental maps for the respective elements; and (i) energy resolved spectra over the range for the Ce and Sm peaks directly on the grain boundary collected using two different counting times, as indicated.

3.2.3 Impedance Spectroscopy

Electrical impedance spectroscopy revealed high impedance at the grain boundaries, as well as in the bulk, in Figure 3.3. High resistivity is expected due to the very low dopant concentration, and particular care was employed in the measurements in order to accurately record the spectra. The data were analyzed by equivalent circuit fitting, which yielded the bulk and grain boundary resistances and their equivalent capacitances at each measurement temperature. The bulk conductivity was simply determined by accounting for the sample dimensions. The specific grain boundary conductivity was calculated from the impedance fit parameters within the framework of the brick-layer model[54] using the expression $\sigma_{gb} = \frac{1}{R_{gb}}\left(\frac{L}{A}\right)\left(\frac{C_{bulk}}{C_{gb}}\right)$, where C_{bulk} and C_{gb} are the bulk and grain boundary capacitances, respectively, and R_{gb} is the grain boundary resistance. This expression accounts for the fact that the total length of grain boundary material that contributes to the measured grain boundary resistance is only a small fraction of the sample length, where that fraction is approximated by $\frac{C_{bulk}}{C_{gb}}$. A single, temperature-averaged capacitance ratio was employed for the calculation. We find the grain boundary conductivity to be 5 orders of magnitude smaller than that of the bulk, Figure 3.3 (c), with an activation energy, 1.51 ± 0.01 eV, that is somewhat higher than that of the bulk, 1.31 eV (statistical uncertainty < 0.001 eV). While lower grain boundary than bulk conductivity is commonly reported, such a large difference is rare, and has appeared in the literature on ceria only in connection with low dopant concentration.[50,55,56]

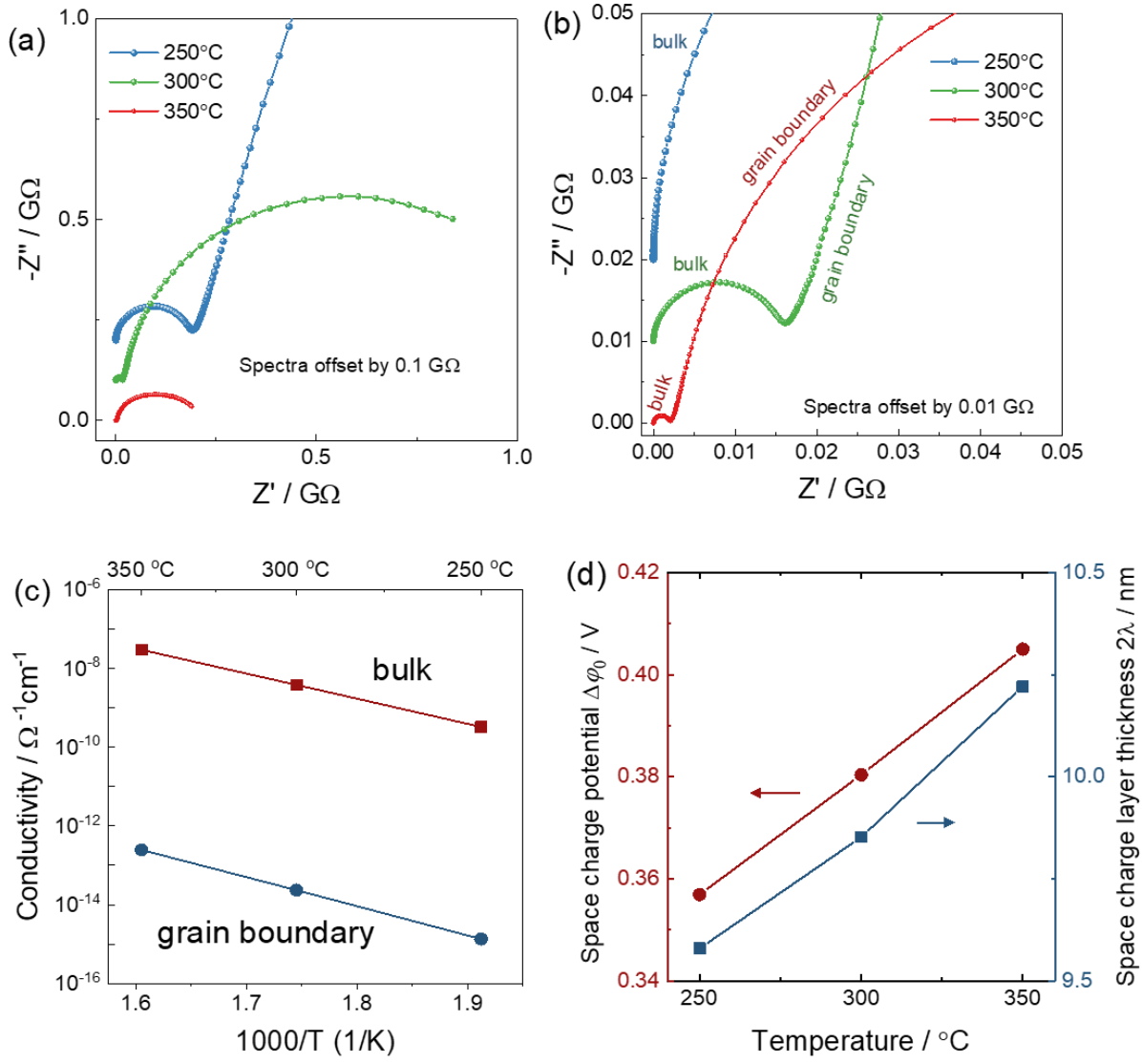

Figure 3.3 Macroscopic transport properties of polycrystalline 0.2 at% Sm doped ceria (grain size 12.5 ± 1.2 μm) under synthetic air : (a) impedance spectra and (b) expanded spectra, collected at the temperatures indicated; (c) bulk and specific grain boundary conductivity determined from equivalent circuit fitting; and (d) space charge potential and space charge layer thickness inferred from a Mott-Schottky analysis.

The average space charge potential was estimated using the expression[8]

$$\frac{\sigma_{bulk}}{\sigma_{gb}} = \frac{e^{(ez\Delta\varphi_0/kT)}}{2ez\Delta\varphi_0 / kT} \tag{3.2}$$

which follows from the Mott-Schottky model, and an assumption that, other than a depletion of carriers, the properties in the bulk and space charge regions are the same. Here, *k* is Boltzmann's constant, *T* is temperature, and *z* is the effective valence of the mobile species (+2 in the case of oxygen vacancies). The derived space charge potential, Figure 3.3 (d), is 0.38 V at 300 °C, and rises with temperature. From a Taylor expansion of Eq. (3.3) the activation energies for bulk and grain boundary transport (E_{bulk} and E_{gb}, respectively) are expected to obey the relationship [55]

$$E_{gb} \approx E_{bulk} + 2e\left\{\Delta\varphi_0\big|_{1/T=0} + \frac{1}{T}\frac{\partial\Delta\varphi_0}{\partial(1/T)}\right\} \tag{3.3}$$

The grain boundary activation energy expected from this expression is ≈ 2.1 eV. While the agreement with the measured value (1.51 eV) is moderate, the observation of a higher activation energy for grain boundary transport agrees with the prediction. The space charge potential measured here (0.36 – 0.41 V) is consistent with the value of 0.41 V we obtain by extrapolation to 300 °C of the bulk and GB conductivities of 0.1 at% Y doped ceria, reported by Guo et al. for the range of 400 to 800 °C.[50] These authors furthermore also find a grain boundary conductivity that is 5-6 orders of magnitude lower than in the bulk. Similarly, Avila-Paredes et al.[55] report a six orders of magnitude difference at 300 °C between bulk and grain boundary conductivity in Gd-doped ceria when the dopant concentration is 1 at%.

3.3 Grain Boundary Potential Unveiled by Electron Holography

3.3.1 Electric Potential Mapping

Off-axis electron holography (OAEH) in a transmission electron microscope offers a unique capability to directly reveal, with nanometer spatial resolution and high sensitivity, the electric field in a material.[57] By splitting a coherent electron beam into two components, one which passes through the sample and one which passes through vacuum, and recombining them, one generates an interference pattern or hologram from which the phase shift and scattering amplitude of the electrons due to interaction with the sample can be reconstructed. Encoded in this reconstruction is the electrostatic potential within the material. The method has been effectively employed for the study of grain boundaries in $SrTiO_3$,[58–60] demonstrating the viability of the approach. Furthermore, the instrument employed here achieves a spatial resolution of ~ 0.6 nm and voltage resolution ~ 0.2 V, values that are well suited to an investigation of grain boundaries in lightly doped ceria

Electron holography measurements, aimed at directly detecting the electric potential and probing the boundary-to-boundary variations, were performed on a total of ten grain boundaries, with sensitivity analysis performed using measurement made through vacuum (see Chapter 3.3.4). The temperature was held at 300 °C for direct comparison with the impedance measurements. Despite the vacuum conditions, the free electron (Ce^{3+}) concentration at grain boundaries is expected to remain negligible at this temperature.[50] In five cases, we were successful in identifying boundaries in which the grains on either side where aligned along the [110] zone axis (for example Figure 3.1). A representative hologram from one of these five samples is shown in Figure 3.4.

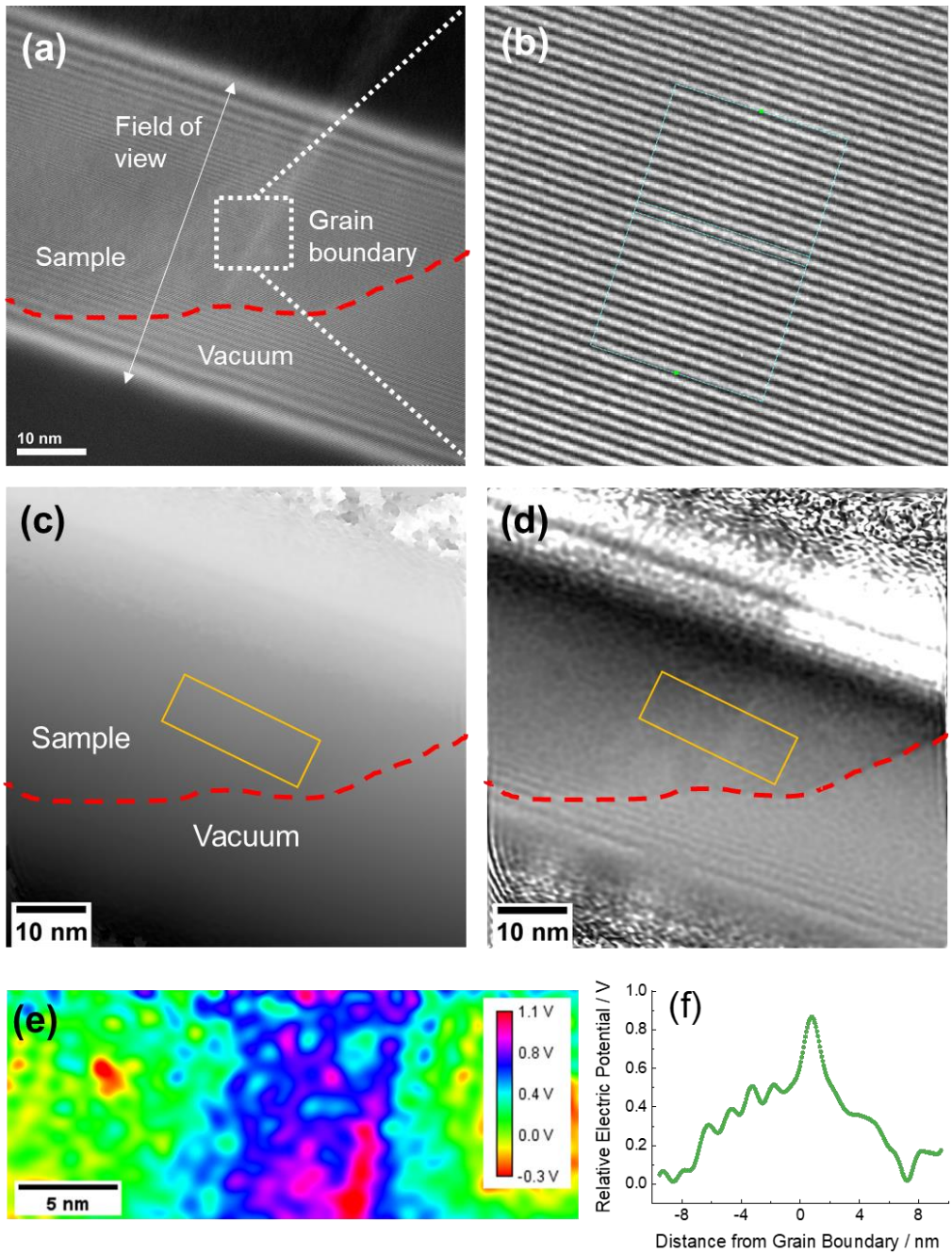

Figure 3.4 Electron holographic imaging of a representative grain boundary in 0.2 at% Sm doped ceria : (a) hologram over a 48 nm field of view, (b) zoomed in view of (a) showing fringe contrast of 35%; (c) reconstructed phase map; (d) reconstructed amplitude map; (e) reconstructed potential map of the yellow boxed region in (c) and (d); and (f) electric potential profile, as integrated over

all of the area depicted in (e), with the bulk potential set to zero. Red dashed line in (a), (c) and (d) corresponds to the edge of the sample.

Prior to recording the image, the sample was tilted slightly away from the zone axis so as to diminish the diffraction contrast that can hinder/create artifacts in the phase reconstruction in electron holography, Figure 3.5.

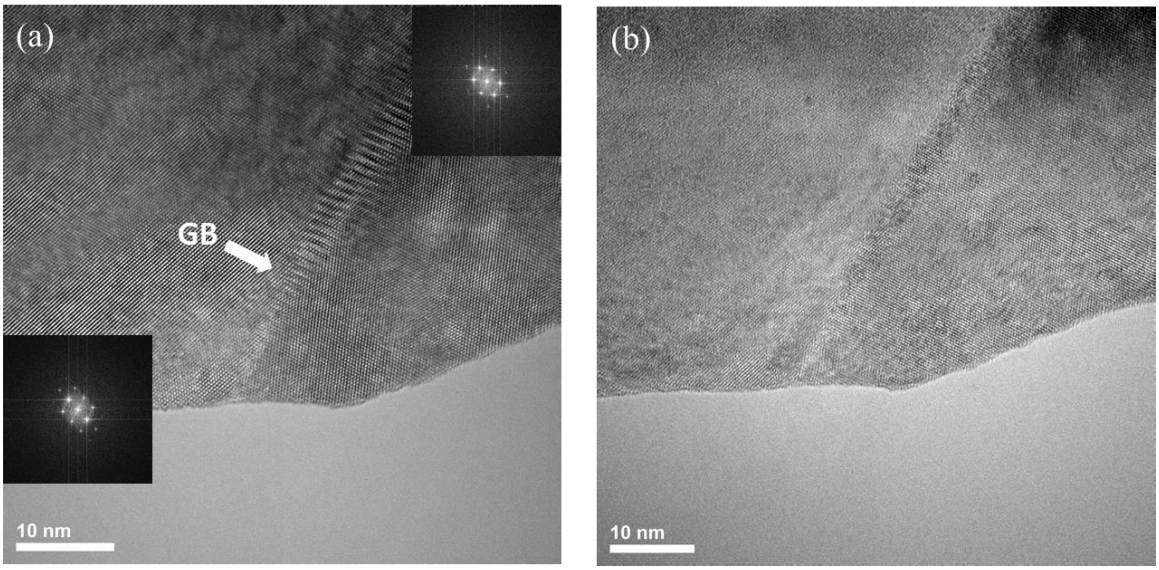

Figure 3.5 Transmission electron microscopy image of a representative grain boundary : (a) aligned along the [110] zone axis, with the FFT images of the two grains shown; and (b) tilted away from the zone axis.

The reconstructed phase map, $\Delta\theta(x, y)$, Figure 3.4 (c), showing the phase shift relative to vacuum, carries the desired information about the electric potential profile. Specifically, under the

assumption of a potential that is invariant along the z direction within the sample, $\Delta\theta(x,y) = C_E \int V(x,y,z)dz = C_E V_p(x,y)t$, where $V_p(x,y)$ is the projected average electric potential, t is the sample thickness, and C_E is the interaction constant equal to 0.00728 $rad/(V \cdot nm)$ for 200 keV electrons. The thickness is obtained from the amplitude map, Figure 3.4 (d), according to the expression[61] $t/\lambda_e = -2\ln(A_0/A_r)$ where t is the sample thickness, λ_e is the inelastic mean free path of electrons in the material, A_0 is the amplitude from the sample region in the hologram, and A_r is the amplitude from the vacuum region. Using a parameterization of λ_e based on inelastic-scattering theory and the Kramers-Kronig sum rule,[53,62] the mean free path in ceria was estimated to be 92 nm. Thus, all information for generating the potential map is available.

Following these methods, we found a clear electrical signature of the grain boundary, with a significant positive electric field over a region almost 20 nm in breadth and a peak potential of 0.88 V, Figure 3.4 (e,f). Results from eight other grain boundaries were qualitatively similar, Figure 3.6. Grains in images 1,2,5,6,9 are [110] zone axis aligned, whereas as those in grain boundary images 3,4,7,8 have random oriented. GB5 is that shown in Figure 3.4.

In addition to the 10 measurements across grain boundaries, 9 measurements were made far from boundaries, from which the mean inner potential of ceria was determined to be 19 ± 3 V. The value is consistent with that calculated using electron scattering factors, 17 V (see Chapter 3.3.4).

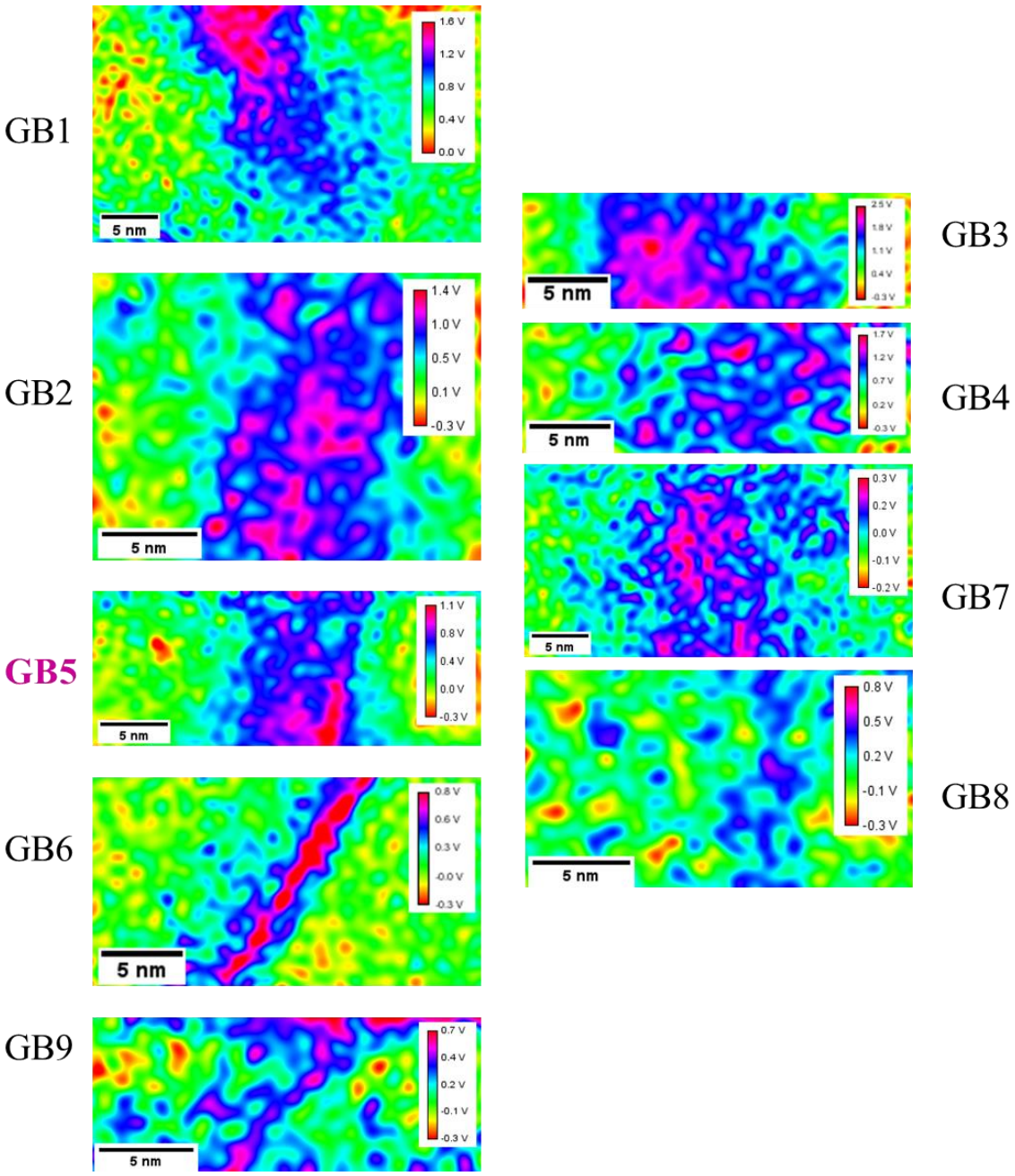

Figure 3.6 Electric potential maps obtained from 9 samples with clearly evident grain boundaries

To determine the space charge potential for each grain boundary, we corrected the data for two features of the experiment: (i) the grain boundary may not necessarily lie parallel to the electron beam, Figure 3.7 (a), and (ii) if the electric field is indeed high at the grain boundary, the field will leak into the vacuum surrounding the sample, Figure 3.7 (b). The non-ideal orientation of the grain boundary has the consequence of broadening the electric potential profile and decreasing the peak value relative to what would be measured in the desired orientation. The electric leakage causes an over estimation of the electric field in the sample because the electrons will undergo a phase shift due to the leakage field in addition to that due to the field within the sample.

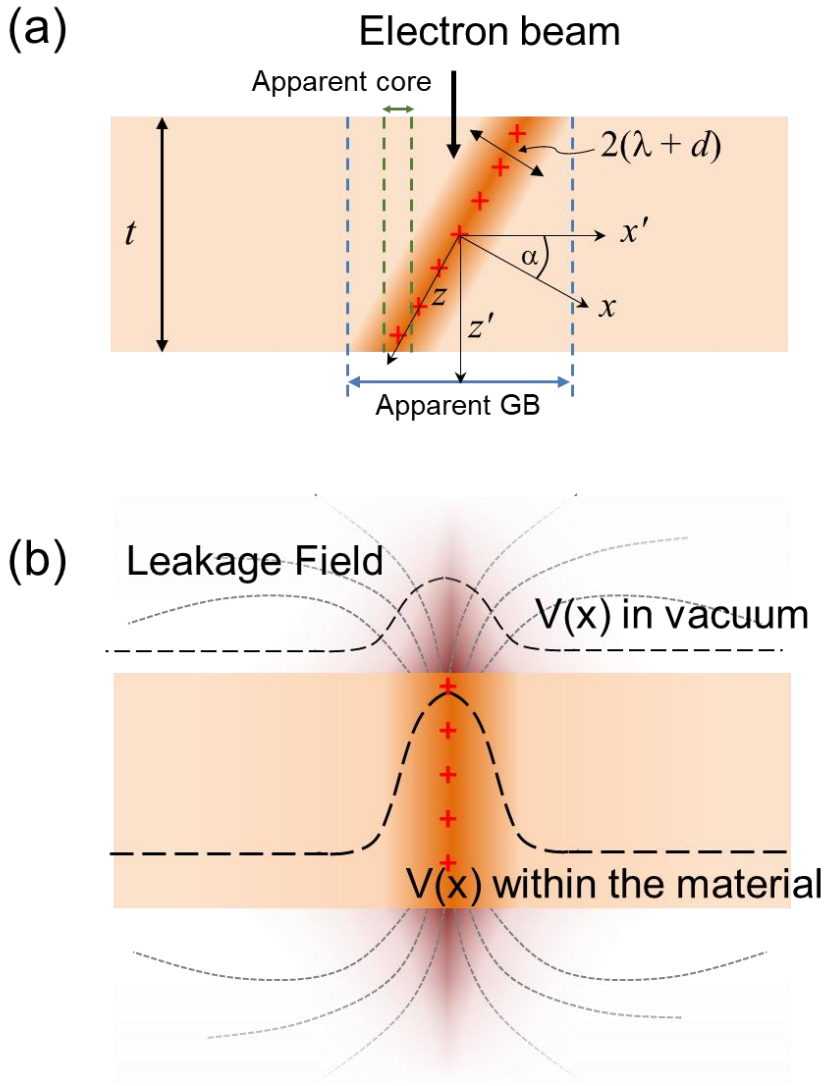

Figure 3.7 Schematics of factors impacting measured electric field associated with grain boundary space charge effects : (a) misalignment of grain with finite core thickness; and (b) leakage of electric field into vacuum.

3.3.2 Tilt Correction

In the analysis of space charge potential, we treated the effect of the grain boundary misorientation relative to the electron beam direction by recognizing that the thickness-averaged electric field, $\bar{V}(x')$, recorded in the holography experiment, Figure 3.7 (a), is given by

$$\bar{V}(x') = \frac{1}{t}\int_{-t/2}^{t/2} V(x',z')dz' = \frac{1}{t}\int_{-t/2}^{t/2} \Delta\varphi\big((x'\cos\alpha - z'\sin\alpha)\big)dz' \approx \frac{1}{t}\int_{-t/2}^{t/2} \Delta\varphi\big(x' - z'\alpha\big)dz' \quad (3.4)$$

where $\{x_i'\}$ refer to coordinates in the experimental reference frame, $\{x_i\}$ to those of the grain boundary reference frame, α is the small tilt angle (rotation about *y*) between the two, and $\Delta\varphi(x)$ is the electric potential due to the charge at the grain boundary core. In projection on the image plane, a grain boundary with a core of thickness 2*d* has a crystallographically visible thickness of $t\tan(\alpha) + 2d/\cos(\alpha)$, providing a means for estimating α. For the grain boundary shown in Figure 3.4 and Figure 3.5, for example, the visible core thickness is 5.0 nm. The true crystallographic thickness (deduced from APT measurements) is ~ 1.6 nm, implying a tilt angle of 2.8°. Across the 9 grain boundary samples the value of α ranged from 0.8 to 9.0° shown in Figure 3.8. The grain boundary misorientation angle relative to the direction of the electron beam is as indicated in the legend for each figure, in which the fitted space charge potentials are also reported.

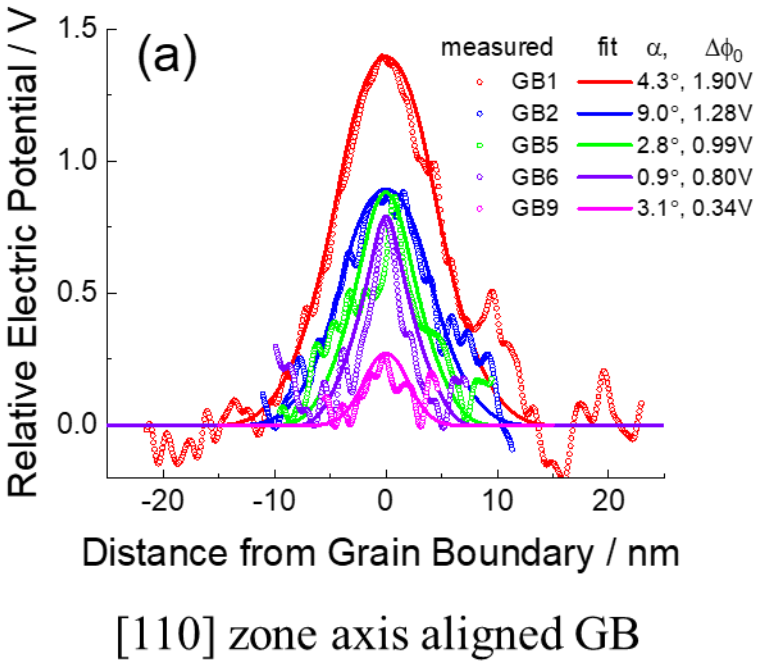

Figure 3.8 Fitting results for nine unique grain boundaries : (a) [110] zone-axis aligned grain boundaries; and (b) random grain boundaries.

Besides the tilt angle, application of Eq. (3.4) requires the functional form of $\Delta\varphi(x)$, which is *a priori* unknown. While the Mott-Schottky solution provides a reasonable first approximation, it is inconsistent with our experimental observation of a grain boundary core of finite thickness. Accordingly, we carried out an analysis accounting for a finite core, rather than the delta-function profile assumed in the Mott-Schottky treatment (see Chapter 1.3.3). Use of the resulting $\Delta\varphi(x)$ in Eq. (3.4) had the effect of decreasing the magnitude of the tilt correction to $\Delta\varphi_o$ relative to that derived from the Mott-Schottky potential profile.

The sensitivity of the deduced value of the space charge potential, $\Delta\varphi_o$, to variations in the core grain boundary thickness, 2*d*, was evaluated by the following procedure. Noting that the crystallographically visible core thickness, 2*d*′, to be related to the grain boundary misalignment angle, α, according to $2d' = t\tan(\alpha) + 2d/\cos(\alpha)$, we solve for α for each *d*. The measured $\bar{V}(x')$ was then represented according to Eq. (3.4) for several *d* and α pairs and a fit performed to obtain $\Delta\varphi_o$. A variation in the true grain boundary core thickness 2*d* from 0 (Mott-Schottky limit) to 2.0 nm produces a variation in $\Delta\varphi_o$ from 1.17 to 0.95 V, a range that is comparable to the ~ 0.2 V sensitivity of the measurement shown in Figure 3.9. While the impact of a finite core thickness is small, in order to avoid a systematic overestimation of $\Delta\varphi_o$, a finite core thickness, specifically $2d = 1.6$ nm, was used for all analyses.

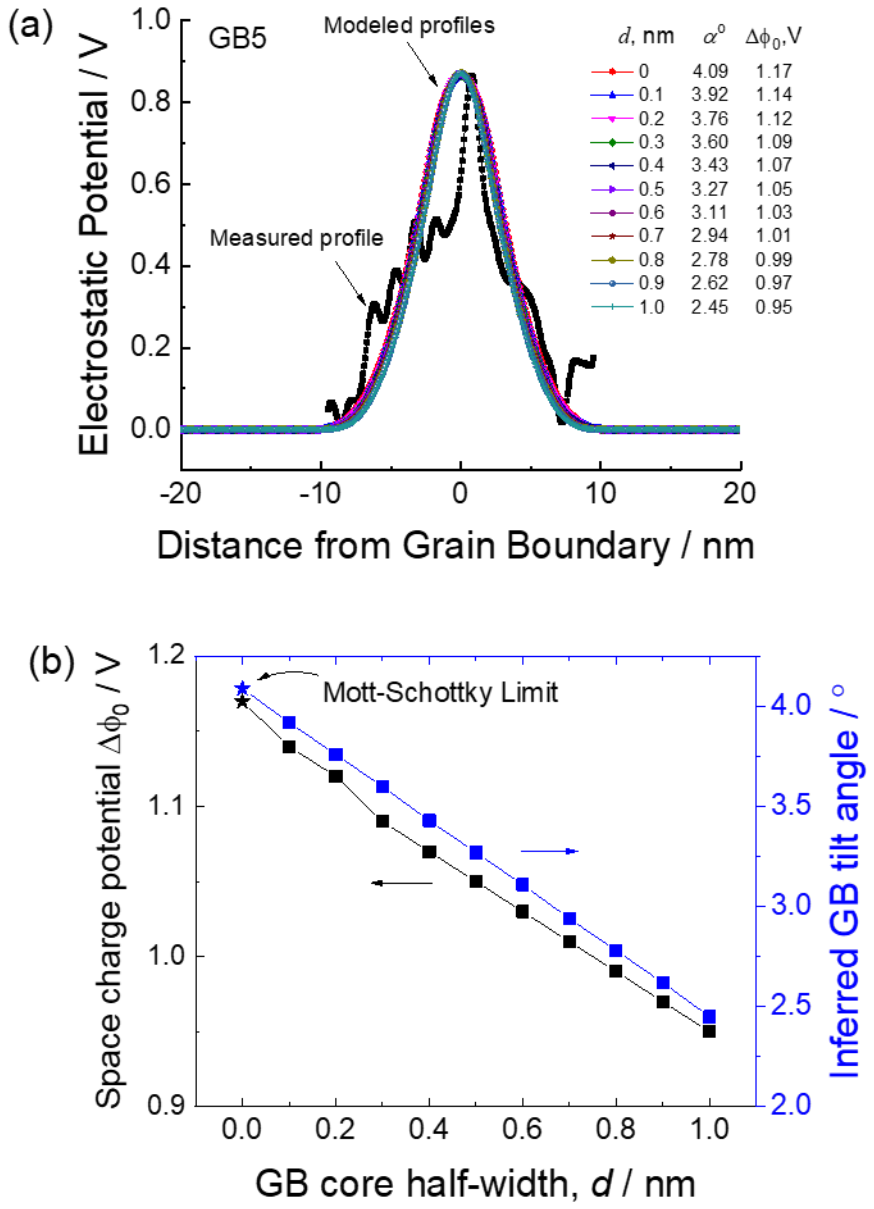

Figure 3.9 Effect of grain boundary core thickness effect on the space charge potential deduced by fitting to the experimental electric field profile : (a) fitted spectra, each with a different grain boundary core thickness between 0 and 1 nm; and (b) dependence of deduced space potential and grain boundary tilt angle on grain boundary core thickness

3.3.3 Leakage Correction

The electric field leakage, also addressed in this analysis, in principle impacts the entire $\bar{V}(x')$ profile, Figure 3.7 (b). We focused here on obtaining a corrected value for the space charge potential, which we approximated as $\Delta\varphi_o = \Delta\varphi_o^{raw} - \frac{\Delta\theta_{leak}}{C_E t}$, where $\Delta\varphi_o^{raw}$ is the tilt corrected space charge potential, $\Delta\theta_{leak}$ is the phase shift measured in the near-vicinity of the surface-terminating grain boundary and the thickness *t* is that of the sample. For the example grain boundary shown in Figure 3.4, we found $\Delta\theta_{leak}$ to be 0.11 rad, Figure 3.10, implying a correction of 0.18 V. The mere detection of a leakage field at the grain boundary termination provides additional direct evidence that the grain boundary has an electric potential that differs from that of the bulk. Furthermore, the magnitude of the leakage field (and associated correction) was correlated to the magnitude of the space charge potential, Figure 3.10 (c), as would be expected for an electric field perturbation occurring at the grain boundaries. High phase shift was found close to the GB core. All 9 GBs were characterized, and the leakage field correction voltage was plot against tilt-corrected space charge potential. It showed that the leakage contribution to electron phase shift was high in GB with large space charge potential.

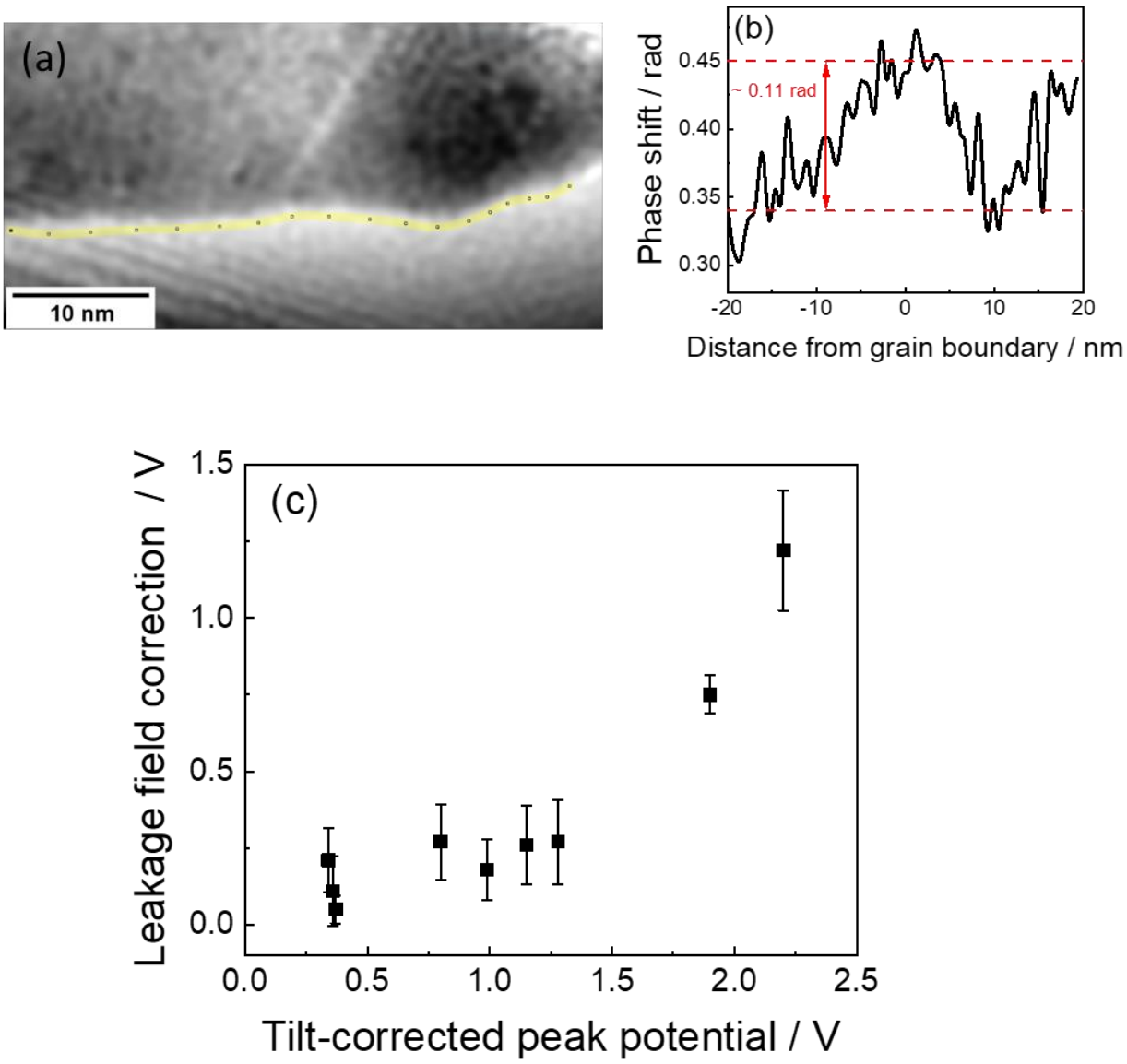

Figure 3.10 Magnitude of leakage field correction : (a) phase mapping of electrons in the near-vicinity of the surface-terminating grain boundary. (b) phase shift profile was plotted along the yellow line in (a). (c) Plot of leakage field correction voltage against tilt-corrected space charge potential.

The space charge potentials determined by these methods, Figure 3.11, displayed a remarkably wide range of values, from as large as 1.15 V to as small as 0.13 V. According to Eq. (3.2), the observed variation in $\Delta\varphi_o$ corresponds to a tremendous, indeed many orders of magnitude, variation in σ_{gb}. While extremely surprising, the result is not entirely unprecedented. In a study of lightly Fe-doped $SrTiO_3$ bicrystals, Zhang et al. found an enormous variation in transport properties, from barely detectable impedance at the boundary to hundreds of kΩ.[14] The macroscopically averaged impedance value of $\Delta\varphi_o$ of 0.38 V lies within the wide range of values determined by holography, but it is notably lower that the averaged value of 0.69 V from the 9 GBs represented in Figure 3.11 (a). The difference is likely due to over sampling of the high $\Delta\varphi_o$ boundaries as these are inherently amenable to electron holography studies. Perhaps even more remarkable than the breadth of recorded $\Delta\varphi_o$ values, was the occurrence of occasional grain boundaries at which no electrical perturbation at all could be detected (see Chapter 3.3.5). This completely unanticipated result indicates that a charged grain boundary core is ***not*** an inevitable feature of electrolyte materials.

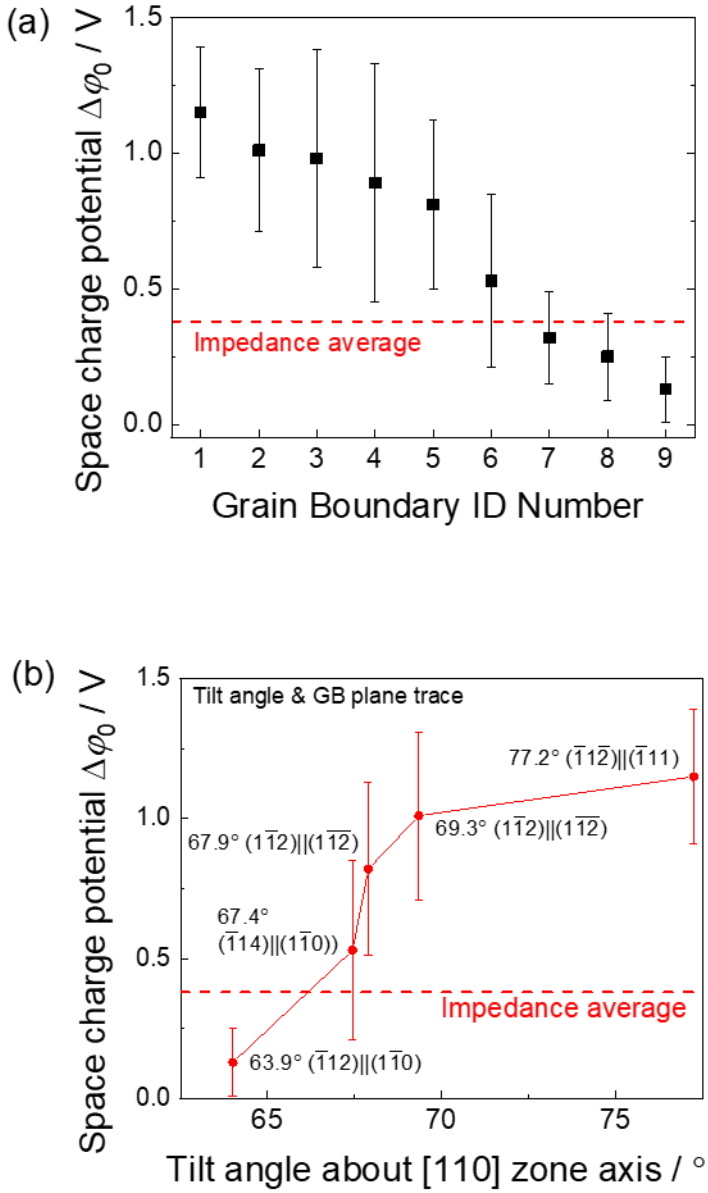

Figure 3.11 Grain boundary space charge potentials measured by electron holography for (a) nine unique grain boundaries and (b) a subset of [110] tilt grain boundaries as a function of tilt angle. Raw measured electric potential profile is corrected for grain boundary misalignment relative to the electron beam direction and electric field leakage into vacuum to obtain the values shown. In (b) the grain boundary tilt angles and plane traces are indicated.

Focusing attention on the [110] zone axis aligned grains, we find here that the space charge potential is highest when the grain-to-grain tilt angle is highest, Figure 3.11 (b). In their study of symmetrical, low-angle tilt grain boundaries in $SrTiO_3$ bi-crystals Zhang et al. similarly concluded (but on the basis of impedance measurements), that the space charge potential increases with increasing angle.[14] The steep variation in $\Delta\varphi_o$ recorded here as a function of [110] tilt angle is further reminiscent of the steep dependence of grain boundary energy in similarly fluorite-structured yttria-stabilized zirconia[63,64] and uranium dioxide[65], and even in cubic close-packed metals over the same angular range.[66,67] Whether the charge and transport characteristics derive from surface energy effects and are thus universal in their dependence on tilt angle remains to be determined.

3.3.4 Phase Detection Limit

Holograms were recorded using a Mollenstadt biprism and an exposure time of 5 seconds. The field of view in Figure 3.12 (a) is 48 nm and the resolution 31 pixels/nm. The intensity contrast in the zoomed region (b) is 38%, indicating a high quality recording;[38] the fringe spacing is 0.194 nm, implying lateral resolution of the reconstructed phase, amplitude and electric field maps of ~ 0.6 nm.

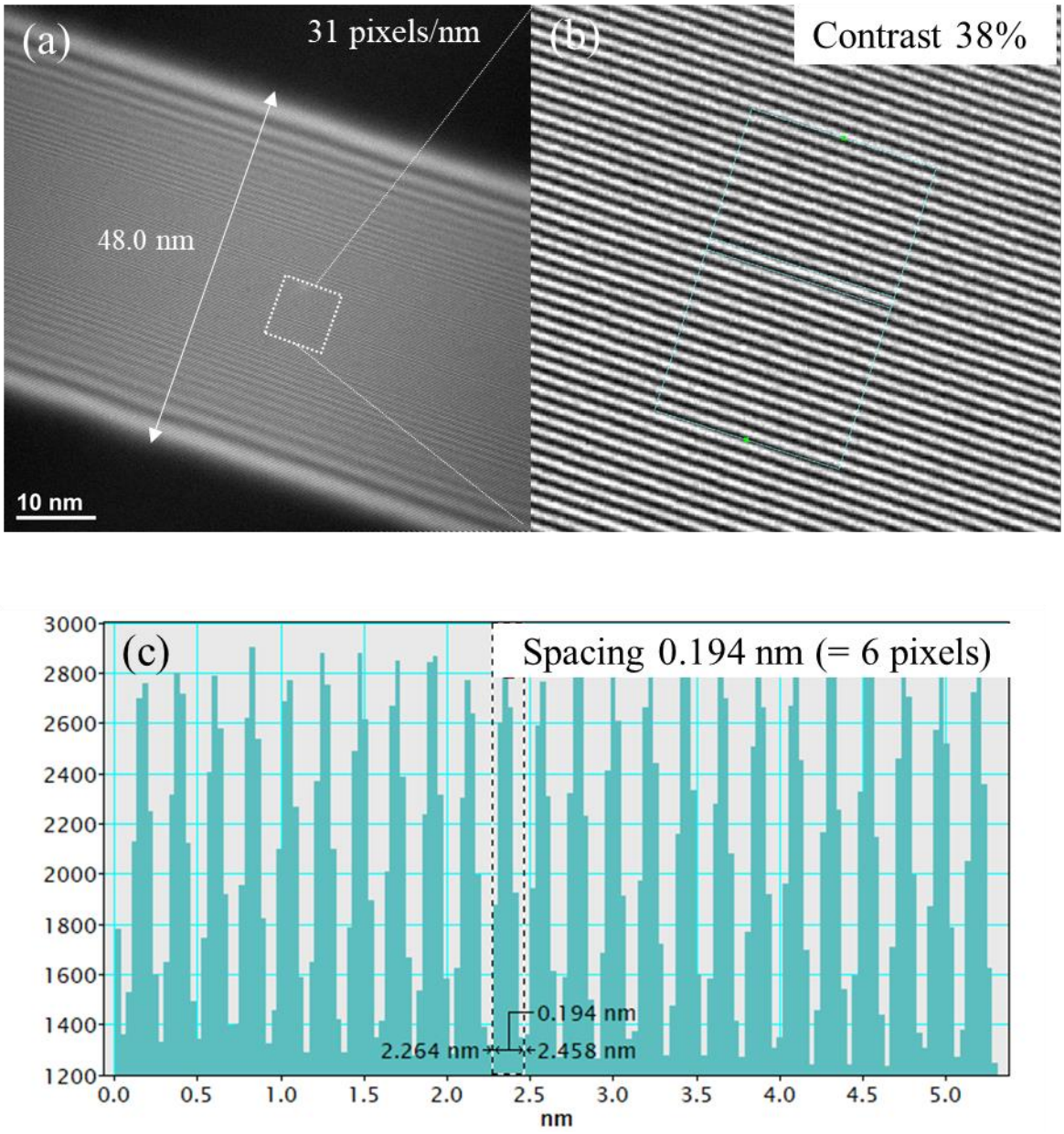

Figure 3.12 Hologram recorded using 100 V bias with electron beam traveling only through vacuum : (a) wide view hologram; (b) zoomed view as indicated; and (c) intensity profile obtained from region corresponding to (b).

The detection limit, σ_φ, was evaluated using the region of the hologram indicated in Figure 3.12 (b). This limit is given by $\sim \frac{\sqrt{2}}{C\sqrt{N_e}}$, where C is the fringe contrast $C = \frac{I_{\max} - I_{\min}}{I_{\max} + I_{\min}}$, and N_e is the number of detected electrons contributing to a give point in the reconstructed phase map.[68] As shown in (c) the average photon count per pixel is ~2082. For the CCD (Gatan Ultrascan CCD 4K × 4K) in the Tecnai F20, every electron generates six photons in the detector. In addition, the reconstruction was binned such that every four pixels in the hologram (2048 × 2048) contributed to one pixel in the phase map (1024 × 1024). Thus, the phase detection limit is

$$\sigma_\varphi \sim \frac{\sqrt{2}}{0.38 \times \sqrt{4 \times 2082/6}} = \frac{2\pi}{63} \qquad (3.5)$$

The measured phase detection limit is comparable to the value of about $\frac{2\pi}{60}$ reported by Lichte[69], using similar instrumentation.

The voltage detection limit in the presence of a sample is given by $V_{\lim} = \frac{\sigma_\varphi}{C_E t}$ the thickness of samples examined here ranged from 40 to 150 nm. Because the fringe contrast decreases with thickness, the voltage detection limit is approximately independent of sample thickness and was ~ 0.2 V in all cases.

3.3.5 Mean Inner Ptential of Ceria

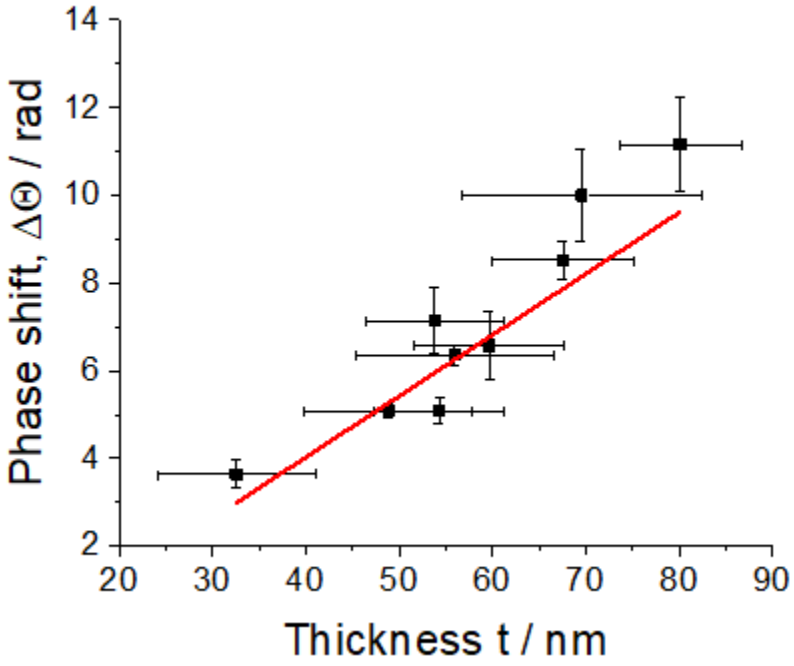

Figure 3.13 Phase contrast as a function of sample thickness at positions far removed from grain boundaries, used for determining the mean inner potential of ceria.

In the absence of other effects, the mean inner potential, V_{MIP}, generates a phase shift, $\Delta\theta$, given by $\Delta\theta = V_{MIP} C_E t$, where C_E is a constant equal to $0.00728\ rad/(V \cdot nm)$ for 200 keV electrons, and t is the sample thickness. Using the best fit slope to the measured data, a value of 19 ± 3 V was obtained for V_{MIP}. The non-zero intercept for $\Delta\theta(t)$ has been attributed in the literature to surface effects. A fit in which the intercept is forced to zero yields a of 15 ± 3 V, and lies within two standard deviations of the value obtained for a free intercept value. The work here

focuses on the difference between bulk and grain boundary regions of the samples studied. Because such surface effects would be expected to remain approximately constant across the sample, they play no role in establishing the grain boundary space charge potential or its detection.

For comparison to the experimentally determined value, the mean inner potential of ceria was calculated from the electron scattering factors of the elements using the expression[70]

$$V_{MIP} = \frac{h^2}{2\pi m_e e}\frac{1}{\Omega}\sum_j n_j f_j(0) = \frac{47.86}{\Omega}\sum_j n_j f_j(0) \qquad (3.6)$$

Here $f_j(0)$ is the electron scattering factor of element *j*, *h* is Planck's constant, *e* is the elementary charge, m_e is the rest mass of the electron, Ω is the unit cell volume in Å^3, and n_j is the number of atoms of element *j* that are in the unit cell. The electron scattering factors of Ce^{4+}, Sm^{3+} and O^{2-} are shown below[71]. For completeness, the 0.2 at% Sm doping is included in the calculation, but it has negligible impact on the result. The predicted mean inner potential is 17 V for 0.2% Sm doped ceria. This number is in good agreement with the measured value of 19 ± 3V.

Element	**Atomic number Z**	**electron scattering factors f_j(0), Å**
Ce^{4+}	58	6.1598±0.0005
Sm^{3+}	62	6.3881±0.0005
O^{2-}	8	4.0992±0.0009

Table 3.1 Electron scattering factors for elements of Ce^{4+}, Sm^{3+} and O^{2-}.

3.3.6 Barrierless Grain Boundary

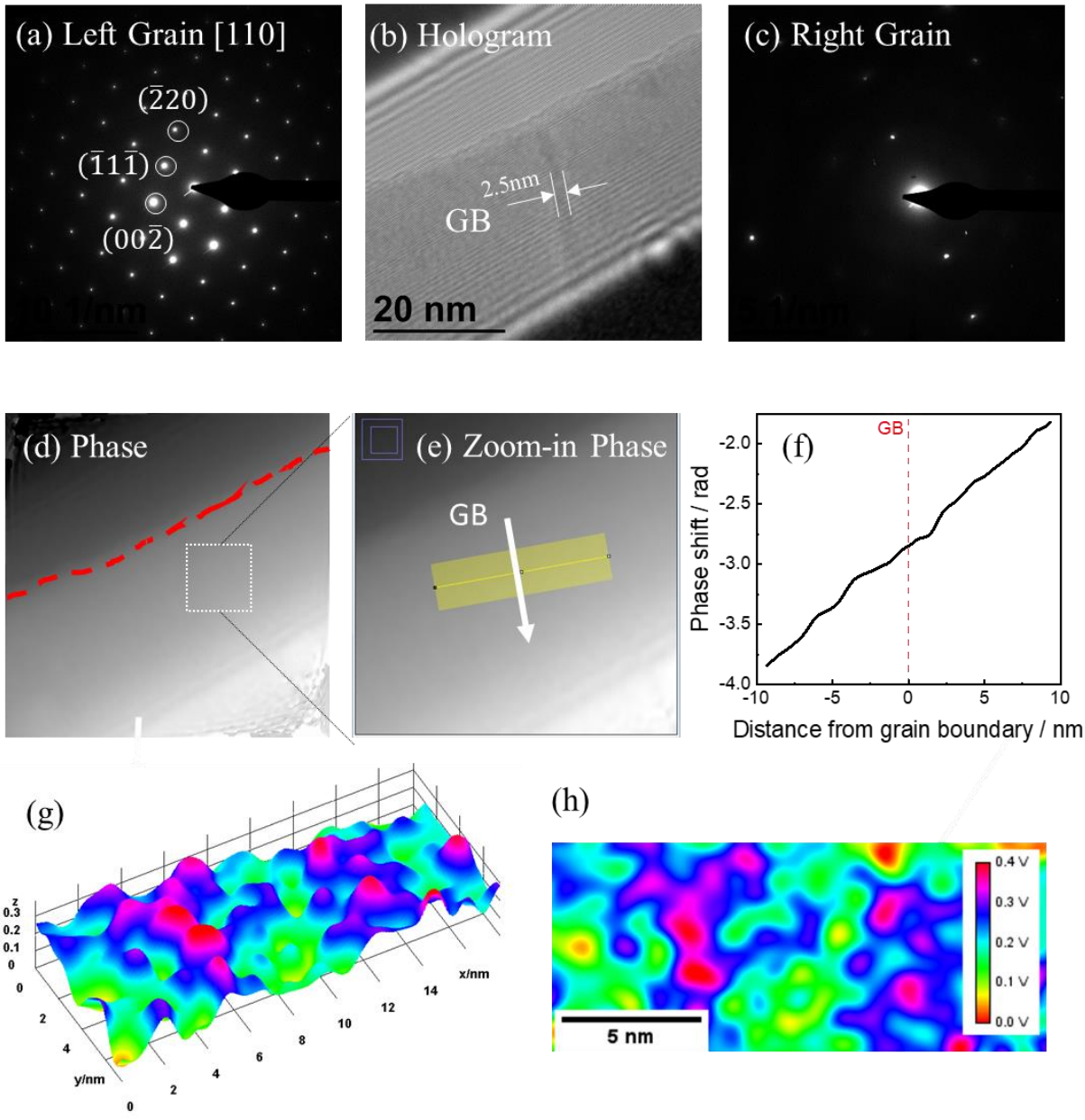

Figure 3.14 Transmission electron microscopy and electron holography imaging of a grain boundary in 0.2 at% Sm doped ceria with no apparent space charge potential , with the panels showing the features indicated.

Clear presence of the grain boundary is revealed in the hologram in Figure 3.14 (b), while the selected area diffraction patterns (a,c) show the regions on either side of the boundary are out of crystallographic alignment. The reconstructed phase maps (d,e) are almost featureless, and there is no impact of the grain boundary on the phase shift profile (f). The reconstructed electric potential map, shown in both (g) 3-D and (h) contour rendering, is similarly rather featureless. The contrast for this measurement is 25% and the sample thickness is 102 nm, thus the potential detection limit is 0.17 V. The absence of a detectable electric field in the vicinity of the grain boundary implies that the space charge potential must be less than 0.17 V.

3.4 Grain Boundary Segregation Unveiled by Atom Probe Tomography

3.4.1 Atom Probe Tomography Reconstruction

While grain boundary crystallography is clearly an important factor, understanding the origin of the grain boundary properties requires knowledge of the grain boundary chemistry to a sensitivity level greater than can be achieved by EDS. Atom probe tomography has elemental sensitivity to the ppm level as well as atomic level spatial resolution.[72] Samples for APT analysis (in the shape of sharp needles with diameter ~ 50 nm) were extracted from close to the surface and deep in the interior of the polycrystalline compact, accessed by cleaving in Figure 3.15.

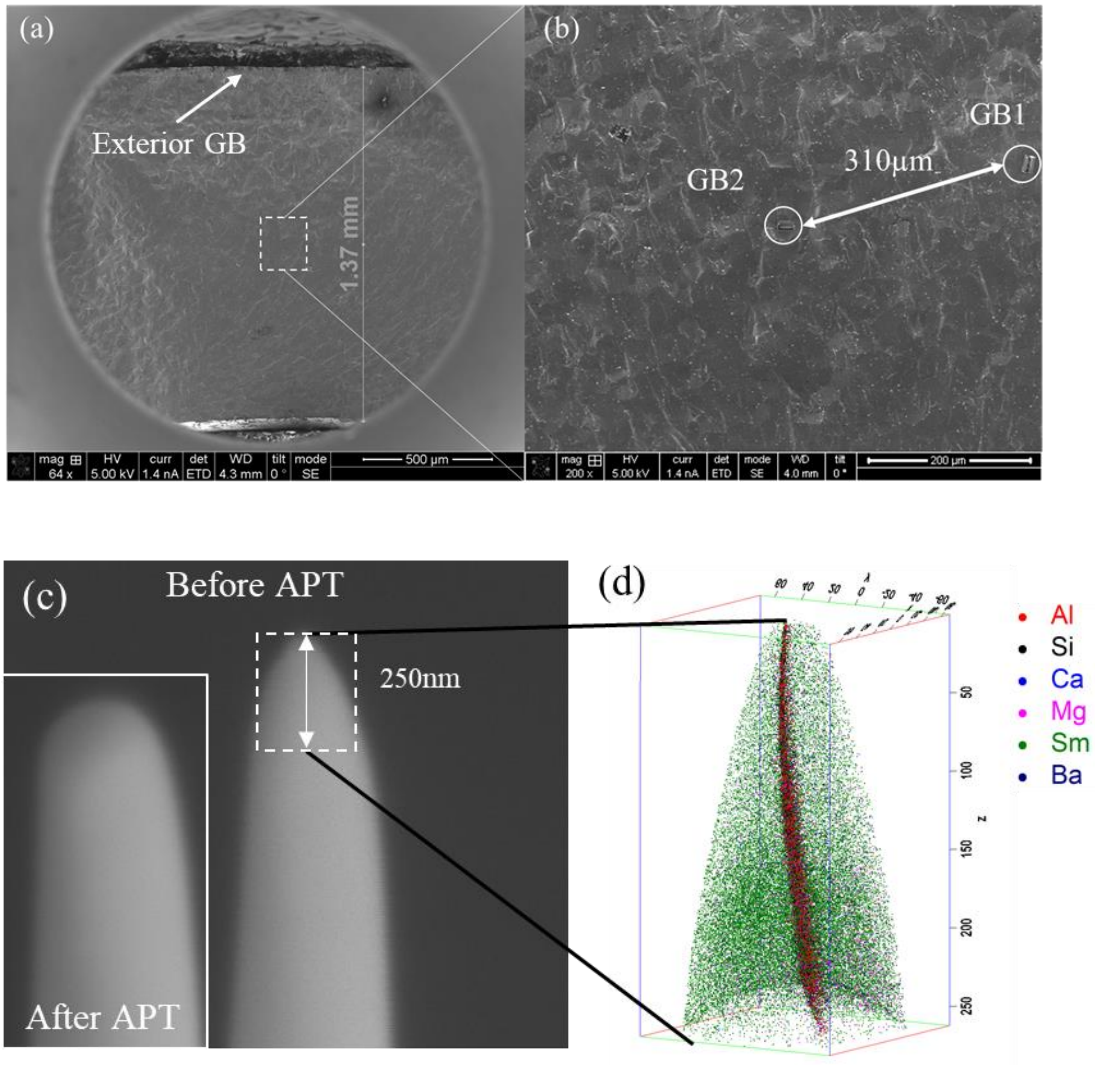

Figure 3.15 Scanning electron microscopy images showing the positions from which APT samples were extracted and the interior GB1 measured by atom probe tomography : (a) wide view cross-sectional image highlighting position from which the near-surface sample was extracted; and (b) zoomed view highlighting positions from which two bulk samples were extracted; (c) SEM image of representative tip-shaped sample before and after APT analysis; (d) APT reconstruction of atomic species.

Conversion from the APT reconstruction to the 1-D profiles was carried out as described below for the interior grain boundaries as an example. Integration was carried out over an area ~ 80 nm in diameter, as shown in the green region due to its lower background compared to other regions in Figure 3.16. Because the grain boundary is not flat in a rectilinear coordinate system, the proximity histogram ("proxigram") approach was employed in which the grain boundary position is automatically detected based on the elemental concentrations.[73] Here the Al iso-concentration surface with 0.035 atom % Al was selected to define the grain boundary. The bin size was 0.5 nm, with 3 nm voxel size and 6 nm delocalization. This parameter set gave isosurfaces most similar in shape to the GB plane. We note that analysis of subsections of the regions depicted here (results not shown) generated different relative concentrations of the impurity elements, indicating that even on the ~ 30 nm scale, significant heterogeneities are present. We further note that the peak concentrations in these other analyses were not always exactly centered on zero (with deviations of ~ 0.2 nm), reflecting the limits of the proxigram approach in handling a curved grain boundary in combination with varying concentrations along the boundary.

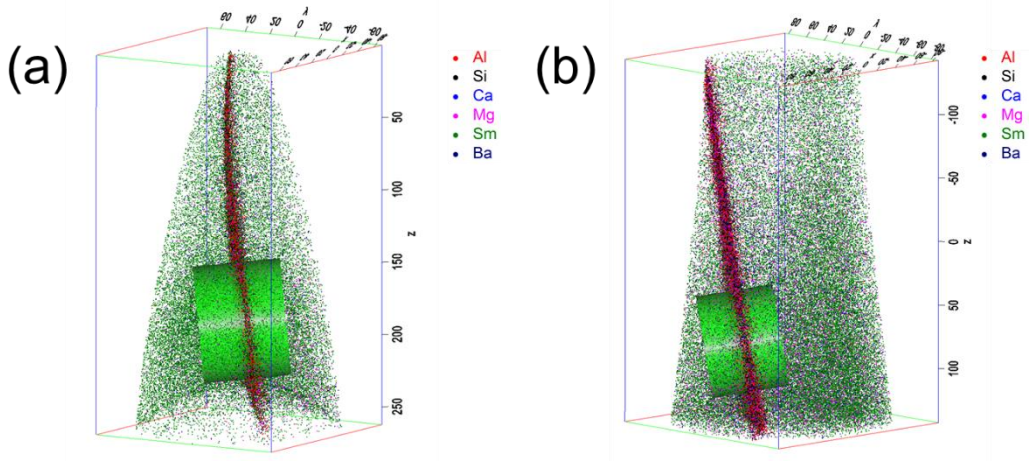

Figure 3.16 Conversion of APT reconstructions to 1-D concentration profiles : (a) GB1; and (b) GB2.

3.4.2 Exterior and Interior Grain Boundary

The representative grain boundary close to the sample surface was found to have high concentrations of Si, Al and Ca, as well as an enhanced Sm concentration relative to the bulk, Figure 3.17 (a). The two grain boundaries deep within the bulk show much lower, but non-negligible, impurity levels in addition to evidence of dopant segregation, Figure 3.17 (b,c). Averaged over the 10 nm expanse of the grain boundaries, the Al content is about twice that of the interior grain boundaries, whereas the Si is about four times higher. The Ca, Mg, Ba and Sm concentrations, in contrast, are comparable to those in the interior. This shows that the sample surface may be contaminated during high temperature sintering process. Therefore, only interior grain boundaries are typically selected for further analysis.

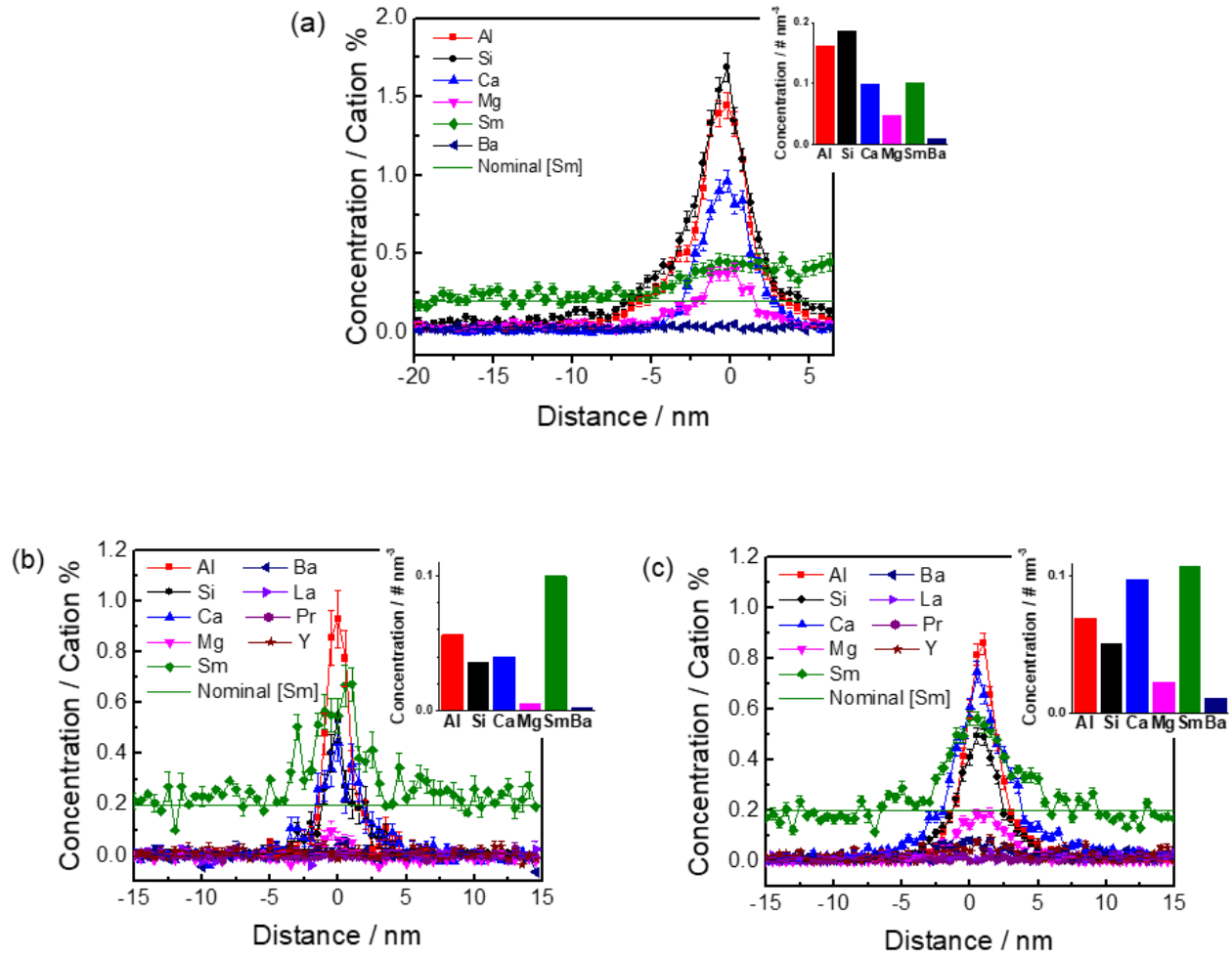

Figure 3.17 Atom probe tomography study of grain boundary located near the surface and in the bulk of the polycrystalline compact : (a) concentration profiles of exterior GB, with the grain boundary position assumed to coincide with the peak impurity concentrations, with inset plot of integrated mean volumetric concentrations from -5 to +5 nm. (b), (c) elemental distributions across interior GB1 and GB2, respectively;

Gaussian fits to the intensity profiles in interior grain boundaries yield the follow results in Table 3.1. The FWHM approximately corresponds to 2*d* used in holography analysis, and the results here motivated the use of d = 0.8 nm. Note that the Sm profile is significantly wider than that of the impurity elements, particularly in GB1.

	GB1		GB2	
Element	Peak / cation %	FWHM / nm	Peak / cation %	FWHM / nm
Al	0.87 ± 0.06	2.08 ± 0.09	0.78 ± 0.02	2.92 ± 0.05
Si	0.42 ± 0.03	2.41 ± 0.16	0.45 ± 0.01	3.86 ± 0.07
Ca	0.39 ± 0.03	3.31 ± 0.21	0.75 ± 0.03	4.99 ± 0.17
Mg	0.12 ± 0.01	1.78 ± 0.17	0.18 ± 0.01	4.33 ± 0.10
Sm	0.69 ± 0.06	4.52 ± 0.51	0.54 ± 0.03	5.76 ± 0.33
Ba	0.06 ± 0.01	1.34 ± 0.40	0.060 ± 0.005	4.69 ± 0.57

Table 3.2 FWHM of species Al, Si, Ca, Mg, Sm and Ba in GB1 and GB2.

Significantly, the impurity concentrations at these two grain boundaries differ substantially, despite their origin from a single sample and near proximity therein. In particular, while the dopant enhancement level (about 3× relative to the bulk) and the Al and Si concentrations of the two grain boundaries are similar, the Ca and Mg concentrations are notably lower in grain boundary 1 (GB1) than they are in GB2. It is known that introduction of alkaline earth elements into doped ceria increases its grain boundary conductivity,[74–77] and thus a difference in the concentration of these

elements between different boundaries immediately suggests differences in transport properties. Furthermore, although impurities were detected, the sample prepared here, with macroscopically averaged Si and Al concentrations of 18 ppm and 5ppm, respectively shown in Table 3.3, is far purer that any previously evaluated in the literature.[50]

3.4.3 Sample Impurity Level

The total impurity levels of the in-house ceria sample were estimated from the APT results and the measured grain size from SEM imaging. Taking each grain to be a cube ($L \times L \times L$), and the impurity-enriched grain boundary region to have a thickness of *l*, the total impurity level is expressed as

$$f_i = \frac{(6lL^2 c_i^{gb})/2 + c_i^{bulk} L^3}{L^3} = \frac{3lc_i^{gb}}{L} + c_i^{bulk} \qquad (3.7)$$

where c_i^{gb} and c_i^{bulk} are the concentrations of impurity *i* in the GB and bulk regions, respectively. The grain boundary concentrations used are those reported for GB1, in Figure 3.17(b), with an impurity-enriched region of 10 nm. The grain size is taken to be 12.5 μm on the basis of Figure 3.1. The background level measured in the APT experiment was 10 ppm/ns.

Element	Literature[50] / ppm*	This work		
		c_i^{gb} / ppm*	c_i^{bulk} / ppm*	Overall / ppm*
Si	867	1404	15	18
Al	<191	2217	-	5
Ca	155	1578	78	82
Mg	129	183	-	<1
Y	52	132	99	99
La	<186	27	27	27
Pr	<37	9	9	9
Gd	<164	-	-	-
Yb	<75	-	-	-
Dy	<32	-	-	-
Nd	<36	-	-	-
Er	<31	-	-	-

*ppm here is reported on a metal basis (i.e., relative to the number of cerium sites)

Table 3.3 Impurity concentrations in lightly doped ceria prepared here (0.2 at% Sm), as compared to the highest purity sample reported in the literature.

3.4.4 Electric Potential Profile

Several potential mechanisms by which dopant and alkaline earth metal segregation influence grain boundary conductivity have been proposed, but with no agreement to date. Here we consider the possible impact of the measured cation chemistry on interfacial charge. An estimation of the charge density was made under the following assumptions: (1) there is no distinct, grain boundary core; (2) the cations, including Ce, exist in their fully ionized state (Ce^{4+}, Si^{4+}, Al^{3+}, etc.); (3) smaller cations, Si^{4+}, Al^{3+}, reside in interstitial sites, whereas larger cations, Ca^{2+}, Mg^{2+}, Ba^{2+} and Sm^{3+}, reside on regular cation (Ce^{4+}) sites; and (4) the concentration of oxygen vacancies is small such that it does not impact the value of the electric field in the grain boundary region. This approach avoids reliance on the highly uncertain oxygen signal recorded by APT. With these assumptions, we (i) compute an initial charge density associated with the effective charge of the cation species (for example, Gd^{3+} replacing Ce^{4+} has an effective charge of -1, written Gd'_{Ce} in Kroger-Vink notation), (ii) compute the implied potential resulting from the excess positive charge, (iii) compute the oxygen vacancy profile under the assumption that the vacancies achieve electrochemical equilibrium, and finally (iv) compute the revised charge density that now accounts for both the cation excess and the oxygen vacancy depletion in the grain boundary and confirm that the impact of vacancies on the electric potential profile is negligible.

Here, GB1 is taken as an example with completed details. The charge, electric potential and oxygen vacancy profiles across grain boundaries were estimated as follows. First, for ease of analysis, the concentration profiles of Figure 3.18 (a) were represented by Gaussian profiles. Second, based on the ionic radii of the elements,[78] the likely site occupancies were assigned. Specifically, Al and Si were taken to reside in interstitial sites, whereas all other elements (see

legend of (a)), being comparable or larger than Ce^{4+}, were taken to enter the structure substitutionally. Third, the relative charges were assigned assuming the structural incorporation and the predominant ionic oxidation states. This implies the following species, as indicated in Kroger-Vink notation: $Al_i^{\cdot\cdot\cdot}$, $Si_i^{\cdot\cdot\cdot\cdot}$, Ca''_{Ce}, Mg''_{Ce}, Ba''_{Ce}, and Sm'_{Ce}. Fourth, the charge profile due to these segregated species, $\rho_{segregation}$, was computed by simple addition of the valence weighted profiles, specifically according to

$$\rho(x)_{segregation} = (3c_{Al} + 4c_{Si} - 2c_{Ca} - 2c_{Mg} - 2c_{Ba} - c_{Sm})e \qquad (3.8)$$

where c_i is the Gaussian profile concentration of each species, and e is the elementary charge, as shown in (b).

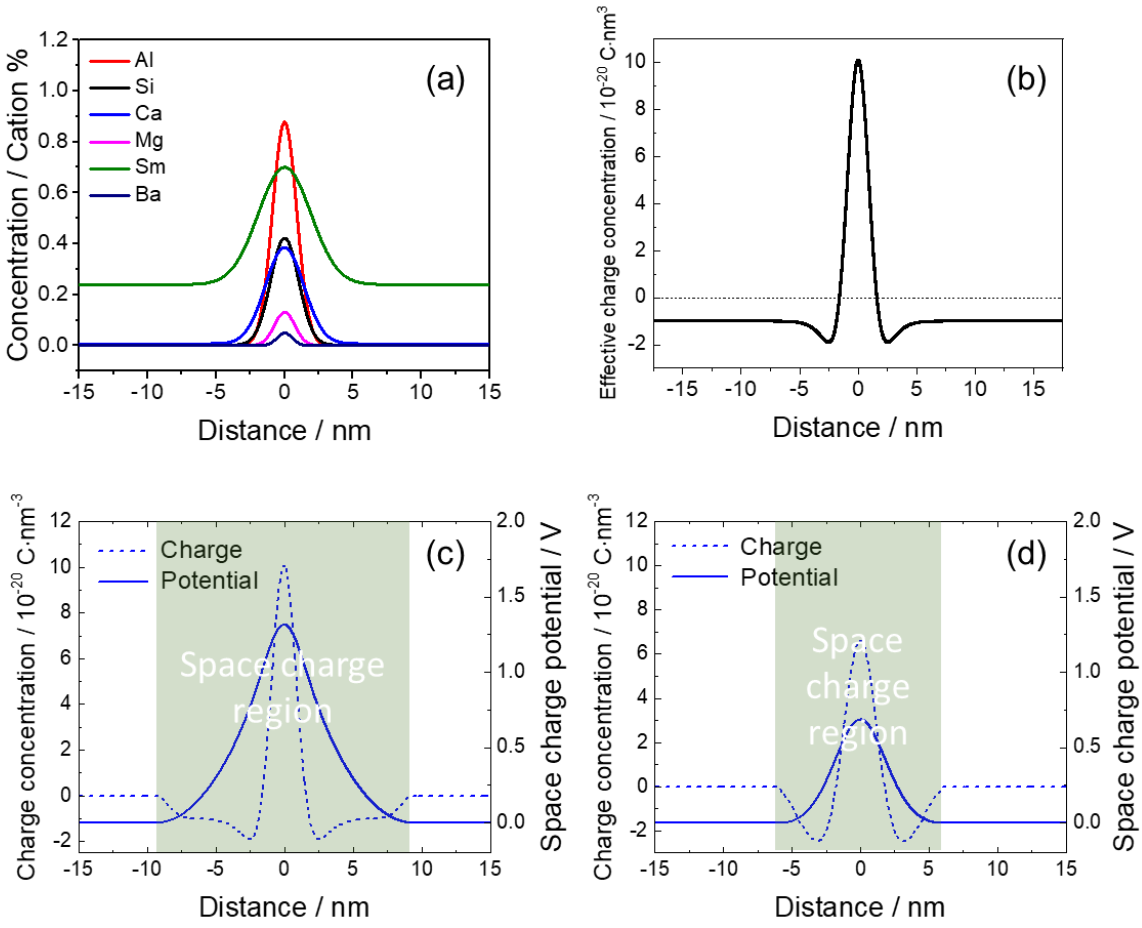

Figure 3.18 Inferring charge, electric potential, and oxygen vacancy profiles from elemental concentration profiles determined by atom probe tomography : (a) Gaussian fits to the profiles shown in Figure 3.17 (b) for GB1; (b) intermediate calculation of charge density due to cation segregation; and (c,d) overlain charge and potential profiles for GB1 and GB2, respectively, after accounting of anion vacancies.

This fourth step produces charge profiles that are not balanced by the presence of oxygen vacancies. Far from the grain boundary, the effective positive charge due to oxygen vacancies

balances out the negative offset evident in the figure, where the latter arises from the Sm dopant species. In the grain boundary region, the large positive charge presumably repels oxygen vacancies, but the system has no way of generating negative charge to balance out the impurities. That is to say, even with an oxygen vacancy concentration of zero, ignoring dopant segregation, introduction of Si^{4+} and Al^{3+} into interstitial sites of ceria cannot be locally charge balanced (unless oxygen interstitials are invoked, a possibility considered unlikely and hence not treated here). Thus, in the fifth step, the electric field due to $\rho_{segregation}$ was computed, where we make the reasonable assumption that the oxygen vacancy concentration can be omitted for the first round analysis. That is, the field was computed according to Poisson's equation

$$\nabla^2(\Delta\varphi) = -\frac{\rho}{\varepsilon} \tag{3.9}$$

with the charge density set to $\rho_{segregation}$ and the bulk dielectric constant set to the value measured by impedance spectroscopy (ε_r = 36), and according to the boundary conditions

$$\begin{aligned} &\Delta\varphi(0) = \Delta\varphi_0 \qquad && \Delta\varphi(\infty) = 0 \\ &\left.\frac{\partial\Delta\varphi}{\partial x}\right|_{x=0} = 0 \qquad && \left.\frac{\partial\Delta\varphi}{\partial x}\right|_{x=\infty} = 0 \end{aligned} \tag{3.10}$$

In the final step, the oxygen vacancy concentration, $C_{V_O^{\cdot\cdot}}$, was computed using the electric potential profile and the assumption of electrochemical equilibrium. Specifically, we used the expression

$$C_{V_O^{\cdot\cdot}}(x) = C_{V_O^{\cdot\cdot}}(\infty)\exp\left(-\frac{2e\Delta\varphi(x)}{kT}\right) \tag{3.11}$$

where $C_{V_O^{\cdot\cdot}}(\infty)$ is the vacancy concentration in the bulk, fixed by the dopant concentration. The charge due to oxygen vacancies was added to the $\rho_{segregation}$ to generate the final charge concentration profiles shown in (c) and (d). Here we see positively charged cores flanked by negatively charge regions, and the overall features are reminiscent of traditional space charge profiles. The positive core is due to the Si^{4+} and Al^{3+} impurities, which cannot be charged balanced within the framework of the fluorite structure. The adjacent negative regions are due to the repulsion of oxygen vacancies by the core, and to some extent, due to the enhancement of dopant species with effective negative charge, which are presumably attracted by the positively charged impurities.

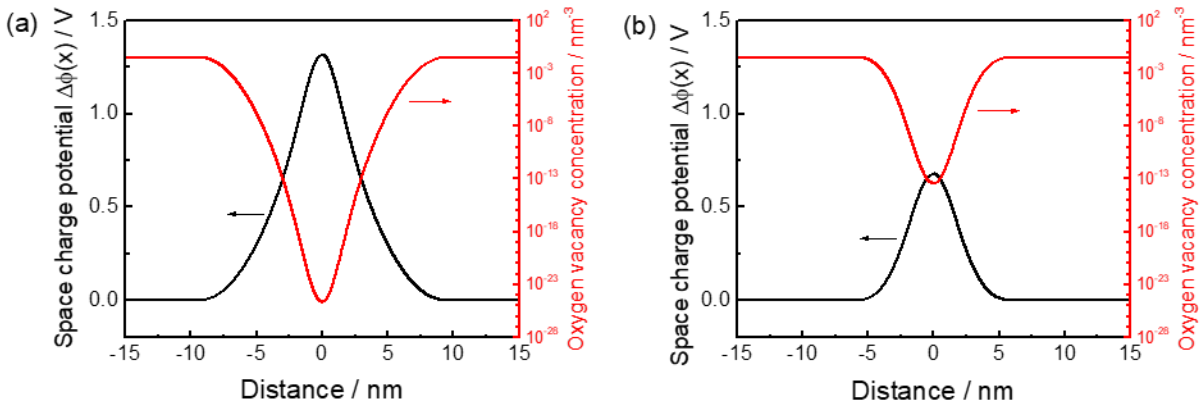

Figure 3.19 Inferred potential and oxygen vacancy concentration profiles for (a) GB1, and (b) GB2, respectively.

The electric potential and vacancy profiles derived from such an analysis are presented in Figure 3.19. Significantly, the assumptions regarding the effective charges of impurity and

segregated dopant species produce an electric field profile and accompanying vacancy depletion profile that are essentially indistinguishable from that produced by the assumption of a charged, infinitely thin grain boundary core. The inferred space charge potentials at the interface are 1.3 and 0.7 V, respectively, for GB1 and GB2, with vacancy depletions at the interfaces of ~20 and ~10 orders of magnitude (as is standard for space charge effects). The almost two-fold difference between the two $\Delta\varphi_0$ values support the conclusion from the holography measurements that substantial grain-to-grain variations are possible in a single material. The present analysis implies that positive charge at the grain boundary core originates from the presence of Si and Al impurities, as opposed to an inherent imbalance between native cationic and anionic species, and that segregation of species with effective negative charge, Gd'_{Ce}, Ca''_{Ce} , etc., to the grain boundary decreases the space charge potential. Thus, the scavenging role of alkaline earth dopants in enhancing grain boundary conductivity can be very simply understood as countering the impurity charge. Similarly, dopant segregation naturally diminishes, rather than increases the grain boundary resistance. We suggest that heightened dopant segregation explains the steep decline of grain boundary resistance with increasing dopant concentration, as reported for Gd-doped[2,55,56], Y-doped[50,56] and La-doped[56] ceria. The interpretation suggests that alkali metals, which have rarely been studied as additives to ceria, may serve as particularly effective space charge scavengers.

3.5 Summary

We directly observe high positive charge in the grain boundaries of lightly doped, high-purity ceria. The detected space charge potential varies from as much as 1.15 V to negligible. This wide range puts into question models of material behavior that assume a single value for $\Delta\varphi_o$. In the case of [110] tilt boundaries, the space charge potential apparently decreases with tilt angle, a result that may reflect the behavior of the surface energy. The observation of grain boundaries that are free of a detectable electric field perturbation indicates that charge imbalance at the interfaces of oxide electrolytes may not be an inherent material property. Indeed, Si and Al impurities at the grain boundaries, as detected by atom probe tomography, may be entirely responsible for high interfacial charge. A similar conclusion was reached in the case of $SrTiO_3$, in which an electric field perturbation at grain boundaries was found only in the presence of impurity species; pristine grain boundaries displayed negligible space charge potential.[60] Here, segregation of trivalent and divalent substitutional dopants to the grain boundaries apparently counters the charge of tetravalent interstitial impurities, and may be the reason for the substantially higher grain boundary conductivity in heavily doped fluorites than in those which are lightly doped, as studied here. The finite-core space charge model developed here provides an approximate framework for treating the electric potential profile generated by differentiated regions of impurity and segregated dopant charge.

4 Direct Grain Boundary Study in Ceria Fibers

4.1 Abstract

Many previous works have focused on mixed ionic-electronic conductors to study material behavior based on single values of grain boundary properties such as space charge potential, grain boundary conductivity, activation energy, etc. even though millions of grain boundary exist in the sample. This is due to a lack of appropriate methods and techniques access to single grain boundary properties. The aim of this work is the deconvolution of the contributions of individual grain boundaries to the macroscopically averaged contribution of an ensemble of grain boundaries on the transport properties of polycrystalline mixed ionic-electronic conductors. We directly observe up to 3 orders of variation in single grain boundary conductivity for samples in the same batch of ceria fibers by impedance spectroscopy. The implied space charge potential varies from 0.25 V to 0.41 V. Due to the small distance between electrodes, we are able to apply large electric field to single grain boundaries and observe current saturation when bias across grain boundaries reaches 1.5×10^{3} V/cm at 450 °C. Such behavior has been theoretically predicted but never previously observed. Electron backscatter diffraction and secondary ion beam spectroscopy unveil the unique misorientation of each fiber, and various segregation level of Si, Al, Ca and Mg at grain boundaries. Variable enrichment of these species may be responsible for the large variation of grain boundary transport properties.

4.2 Ceria Fibers and Fiberboard

4.2.1 Ceria Fibers

As previously reported, the undoped ceria fibers provided by Zircar Zirconia Inc. have diameter in the 3 – 10 um range, and we typically select those with a diameter of about 6 μm for electrical measurement. The grain boundaries lie normal to the axial direction and are spaced every 10-40 μm along the length of the fiber as shown in Figure 4.1. As evident from the representative high resolution transmission electron microscopy image of a thin slice of sample prepared by focused ion beam (FIB) milling, the grain boundaries are sharp and free of any amorphous phase.

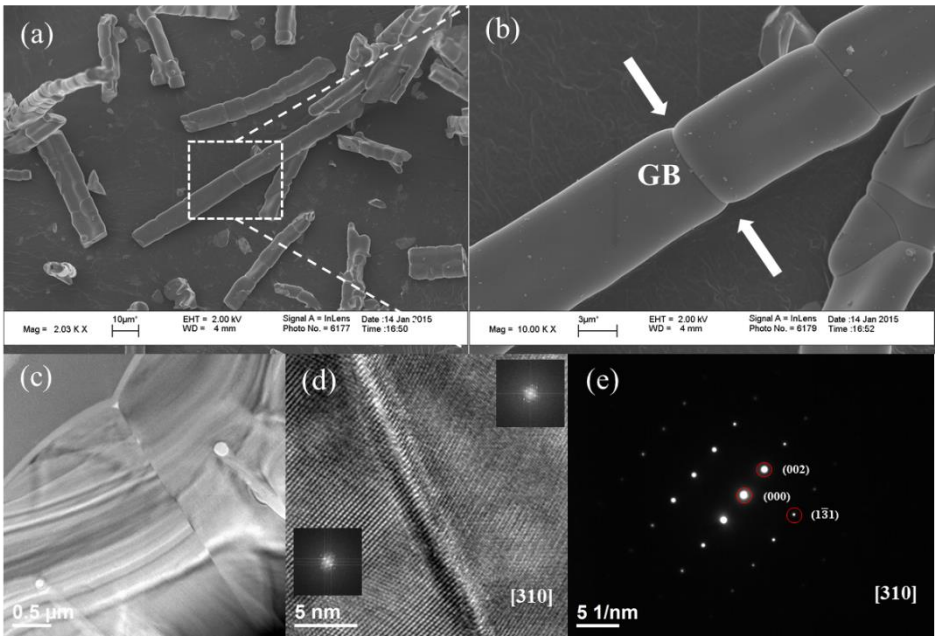

Figure 4.1 Electron image of a representative fiber and grain boundary : (a) scanning electron microscopy image of a representative fiber, (b) zoomed in view of (a) showing the clear grain boundary; (c) low mag transmission electron image of the grain boundary, with (d) high resolution transmission electron image; (e) selected area diffraction pattern of the left grain showing the grain boundary is in the [310] zone axis.

4.2.2 Ceria Fiberboard

The sintered fiberboard prepared by conventional ceramics processing starting from the same batch of fibers shows high density, >96% of the theoretical value as measured by the Archimedes method. The grain size is determined to be 10.9 ± 0.7 μm from the scanning electron microscope image as shown in Figure 4.2 by using mean-intercept method.

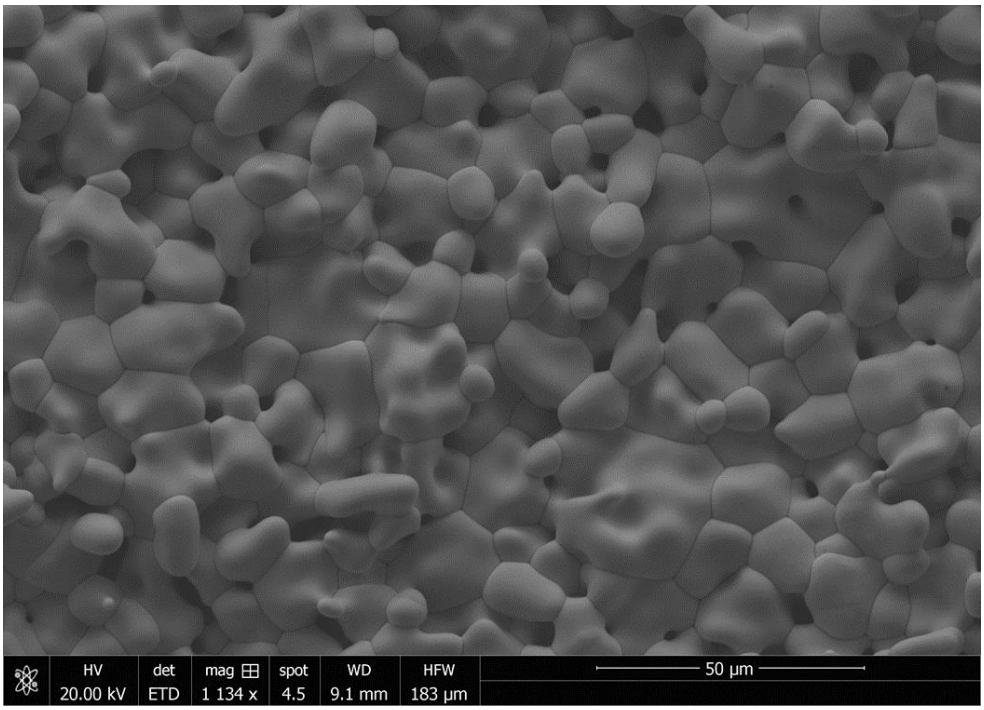

Figure 4.2 Scanning electron microscopy image of the fiberboard prepared by sintering commercial ceria fibers at 1550 °C for 28 hours with relative density >96%.

Example electrical impedance spectra are showed in Figure 4.3 revealing the bulk and grain boundary impedance in air from 500 °C to 300 °C. As seen in Chapter 3.2.3, the impedance data were analyzed by equivalent circuit fitting, yielding the bulk and grain boundary resistances and

their equivalent capacitances at each measurement temperature. The bulk conductivity was determined by accounting for the sample dimensions with the equation: $\sigma_{bulk} = \frac{1}{R_{bulk}}\left(\frac{L}{A}\right)$ where L and A are sample thickness and sample area, and R_{bulk} is bulk resistance. The specific grain boundary conductivity was calculated from the impedance fit parameters within the framework of the brick-layer model[54] using the expression $\sigma_{gb} = \frac{1}{R_{gb}}\left(\frac{L}{A}\right)\left(\frac{C_{bulk}}{C_{gb}}\right)$, where C_{bulk} and C_{gb} are the respective bulk and grain boundary capacitances and R_{gb} is the grain boundary resistance. A single, temperature-averaged capacitance ratio was employed for the calculation. This expression accounts for the fact that the total length of grain boundary material that contributes to the measured grain boundary resistance is only a small fraction of the sample length, where that fraction under the assumption of a spatially invariant dielectric constant is approximated by $\frac{C_{bulk}}{C_{gb}}$. Thus, the grain boundary thickness δ can be estimated according to $\frac{C_{bulk}}{C_{gb}} = \frac{\delta}{G}$ where G is grain size and δ was determined to be 29.9 nm. To be accurate, the calculated grain boundary thickness is not a physical or crystallographic thickness, but a thickness related to electrical proporties, describing the width of space charge layer.

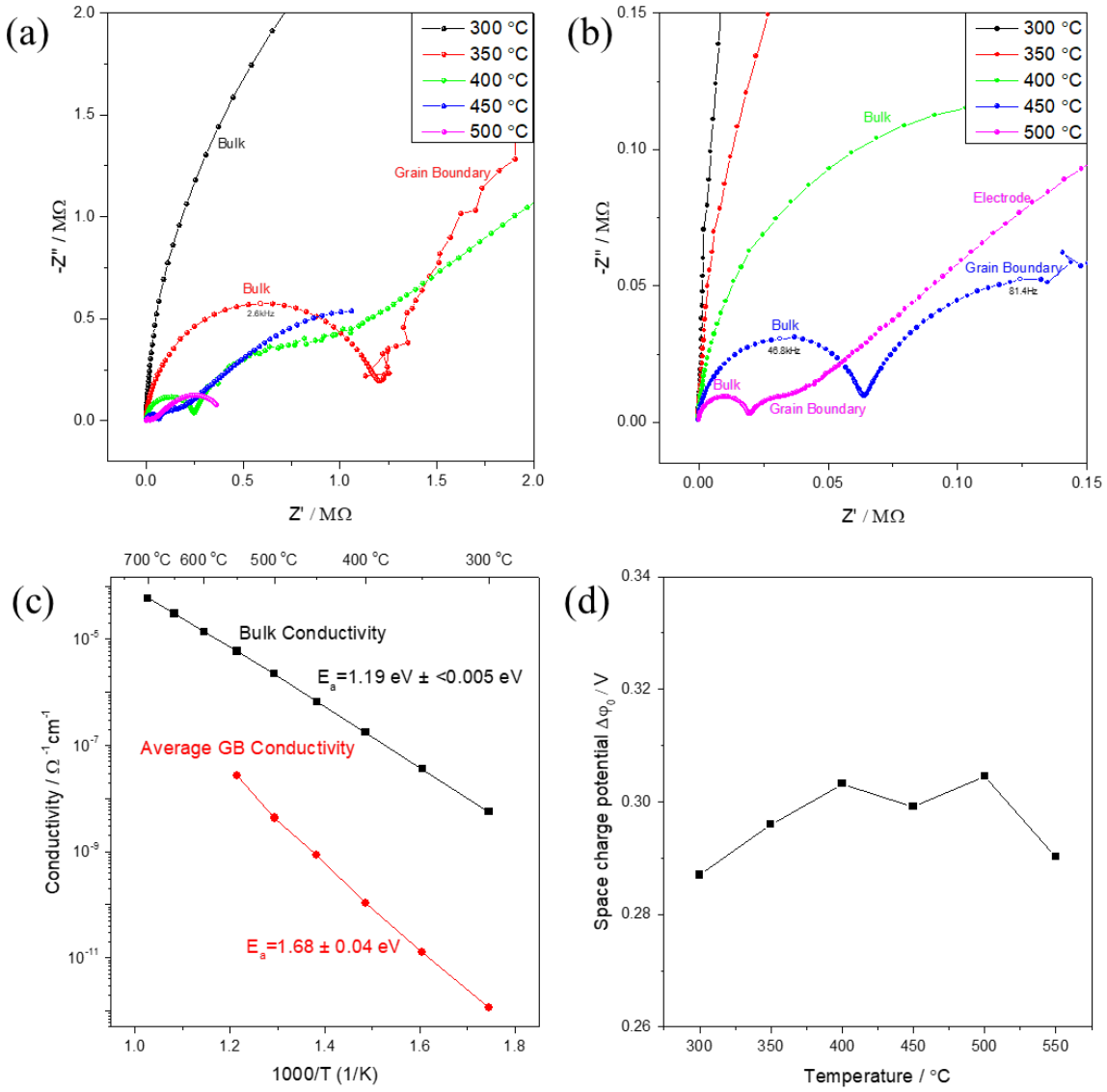

Figure 4.3 Macroscopic transport properties of ceria fiberboard (grain size 10.9 ± 0.7 μm) under synthetic air : (a) impedance spectra and (b) expanded spectra, collected at the temperatures indicated; (c) bulk and specific grain boundary conductivity determined from equivalent circuit fitting; and (d) space charge potential inferred from a Mott-Schottky analysis.

As shown in Figure 4.3 (c), the grain boundary conductivity is 3-4 orders of magnitude smaller than that of the bulk with an activation energy of 1.68 ± 0.04 eV higher than that of the bulk, 1.18 eV (statistical uncertainty < 0.005 eV). The higher grain boundary activation energy is consistent with our 0.2% Sm doped CeO_2 used for electron holographic study and is commonly reported elsewhere[50,51,79]. The space charge potential at each temperature was calculated according to Eq. (3.2) as shown in Figure 4.3 (d) with temperature averaged value 0.30 V.

4.3 Device Performance

4.3.1 COMSOL Simulation

The electrodes of the fabricated device for in-plane measurement are shown in Figure 4.4. The contact area between the electrodes and the tested fiber does not fully wrap the fiber. Only half of the area around the fiber is in contact with SCN20 coated Pt posts. To assess the impact of this geometry on the measured transport properties, finite element simulation was performed by using the AC/DC module of COMSOL 5.2. The geometry of a typical fiber was set to 6 μm in diameter and 20 μm in length. The bulk and grain boundary conductivity measured from the fiberboard at 450 °C in air were used for simulation. A voltage of 50 mV was applied. The maximum mesh size was 0.2 μm as the results among varied mesh size agreed within 1%. To compare, another electrode type was simulated with fully wrapped electrodes on a fiber.

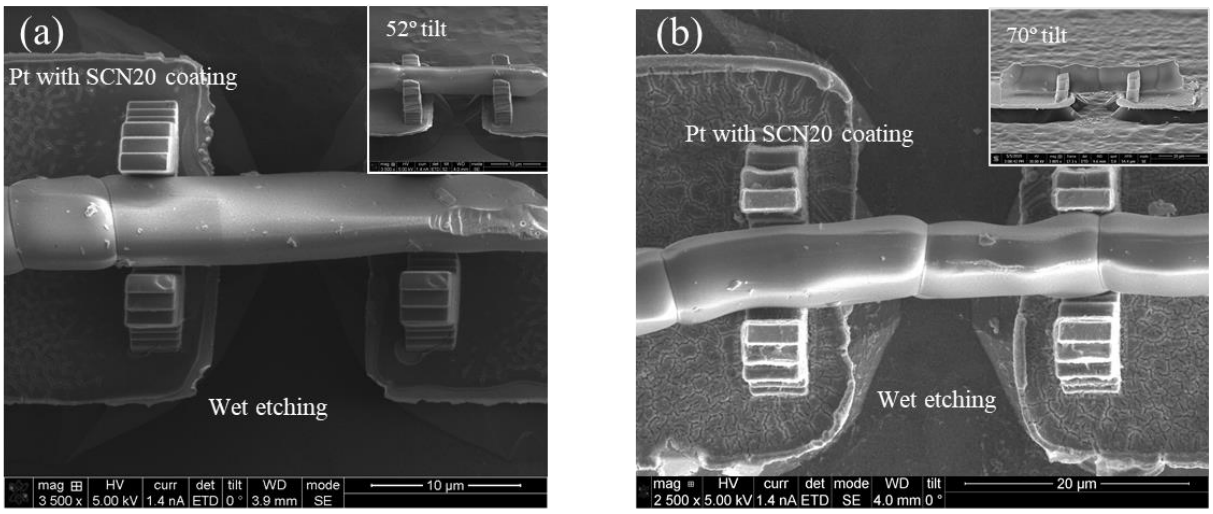

Figure 4.4 Scanning electron imaging of two representative samples : (a) a fiber without grain boundary, (b) a fiber with a single grain boundary.

At 450 °C, a typical fiber with 6 µm in diameter and 20 µm in length has a total resistance of 23 GΩ. On both sides of the fiber, electrodes with a width of 3 µm are half-wrapped as shown in Figure 4.5 (a, c). This decreases the effective fiber length. The simulated resistance is 20 GΩ which is 3 GΩ less than the fiber resistance. When the electrodes are hypothetically fully wrapped around the fiber, the resistance turns out to be 18 GΩ which is even less than the fiber resistance. The current density distribution in Figure 4.5 (e)-(g) quantifies this behavior: the electrodes have a finite width along the axis of the fiber which shortens the current pathway making the fiber "shorter" than actual length. Therefore, with conductivity and cross-sectional area unchanged, the resistance will be less than the real.

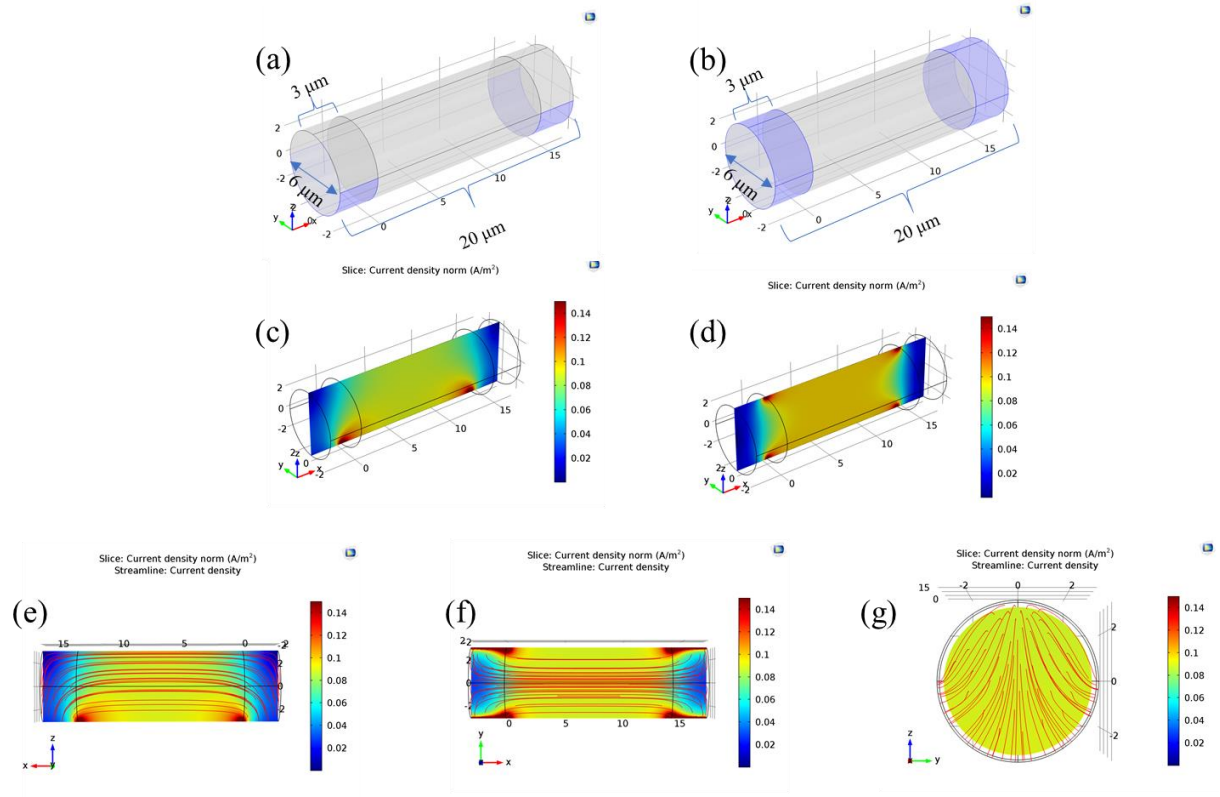

Figure 4.5 Electrical conductivity simulation in AC/DC Module COMSOL 5.2 : (a) half-wrapped electrodes, and (b) fully wrapped electrodes, with (c) current density of (a), and (d) current density

of (b); Streamline of current density in (e) x-z plane, (f) x-y plane, and (g) y-z plane of half-wrapped electrodes. Current density norm means the absolute magnitude of current density with the unit of A/m^2. Simulation conditions: temperature = 450 ° C, voltage=50 mV, atmosphere = air, fiber diameter = 6 μm, max mesh size for simulation = 0.2 μm.

By comparing the two different electrode types, the half-wrap electrodes are more resistant than the fully wrapped electrodes because the cross-sectional area that current travels through is slightly smaller, somewhat balancing the decreased resistance due to the shorter current pathway. Furthermore, the total resistance of 17 μm and 14 μm fibers are calculated to be 21 GΩ and 20 GΩ respectively. In terms of resistance, a 20 μm long fiber with half-wrapped electrodes is equal to a 14 μm long fiber. This means that the current density almost distributes over the entire cross-sectional area between the two electrodes which is also 14 μm. Even when compared to a 20 μm long fiber, the half-wrapped electrodes only bring down the total resistance by 13% as shown in Table 4.1.

For electrical measurement on fiber samples, it is extremely difficult to apply electrodes on both end faces of fibers which means the real resistance is hard to measure. Since the current distribution in the region between electrodes is almost fully distributed, the half-electrode provides a satisfactory measurement geometry.

Types	Total resistance / GΩ	Half-wrapped electrodes relative to other cases
Half-wrapped electrode	**20**	**-**
Full-wrapped electrode	18	111%
20μm long fiber	23	87%
17μm long fiber	21	95%
14μm long fiber	20	100%

Table 4.1 Simulated resistance at different electrode types and length of fibers.

4.3.2 Sample Holder and Bare Device Impedance

The sample holder is an alumina 4-bore tube (AdValue Technology, Inc) with three Pt wires through it. The holder was preheated to 1100 °C for 3 hours to remove surface contamination. Ceramics bond (Aremco Products, Inc) was used to seal the end of the holder. This is because ceramics bond as a high temperature sealant has a much higher impedance than any conventional polymer sealants. The impedance spectra of the sample holder without loading samples from 500 °C to 300 °C under flowing air are shown in Figure 4.6 (a). The sample holder is shown to be very resistive at high temperature, e.g. >1800 GΩ at 450 °C.

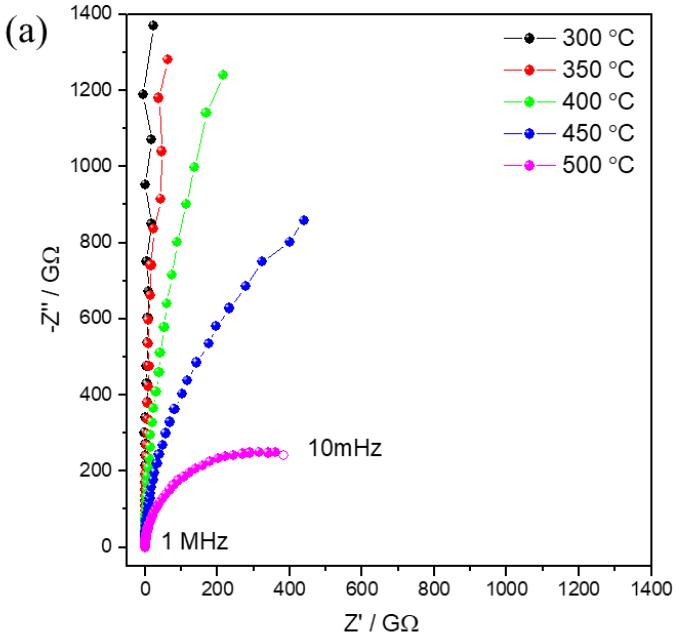
(a)
300 °C
350 °C
400 °C
450 °C
500 °C
10mHz
1 MHz
-Z'' / GΩ
Z' / GΩ
0
200
400
600
800
1000
1200
1400

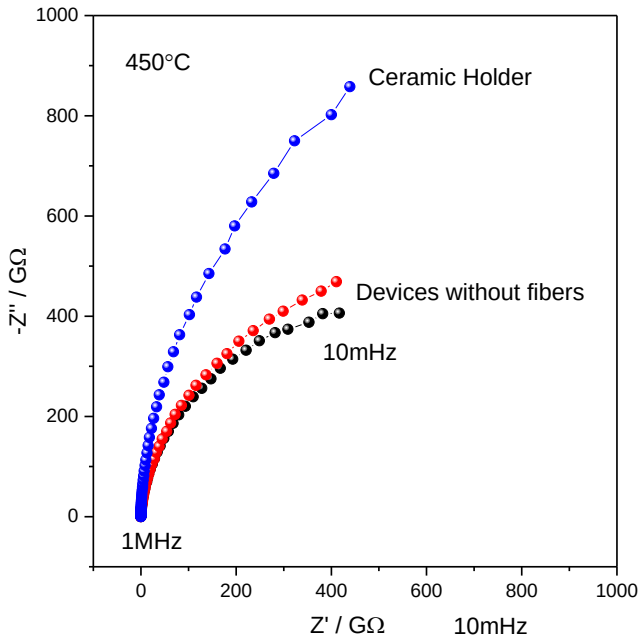
450°C
Ceramic Holder
Devices without fibers
10mHz
1MHz
10mHz
-Z'' / GΩ
Z' / GΩ
0
200
400
600
800
1000

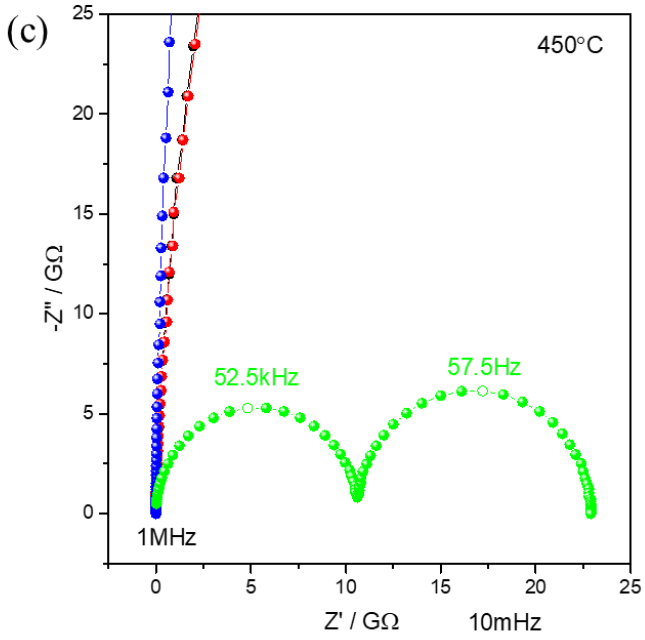

Figure 4.6 Macroscopic transport properties of the sample holder and devices without loading fibers under synthetic air : (a) impedance spectra of sample holder from 500 °C to 300 °C; (b) impedance spectra of sample holder, devices without fibers collected at 450 °C, and (c) spectra from (b) along with the simulated impedance of a typical fiber (6 μm thick and 20 μm long).

Two bare devices without fibers were also tested on the same conditions. In Figure 4.6 (b-c), impedance of sample holder and two bare devices are compared at 450 °C. Even though the impedance of the two bare devices is lower than that of sample holder, they still have a >800 GΩ impedance. The impedance spectrum of a fiber which is 20 μm long and 6 μm thick is simulated based on the bulk conductivity and grain boundary conductivity from the fiberboard. Since the grain boundary conductivity from the fiberboard is the averaged conductivity of all grain

boundaries, the fiber impedance can be only for reference. As reported previously, the total fiber resistance (including both bulk and grain boundary resistance) is 23 GΩ which is much smaller than that of bare device, which is over 800 GΩ. Therefore, the leakage contribution from the substrate is negligible and, therefore, ignored.

4.3.3 Reducing Electrode Impedance by SCN20 Coating

An essential aspect of the fabricated devices is the SCN20 coating, which can reduce electrode impedance due to its high catalytic activity. To validate the coating effect, two devices, each of which carried a fiber free of grain boundaries, were measured at the same conditions by impedance spectroscopy. The fiber loaded into the device without the SCN20 coating was 8 μm in diameter and 16 μm in length with the bulk resistance estimated to be 5 GΩ at 450 °C based on the bulk conductivity from the fiberboard. Similarly, the other fiber in the device with the SCN20 coating was 5 μm in diameter and 15 μm in length with the bulk resistance estimated to be 13 GΩ at 450 °C. Example impedance spectra at 450 °C in air are shown in Figure 4.7. Under zero bias, the measured impedance of the fiber in the device without the SCN20 coating is 40 GΩ which is much larger than the estimated value 5 GΩ. In contrast, the impedance of the fiber in the device with the SCN20 coating was measured to be 11 GΩ which is consistent with the estimated 13 GΩ. This implies that the Pt electrode introduces large resistance to the impedance measurement.

Furthermore, bias was applied to the measurement from 0 V to 1 V and went back to initial state of zero bias as the last step. The impedance of the device without the SCN20 coating is sensitive to the applied bias, and decreased from 40 GΩ to 5 GΩ when bias changed from 0 V to 1 V. Since the tested fiber is free of grain boundaries and the bulk electrical conductivity is

independent of bias, the change in impedance must be from electrochemical response from the electrode. This shows that the main impedance is due to the electrode response, which results from inadequate electrochemical activity at the Pt-ceria-gas interface. In such a device, any grain boundary impedance would be buried and overwhelmed by the electrode response.

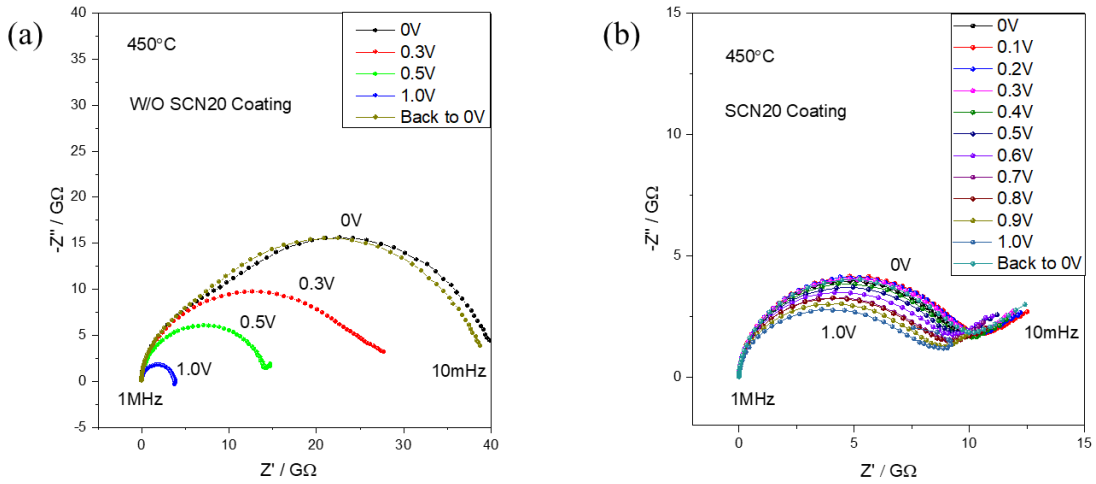

Figure 4.7 Bias behavior of devices with and without SCN20 coating under synthetic air : (a) impedance spectra of a device without SCN20 coating at the bias from 0 V to 1 V; (b) impedance spectra of a device with SCN20 coating at the same bias range.

However, the impedance behavior of bare device with the SCN20 coating is relatively unchanged under bias from 0 V to 1 V, which implies the electrode impedance is small. This simply reflects the high electrochemical activity of SCN20. It is anticipated that by using the coated device, the grain boundary impedance in a boundary containing fiber can be unveiled without influence of the electrode impedance.

4.4 Grain Boundary Impedance

4.4.1 Impedance Spectra of Single Grain Boundaries

Impedance spectra of an example ceria fiber with a grain boundary (a bicrystal) are shown in the Nyquist plot in Figure 4.8 from 500 °C to 300 °C. Through the entire frequency range of 1 MHz to 10 mHz, each impedance spectrum is a single depressed semicircle with the resistance spanning from 5 GΩ to over 1000 GΩ. The observed impedance spectra are inconsistent with those commonly observed on macroscopic polycrystalline samples in Figure 2.8, which have well separated bulk and grain boundary arcs in the frequency domain. After an intensive study of the spectra and the impedance measurement system, we found that a large stray capacitance affiliated with the device, sample holder and wiring was responsible for the observation of a single arc in the impedance spectra of a bicrystal fiber.

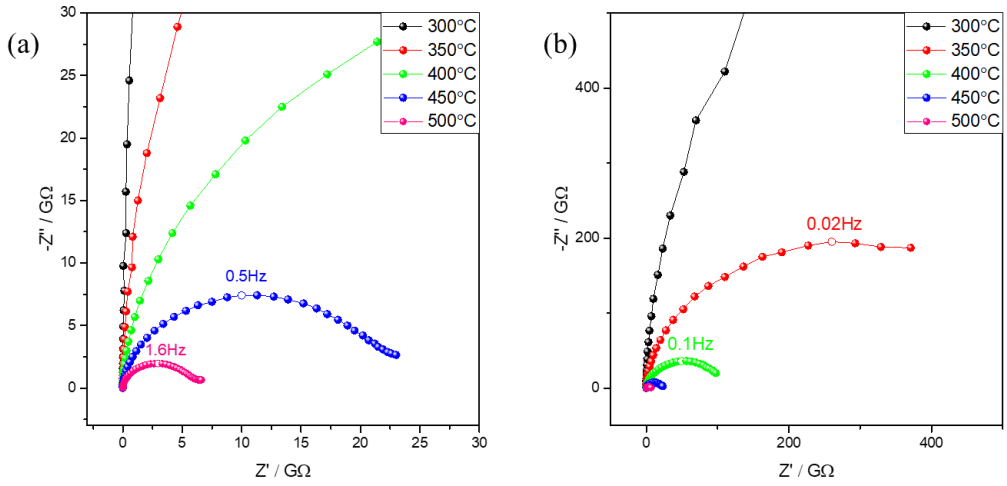

Figure 4.8 Macroscopic transport properties of a single fiber under synthetic air : (a) impedance spectra and (b) expanded spectra, collected at the temperatures indicated.

4.4.2 Stray Capacitance Effect

Stray capacitance, or parasitic capacitance, is an unavoidable capacitance that generally exists between electronic elements within a circuit. When electronic elements have different electrical potentials and are close to each other, electric charge will be stored on them and additional capacitance, which is stray capacitance, will be introduced to the circuit. Generally, the stray capacitance effect is observed when a small capacitance is being measured.

Unlike through-plane measurement which may have a quite large distance between electrodes reducing stray capacitance, the in-plane measurement generally has smaller distance between electrodes. In this study, the Pt posts are less than 20 μm between each other which implies unavoidable stray capacitance. Building on the results shown in Figure 4.6, the temperature dependence of the impedance of two devices without fibers were measured with the impedance spectra as shown in Figure 4.9. The capacitance values determined from both the ceramic holder in Figure 4.6 (a) and from the two devices in Figure 4.9 are reported in Table 4.2. The average capacitance of the sample holder and the devices over the temperatures are almost the same. This shows that the sample holder we used for impedance measurement has already introduced very high stray capacitance to the measurement, which means that no matter how device fabrication is improved, stray capacitance cannot be lower than $1.2\times10^{-11}F$.

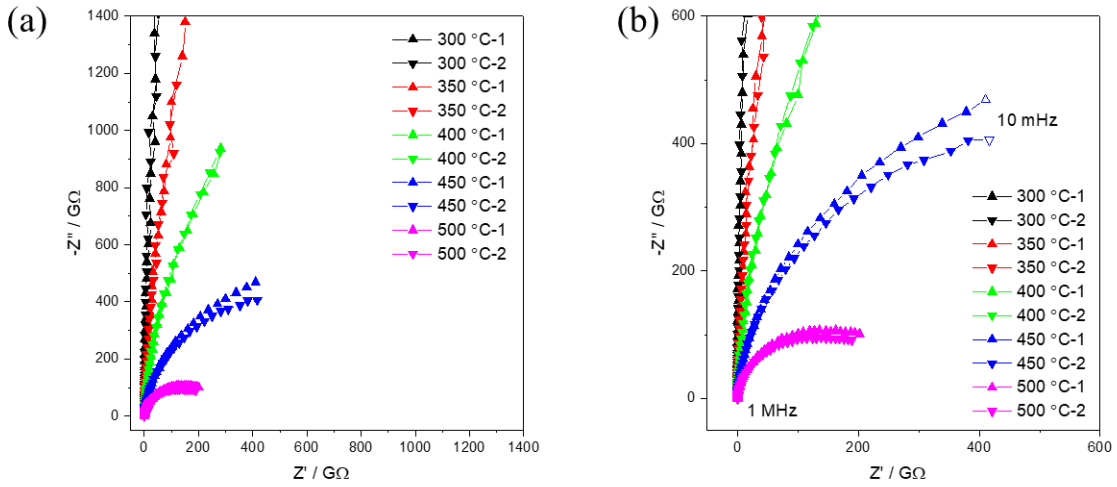

Figure 4.9 Macroscopic transport properties of two devices without loading fibers under synthetic air : (a) impedance spectra and (b) expanded spectra, collected at the temperatures indicated.

Temp / °C	Capacitance of the sample holder / F	Capacitance of the Device #1 / F	Capacitance of the Device #2 / F
300	1.2×10^{-11}	9.0×10^{-12}	1.0×10^{-11}
350	1.2×10^{-11}	1.3×10^{-11}	1.1×10^{-11}
400	1.2×10^{-11}	1.4×10^{-11}	1.3×10^{-11}
450	1.3×10^{-11}	1.4×10^{-11}	1.5×10^{-11}
500	1.3×10^{-11}	1.5×10^{-11}	1.5×10^{-11}
Average	1.2×10^{-11}	1.3×10^{-11}	1.3×10^{-11}

Table 4.2 Measured stray capacitance from the sample holder in air from 500 °C to 300 °C.

To better understand the stray capacitance, we also built a model to calculate the stray capacitance from a holder composed of two parallel wires through the 4-bore alumina tube as shown in Figure 4.10. The required parameters are the diameter of Pt wires a = 0.5 mm, the distance between Pt wires d = 3.15 mm, the wire length l = 450 mm, and the relative dielectric constant of alumina $\varepsilon_r = 9.8$. Therefore, the stray capacitance between the Pt wires is determined to be

$$C = \frac{\pi \varepsilon_r \varepsilon_0 l}{\ln\left(\frac{d}{2a} + \sqrt{\frac{d^2}{4a^2} - 1}\right)} = 6.8 \times 10^{-11} F \qquad (4.1)$$

The value is consistent with what was measured on the bare electrode which showed that the long parallel Pt wires and short distance between wires are the main reason responsible for the large stray capacitance.

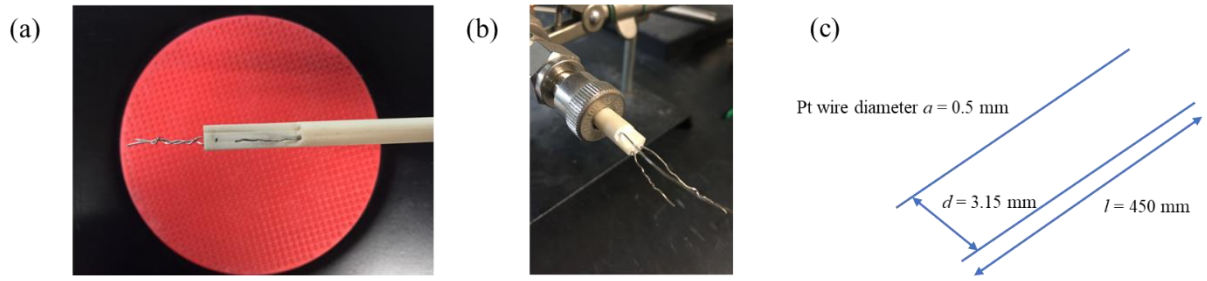

Figure 4.10 Sample holder setup and parallel wire model for stray capacitance calculation : (a) 4-bore alumina tube as sample holder, with (b) ceramic bond as sealant at the end; (c) parallel wire model for stray capacitance calculation.

The large stray capacitance in the system will influence the shape of impedance spectra in the Nyquist plot. The bulk and grain boundary arcs are not resolvable in the frequency domain when the stray capacitance is larger than the grain boundary capacitance (usually bulk capacitance is much smaller than that of grain boundary). In order to explore it further, we simulated a series of impedance spectra in which the stray capacitance was set to increases from infinitely small, ~0 to fairly large, $\sim 1\times10^{-11} F$, Figure 4.11. The latter is on the order of what we have measured from the bare device and sample holder. The equivalent circuit for simulation is performed using parameters calculated from the impedance data on fiberboard at 450 °C ($\varepsilon_r = 25$, $GB\,thickness = 29.9\,nm$, $\sigma_{bulk} = 6.65\times10^{-7} S/cm$, $\sigma_{gb} = 8.57\times10^{-10} S/cm$), and the typical geometry of fibers (6 μm thick and 20 μm long). The bulk and grain boundary capacitances are determined to be $3.1\times10^{-16} F$ and $2.1\times10^{-13} F$, respectively. We find that when the stray capacitance is smaller (at least 1 order) than the grain boundary capacitance, the bulk arc and grain boundary arc can be well separated. However, when the stray capacitance is comparable to the grain boundary capacitance or larger, the bulk and grain boundary arcs merge into a single arc and cannot be resolved. When the stray capacitance reaches $1.0\times10^{-11} F$, the impedance spectrum looked like a perfect single arc without any evidence of distinct bulk and grain boundary arcs. This explains well why the observed impedance of a bicrystal fiber is a single arc with a large stray capacitance of $1.3\times10^{-11} F$. Significantly, however, even though stray capacitance can change the shape of impedance spectra, it has no effect on total resistance. This behavior is leveraged to obtain values for the grain boundary resistance.

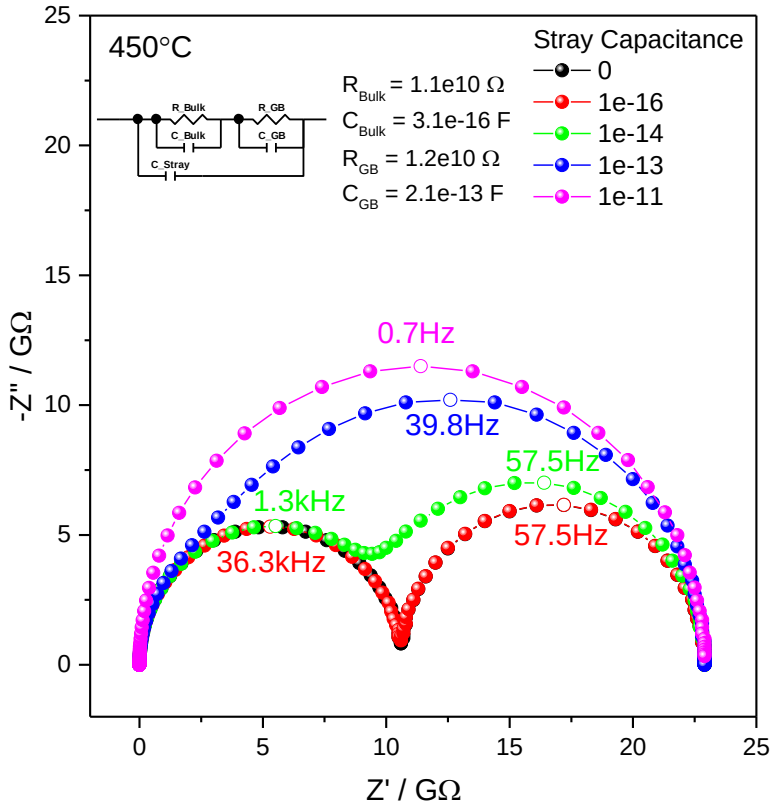

Figure 4.11 Simulation of stray capacitance effect on a single fiber impedance (6 μm thick and 20 μm long)

4.4.3 Simulation of Fiber Diameter Effect on Impedance

Since the stray capacitance resulting from the combined effect of the fabricated devices, sample holder and wiring is difficult to reduce, it is of value to consider whether the measurement can be improved by changing the sample geometry. Specifically, we consider the sample

dimensions required for the bulk and grain boundary capacitance to be larger than the stray capacitance.

The bulk and grain boundary capacitance are related to the geometry of fibers by

$$C_{bulk} = \varepsilon_r \varepsilon_0 \frac{A}{L}$$
$$C_{gb} = \varepsilon_r \varepsilon_0 \frac{A}{\delta} \qquad (4.2)$$

where ε_r (= 25) is relative dielectric constant, ε_0 is vacuum permittivity, A is cross-sectional area of fibers, L is the length of the fibers, and δ is the grain boundary thickness. We assume the relative dielectric constant of the grain boundary is equal to that of the bulk. Clearly, the capacitance will increase when the ratio of cross-sectional area to sample length increases. Therefore, we simulate a series of impedance spectra by changing the diameter of fibers from 4 μm to over 100 μm with a fixed length of 20 μm. The stray capacitance is set to be $1\times10^{-11} F$ throughout the simulation.

Example impedance spectra of bicrystal fibers with diameter increasing from 10 μm to 80 μm are shown in Figure 4.12. We observe that when diameter is larger than 50 μm, the impedance spectra tend to separate into two arcs. When the diameter reaches 80 μm, the bulk and grain boundary arcs are convincingly separated. The simulation result shows that increasing fiber diameter can reduce stray capacitance effect by increasing grain boundary capacitance over stray capacitance. However, when a fiber diameter increases to 80 μm with only 20 μm thickness, it is appropriate to address it as a disc rather than a fiber.

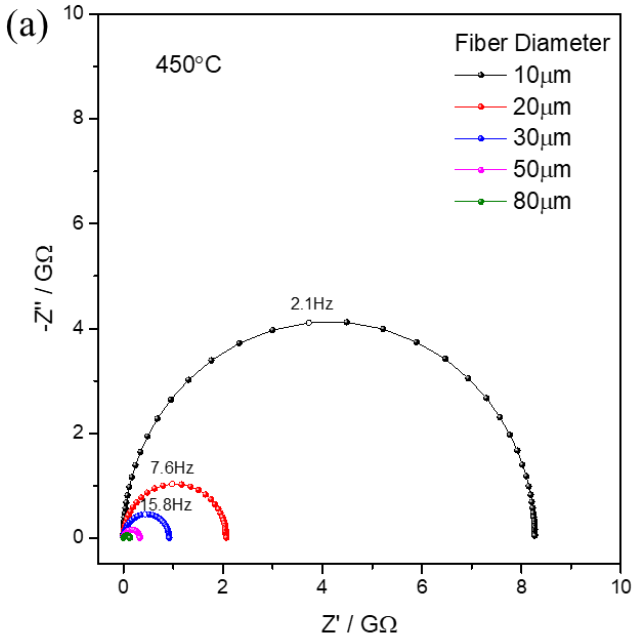
(a)
450°C
Fiber Diameter
10μm
20μm
30μm
50μm
80μm
2.1Hz
7.6Hz
15.8Hz
-Z'' / GΩ
Z' / GΩ
0
2
4
6
8
10

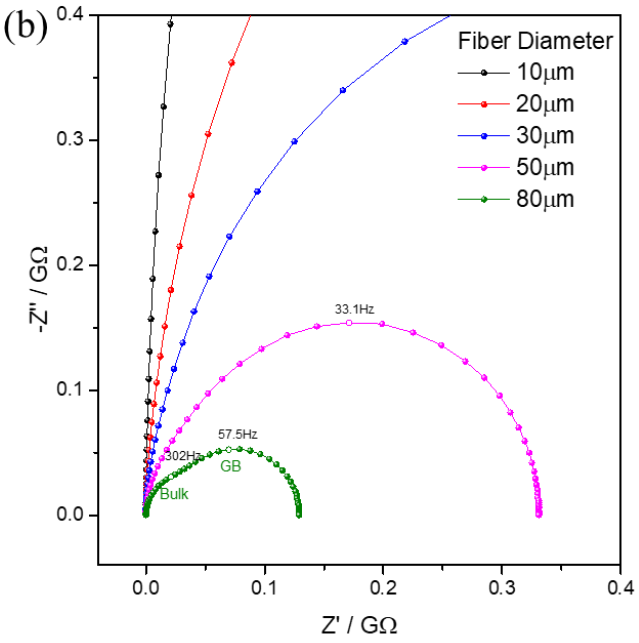
(b)
Fiber Diameter
10μm
20μm
30μm
50μm
80μm
33.1Hz
57.5Hz
302Hz
GB
Bulk
-Z'' / GΩ
Z' / GΩ
0.0
0.1
0.2
0.3
0.4

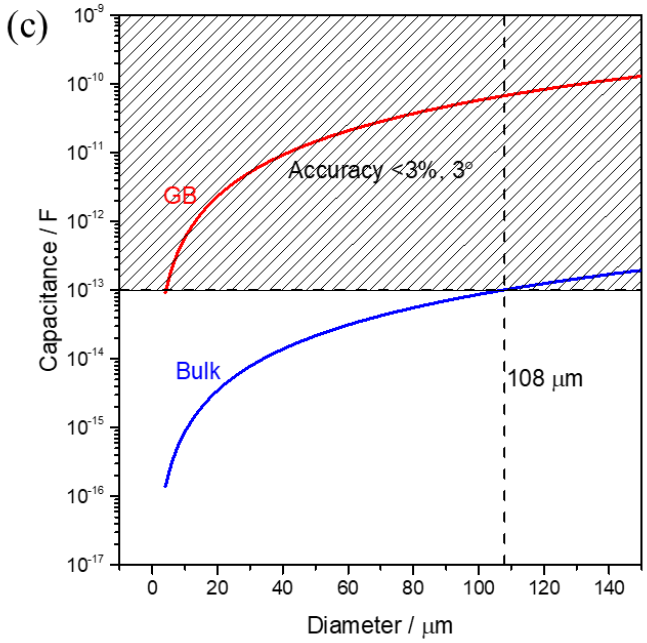

Figure 4.12 Simulation on impedance spectra on fibers with different geometry under synthetic air : (a) impedance spectra with fiber diameter 10-80 μm, and (b) expanded spectra; (c) bulk and grain boundary capacitance with fiber diameter increases. Simulation conditions: fiber length set to 20 μm, grain boundary thickness set to 29.9 nm, relative dielectric constant ε_r = 25 (measured from impedance on pellet sample), stray capacitance set to 10^{-11} F.

Even if we can find a smart way to successfully synthesis a micron disc with 80 μm diameter and 20 μm thickness, high-quality impedance spectra which produce well-separated bulk and grain boundary arcs cannot be guaranteed. This is due to the limited instrument performance of a real measurement. High quality instrument performance is limited within the accuracy contour

plot which varies by test conditions, model and manufacturer. For example, for a "fiber" with 80 μm in diameter and 20 μm in length, the resistance and capacitance of bulk and grain boundary are calculated to be:

$$R_{bulk} = 6.0 \times 10^{7}\,\Omega \qquad R_{gb} = 6.9 \times 10^{7}\,\Omega$$
$$C_{bulk} = 5.6 \times 10^{-14}\,F \qquad C_{gb} = 3.7 \times 10^{-11}\,F$$

This bulk and grain boundary resistance can be measured accurately with a Faraday cage. However, the bulk capacitance is on the order of $10^{-14}\,F$. According to the accuracy contour plot of the impedance analyzer Modulab X in Figure 4.13[80], the capacitance of $10^{-14}\,F$ is too small to be accurately measured through entire frequency with error >3% and >3°. The impedance analyzer can measure larger capacitance with higher accuracy in a wide frequency range. For the capacitance of $10^{-13}\,F$, accuracy of < 3% and < 3° error can be achieved through the frequency of 100 Hz to 0.1 MHz while for the capacitance of $10^{-11}\,F$ the frequency range expands to 0.1 Hz to 1 MHz with accuracy approaching to < 1% and < 1°.

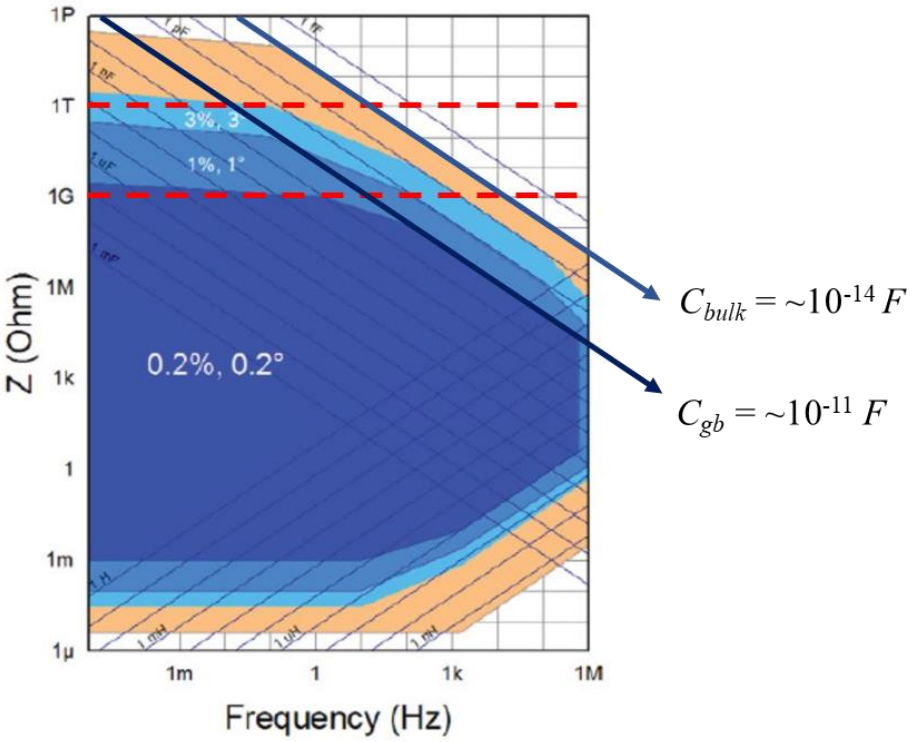

Figure 4.13 Accuracy contour plot of XM Modulab combined with Femto Ammeter and 2A Booster

To accurately measure bulk impedance in the high frequency range, the bulk capacitance must be the order of $10^{-13}F$ or even higher, which implies the fiber diameter needs to be larger than 80 μm. From the Figure 4.12 (c), to achieve the accuracy of < 3% and < 3°, the diameter of the fiber is calculated to be at least 108 μm. This additional requirement does not depend on stray capacitance but relies on instrument limit. In other words, even if we succeeded in removing stray capacitance by redesigning the ceramic holder, we still need a fiber with such a large diameter to obtain accurate measurement of the bulk capacitance.

4.4.4 Variability of Grain Boundary Impedance

After understanding the stray capacitance effect in our measurement, we found it was difficult to either reduce stray capacitance below grain boundary capacitance or increase fiber diameter above 108 μm. The goal of recovering well-separated bulk and grain boundary arcs may not be easily achieved. However, stray capacitance has no effect in the total resistance, and we can unveil the grain boundary resistance by subtracting the bulk resistance from the measured total resistance. The bulk resistance can be determined based on the bulk conductivity measured from the fiberboard. Therefore, we have the key for solving the mystery of single grain boundary resistance.

Six bicrystal fibers were measured by impedance spectroscopy from 600 °C to 300 °C in air. The area specific resistance of the grain boundaries is calculated by multiplying the grain boundary resistance with the cross-sectional area and is plotted in Figure 4.14 (a). The average area specific resistance of grain boundaries is calculated based on the measurement of the fiberboard by multiplying average grain boundary resistivity with grain boundary thickness. From the plot, we observe the variation of area specific grain boundary resistance of the six fibers is 2-3 orders of magnitude, suggesting that the space charge potential and space charge layer thickness varied as well.

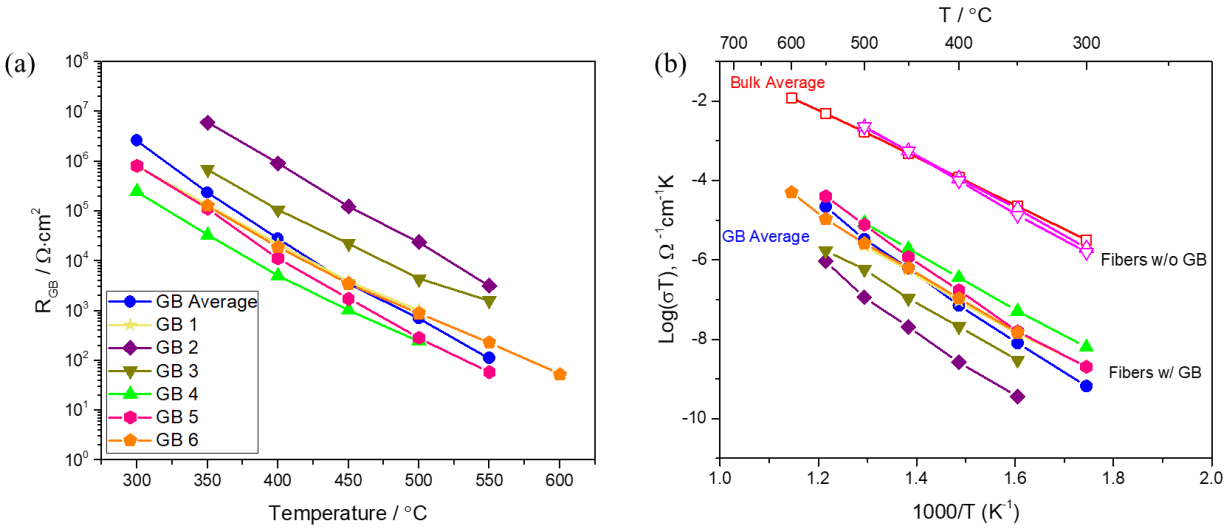

Figure 4.14 Single grain boundary resistance at the temperatures indicated : (a) area specific resistance of single grain boundaries; (b) Arrhenius plot of grain boundary conductivity at inversed temperatures.

The space charge potential $\Delta\varphi_0$ of single fibers can be calculated using the expression[8]

$$\frac{\sigma_{bulk}}{\sigma_{gb}} = \frac{e^{(ez\Delta\varphi_0/kT)}}{2ez\Delta\varphi_0 / kT} \qquad (4.3)$$

where, σ_{bulk} and σ_{gb} are the conductivity of bulk and grain boundary, *k* is Boltzmann constant, *T* is absolute temperature, and *z* is the effective valence of the mobile species (+2 in the case of oxygen vacancies). The expression is based on the Mott-Schottky model, and an assumption that, other than a depletion of carriers, the properties in the bulk and space charge regions are the same. In a typical measurement of a polycrystalline sample, the ratio of bulk to grain boundary

capacitance values can be used to obtain σ_{gb} from the impedance data. However, as discussed, the stray capacitance makes this approach impossible. The grain boundary thickness of each fiber is unknown, but uniquely relevant to its space charge potential by the expression:

$$\delta = 2\lambda = 2\sqrt{-\frac{\varepsilon_r \varepsilon_0 \Delta\varphi_0}{e z_d c_d}} \tag{4.4}$$

which follows from Mott-Schottky model where $\Delta\varphi_0$ is the space charge potential, ε_r (=25) is relative dielectric constant, ε_0 is vacuum permittivity, z_d is the effective valence of the dopant, e is the elementary charge, and c_d is the volumetric concentration of the dopant. The only unknown parameter is $z_d c_d$. However, when the impedance of the fiberboard is measured, the average space charge layer thickness $2\bar{\lambda}$ and average space charge potential $\Delta\overline{\varphi_0}$ were calculated to be 29.9 nm and 0.30 V, respectively based on brick layer model and Mott-Schottky model. These parameters can be used in the equation above to calculate the average charge concentration in the fiberboard which is also assumed to be true in single fibers.

$$(z_d c_d)^{fiberboard} = -\frac{\varepsilon_r \varepsilon_0 \Delta\overline{\varphi_0}}{e\bar{\lambda}^2},\ (z_d c_d)^{fiberboard} = (z_d c_d)^{fiber} \tag{4.5}$$

The Eq. (4.3) now is converted to

$$\frac{\sigma_{bulk}}{\sigma_{gb}} = \frac{\sigma_{bulk}}{\delta / ASR_{gb}} = \frac{e^{(ez\Delta\varphi_0/kT)}}{2ez\Delta\varphi_0 / kT} \tag{4.6}$$

where $\delta = 2\bar{\lambda}\sqrt{\frac{\Delta\varphi_0}{\overline{\Delta\varphi_0}}}$. Now, the only free variable is the space charge potential $\Delta\varphi_0$, and it can be determined from Eq. (4.6). Furthermore, the space charge layer thickness (=grain boundary thickness) and grain boundary conductivity can be obtained afterwards. The average space charge potential and space charge layer thickness over the measured temperature ranges in Figure 4.14 are shown in Figure 4.15.

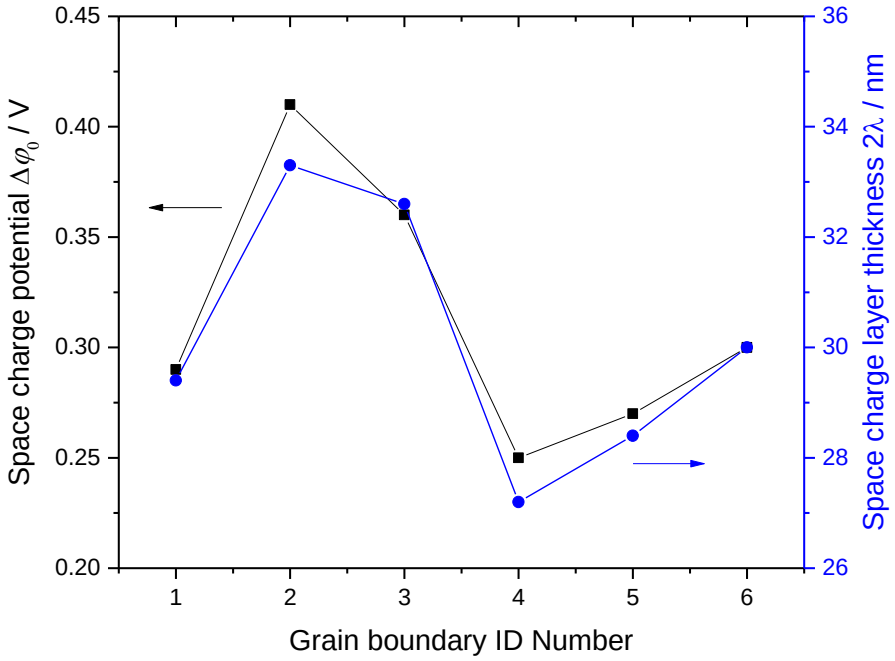

Figure 4.15 Average space charge potential and space charge layer thickness of the six characterized fibers over the measured temperature ranges inferred from a Mott-Schottky analysis.

The grain boundary conductivity with the dependence of temperature is plotted in Figure 4.14 (b). Activation energies are calculated from the slopes based on linear fitting to the data. The activation energies and space charge potentials are summarized in the Table 4.3 and are plotted in Figure 4.16. From the table, the high space charge potential corresponding to low grain boundary conductivity has large activation energy. High space charge potential and activation energy are related to large grain boundary barrier. GB2 has the highest potential 0.41 V among the six fibers with 1.71 ± 0.08 eV activation energy, which is 0.16 V higher than that of GB4 with 1.38 ± 0.02 eV activation energy. Even though there is only a slight difference in space charge potential, the grain boundary conductivity can be quite different following the Eq. (4.3). Compared to lower barrier GB4, the conductivity of higher barrier GB2 is 2-3 orders lower throughout the entire temperature range. In summary, the large variability in grain boundary conductivity is unveiled by impedance spectroscopy on single fibers.

Type	Diameter / μm	Length / μm	GB Activation Energy / eV	Space Charge Potential / V	GB thickness / nm
GB1	5.9	15.4	1.34 ± 0.04	0.29	29.4
GB2	4.3	21.2	1.71 ± 0.08	0.41	33.3
GB3	5.5	18.6	1.42 ± 0.03	0.36	32.6
GB4	4.8	16.0	1.38 ± 0.02	0.25	27.2
GB5	6.1	18.6	1.63 ± 0.05	0.27	28.4
GB6	6.2	18.5	1.50 ± 0.03	0.30	30.0
GB Average	1.75 cm	0.1 cm	1.68 ± 0.04	0.30	29.9
Bulk Average			1.19 ± 0.00	-	-
Fiber 1 without GB	4.7	15.1	1.33 ± 0.01	-	-
Fiber 2 without GB	5.0	14.8	1.40 ± 0.01	-	-

Table 4.3 Parameters summary for six fibers with normal grain boundaries and two fibers without grain boundaries

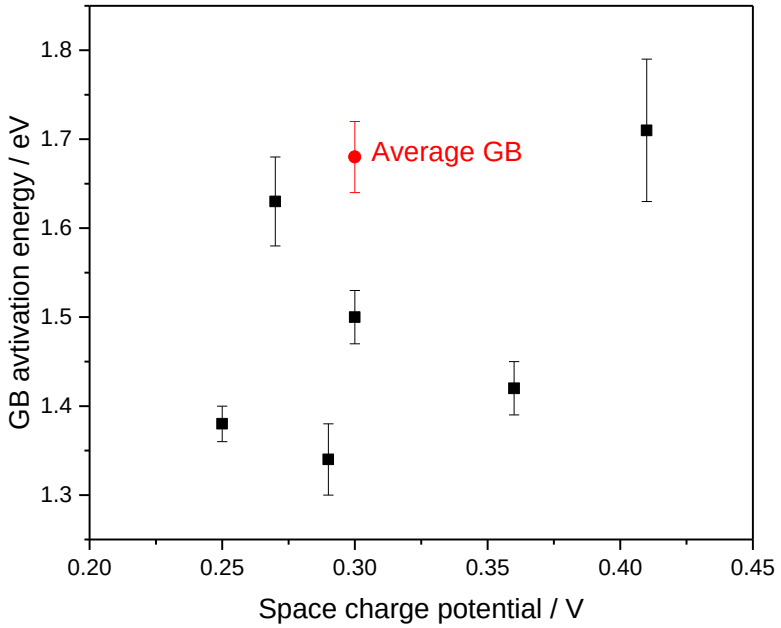

Figure 4.16 Plot of grain boundary activation energy vs. space charge potential of the six characterized bicrystal fibers.

4.4.5 Grain Boundary Bias Behavior and Current Saturation

Many studies have found that the electrical behavior of grain boundaries under bias is different from that of bulk in ionic conductors such as Sm doped CeO_2, Y doped CeO_2, Y doped $BaZrO_3$, etc[10,11,81–84]. When the bias across grain boundary V_{gb} is less than or comparable to the thermal voltage, $V_{th} = \frac{kT}{e}$, the electric current transporting through grain boundary is linear with V_{gb}, which shows the linear behavior of ohmic resistance. However, when the bias continues to increase over V_{th}, the relationship between electric current and bias follows power law, which is

$I_{gb} \propto V_{gb}^{n}$ where $n \simeq 2$. The mechanism for this bias behavior has been studied based on space charge theory[81,83]. To date, major studies have been focused on polycrystalline materials with a large number of grain boundaries. In these studies, the grain boundary behavior represents the average effect which ignores single grain boundary properties such as crystalline structure, misorientation, composition etc.

In order to explore electrical behavior of single grain boundaries, bias was directly applied from 0 V to 8 V on fibers which spanned only 20 μm between electrodes. This implies an ultrahigh electric field up to $4\times10^{3}\, V/cm$ on a single grain boundary, more than any other bias that has been reported in macroscopic samples. The bias ramp step is 10 mV/s with data collection every 5 mV.

Example $I_{gb}-V_{gb}$ plots of three bicrystal fibers, GB1, GB3 and GB5, from 550 °C to 350 °C in air are shown in Figure 4.17. Here the current density j_{gb} replaces the current I_{gb} in y-axis by considering the diameters of each fiber. Bias across grain boundary in x-axis is in the unit of V_{th}. GB3 has a higher space charge potential at 0.36 V while GB5 has a lower potential at 0.27 V. GB1 has a potential at 0.29 V similar to that of fiberboard. In the plot of GB3, the current through the grain boundary has linear relationship with the bias across grain boundary before $\frac{V_{gb}}{V_{th}} \sim 20$. When the bias increases beyond $\frac{V_{gb}}{V_{th}} = 20-30$, a power law relationship between j_{gb} and $\frac{V_{gb}}{V_{th}}$ with an exponent of ~2 appears. Moreover, the slope in high bias region slightly increases from 1.81 ± 0.02 to 2.67 ± 0.01 when the temperature decreases from 550 °C to 350 °C. The

transition point shows a shift toward higher bias when temperature decreases, which is due to the temperature dependence of $V_{th} = \frac{kT}{e}$. In contrast, lower space charge potential GB5 has slightly different grain boundary behavior, especially under high bias. The $I_{gb} - V_{gb}$ plot of this bicrystal fiber can be divided into three sections. The first section is a linear region $j_{gb} \propto \frac{V_{gb}}{V_{th}}$ which is seen when $\frac{V_{gb}}{V_{th}}$ is relatively low (e.g. $\frac{V_{gb}}{V_{th}} \leq 10$ at 450 °C). Then $j_{gb} \propto \left(\frac{V_{gb}}{V_{th}}\right)^n$ where $n \simeq 2$ when $\frac{V_{gb}}{V_{th}} = 20 - 30$ at 450 °C. Surprisingly, when $\frac{V_{gb}}{V_{th}}$ further increases, the linear relationship returns. This behavior suggests the current reaches a saturation regime. Such saturation behavior has been predicted[85,86] but rarely experimentally observed in ionic conductors. This is because macroscopic samples have millions of grain boundaries. Even though a high bias can be applied to the sample, the voltage across any individual grain boundary is small and can't bring the grain boundary to saturation. However, in our study, each fiber has only one grain boundary, and the grain boundary conductivity is ~3 orders less than the bulk conductivity. Most of the bias applied to the fiber drops on the grain boundary. Therefore, a large bias is achieved which drives the grain boundary towards saturation. However, current saturation is not found on GB1 and GB3 with higher space charge potential when the applied bias goes to maximum 8 V. This is probably because the applied bias is not large enough when the grain boundary barrier is high.

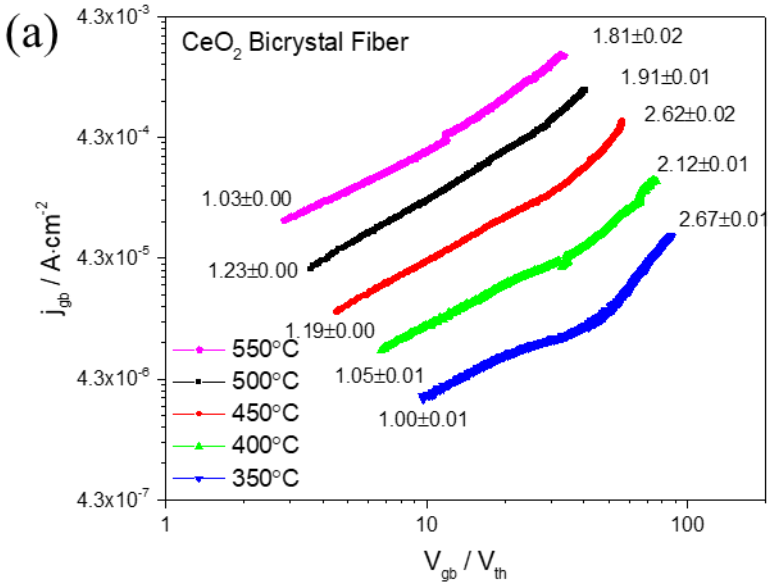
(a)
CeO2 Bicrystal Fiber
1.81±0.02
1.91±0.01
2.62±0.02
2.12±0.01
2.67±0.01
1.03±0.00
1.23±0.00
1.19±0.00
1.05±0.01
1.00±0.01
550°C
500°C
450°C
400°C
350°C
4.3x10-3
4.3x10-4
4.3x10-5
4.3x10-6
4.3x10-7
jgb / A·cm-2
1
10
100
Vgb / Vth

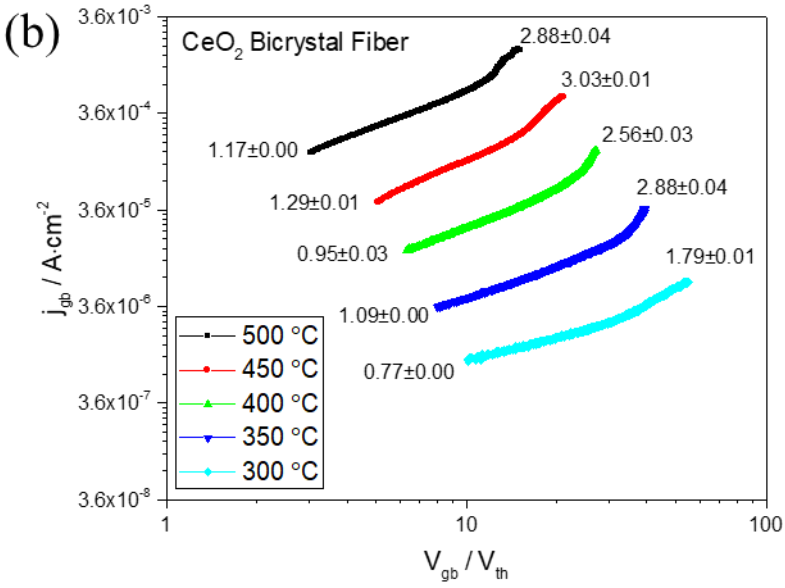
(b)
CeO2 Bicrystal Fiber
2.88±0.04
3.03±0.01
2.56±0.03
2.88±0.04
1.79±0.01
1.17±0.00
1.29±0.01
0.95±0.03
1.09±0.00
0.77±0.00
500 °C
450 °C
400 °C
350 °C
300 °C
3.6x10-3
3.6x10-4
3.6x10-5
3.6x10-6
3.6x10-7
3.6x10-8
jgb / A·cm-2
1
10
100
Vgb / Vth

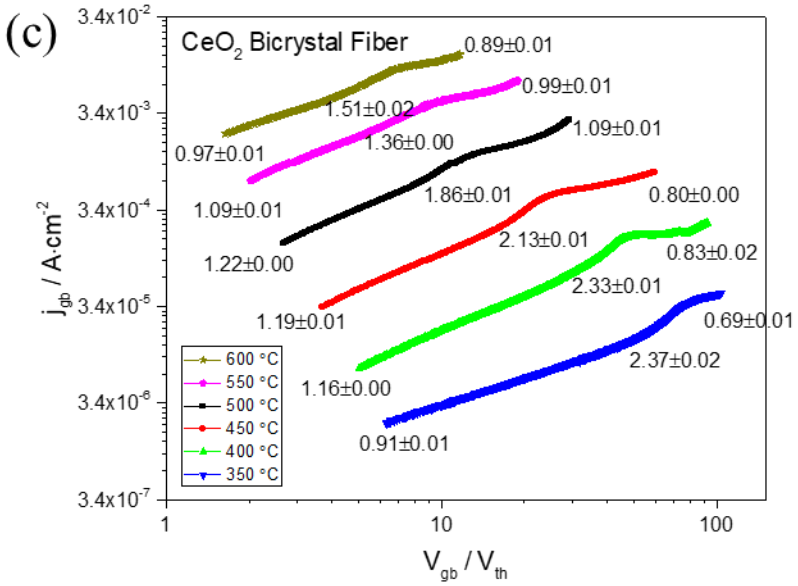

Figure 4.17 I_{gb} -V_{gb} plots of grain boundary with different space charge potentials at indicated bias : (a) GB3 with 0.36 V, (b) GB1 with 0.29 V and (c) GB5 with 0.27 V. Current density is used considering variability of fiber diameters.

4.5 Grain Boundary Misorientation and Composition

The misorientation of each fiber was measured by EBSD. One example grain boundary (GB1) is shown in Figure 4.18. The sample is tilted 70° from the horizontal plane to optimize both the contrast in the diffraction pattern and the fraction of electrons scattered from the sample. Since the fiber has a geometry of cylinder, the region for detection is limited and restricted to only the very top surface facing towards the detector. Other parts of the fiber are either blocked from the detector or from the incident electron beam. In the Figure 4.18 (c), only the top surface of the fiber is able to be characterized by EBSD. The region that can be indexed is only along the outline of the fiber. When the electron beam reaches the area below the top surface, the backscatter signal is blocked by the fiber itself and thus not collected by the detector.

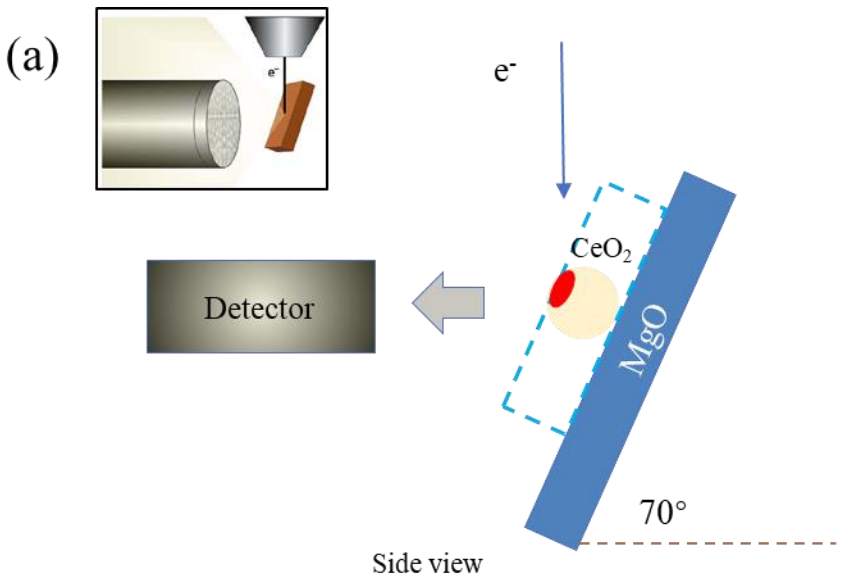

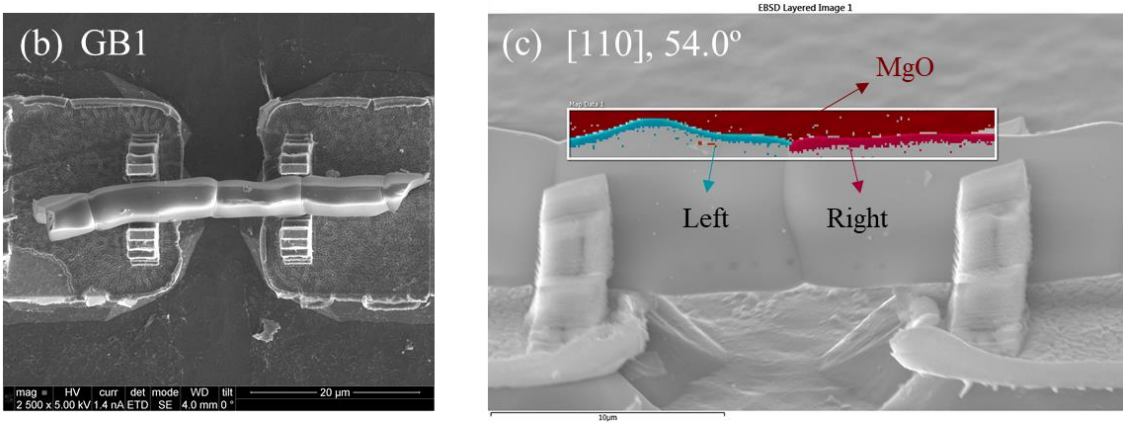

Figure 4.18 Electron backscatter diffraction analysis on a representative grain boundary : (a) schematic of measurement geometry; (b) scanning electron imaging of a fiber with a grain boundary GB1; (c) misorientation mapping on the top surface of the grain boundary.

The misorientation is recorded as Euler angles and converted to the pair of rotation axis/angle in the Table 4.4 below. The rotation axes of the six grain boundaries are not the same: there are a low index axis [100] of GB 6 and a high index axis [$\bar{4}$17] of GB3. Among the six fibers, GB1, GB4 and GB5 share the same rotation axis [110] with the rotation angles of GB1, 54.0º, higher than that of GB4, 7.7°. With higher rotation angles, the space charge potential of GB1 is 0.04 V higher than that of GB1, which implies a relationship between misorientation angles and space charge potential as shown in Figure 4.19.

Fiber Type	Space Charge Potential / V	Misorientation
GB1	0.29	[110] / 54.0°
GB2	0.41	[111] / 54.2°
GB3	0.36	[$\bar{4}$17] / 24.1°
GB4	0.25	[110] / 7.7°
GB5	0.27	[110] / 46.4°
GB6	0.30	[100] / 45.2°
GB Average	0.30	Random

Table 4.4 Misorientation determined by electron backscatter diffraction for six fibers with normal grain boundaries

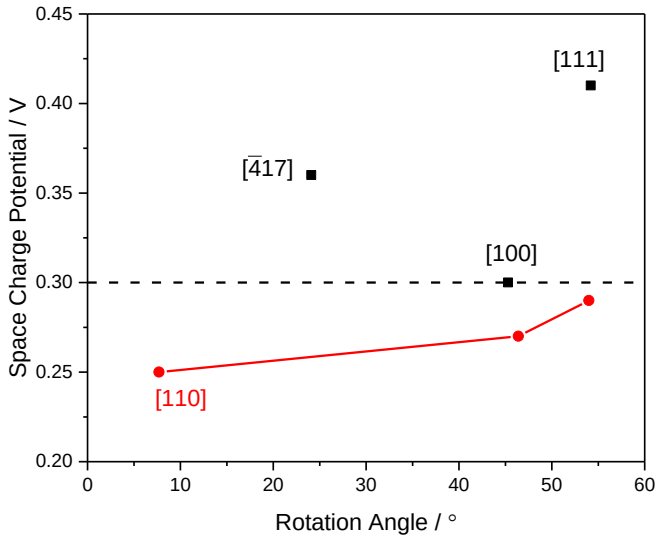

Figure 4.19 Plot of space charge potential vs. rotation angle with rotation axis as indicated.

To correlate misorientation with electrical properties of GB, we observe that the most resistive GB2 has misorientation of [111] / 54.2° while the least resistive GB 4 has misorientation of [110] / 7.7°. In contrast, GB6, which represents the average impedance, has misorientation of [100] / 45.2°. The relevant research on grain boundary conductivity or grain boundary energy dependence of misorientation in CeO_2 is rare. There are two studies on grain boundary energy and surface energy of twist and tilt grain boundaries in CeO_2 but are not very relevant to our work[87,88]. Our result provides an important missing link between misorientation and electrical properties of grain boundaries.

Chemical composition of the six fibers has not been characterized yet by SIMS. However, the grain boundary composition of random fibers was studied. We found a high variability in grain boundary composition. An example of grain boundary is shown in Figure 4.20. Al, Si, Mg and Ca are found to segregate at the grain boundary. Those species are not purposely doped in the fibers but are impurities possibly from the starting materials, transferring and/or sintering process. Another grain boundary with less segregation is shown in Figure 4.21. None of the previous impurities are found to be obviously segregated in this grain boundary. Even in the same fibers in Figure 4.22, the two grain boundaries have different segregation level. The finding from SIMS study is consistent with previous APT study on 0.2 at% doped CeO_2 used for electron holography where Al and Si are most likely responsible for positive space charge potential at grain boundaries in CeO_2. As interstitial impurities, the segregated Al and Si introduce positive charge $Al_i^{\cdots}$ and $Si_i^{\cdots\cdot}$ to the grain boundary core.

The segregation level related to grain boundary state depends on many factors. One of the most important factors may be misorientation. From what we learned from EBSD analysis, we found the misorientation of each fibers was unique causing varied grain boundary energy. The grain boundary energy in ionic oxides has been studied widely[14,63–65,87,89,90], which shows that the grain boundary energy will change in terms of misorientation. The varied grain boundary energy may be the driving force on species to segregate at grain boundary core.

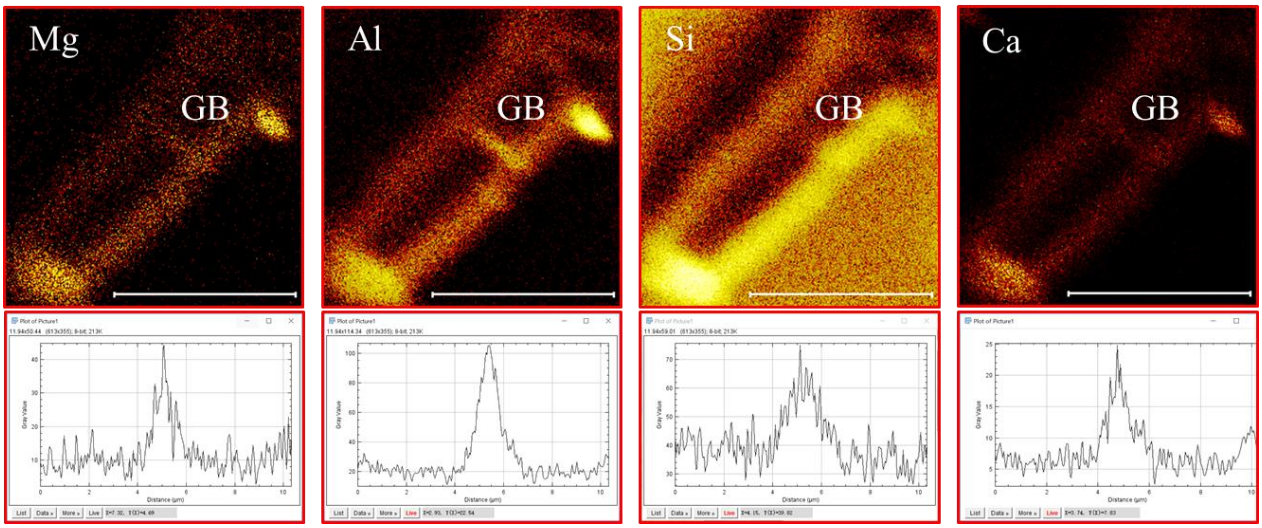

Figure 4.20 Chemical composition mapping across a representative heavily segregated grain boundary for Mg, Al, Si and Ca. Scale bar = 10 μm.

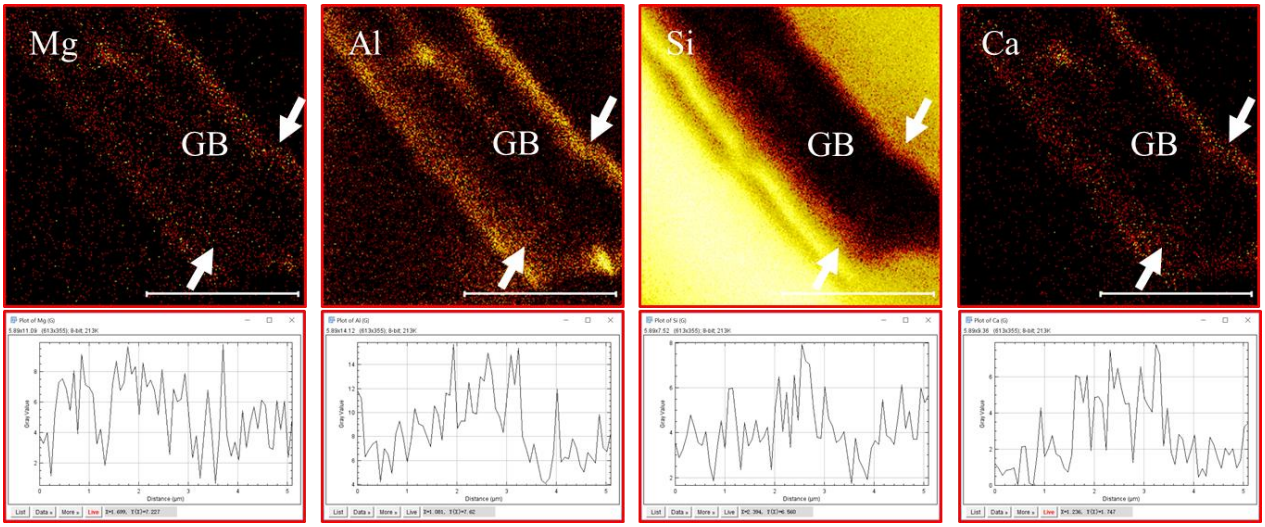

Figure 4.21 Chemical composition mapping across a representative lightly segregated grain boundary for Mg, Al, Si and Ca. Scale bar = 10 μm.

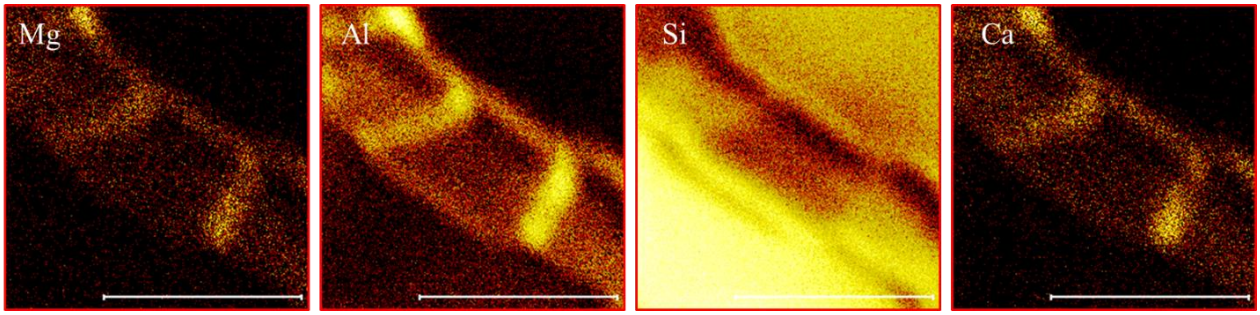

Figure 4.22 Chemical composition mapping across a representative fiber with two grain boundaries for Mg, Al, Si and Ca. Scale bar = 10 μm.

4.6 Beyond Undoped Ceria Fibers & Fiberboard

I would like to take the last chance to discuss impurities and impedance in nominal undoped ceria synthesized in the lab and literature. Hopefully my input on this topic will be helpful to someone after me.

In the past five years, many ceria samples were synthesized, either doped or undoped, with starting powders, either high purity or regular. All the samples are sintered at high temperatures to achieve large density, approaching to the theoretical value. All the nominally undoped ceria samples were found to have different bulk and grain boundary conductivities. The difference in bulk conductivity can be as high as 4 orders which is definitely beyond measurement error. The large difference must be due to something else, of which the most possible factor, an impurity, is addressed here.

Even if the synthesized sample is nominally undoped, an impurity in the sample can convert the sample from undoped to doped. Impurities can be from anywhere such as starting powders, grinding, sieving, ball milling, beakers, pressing, combustion boats, furnaces, etc. In some steps, impurities can be controlled carefully. For example, during the high temperature sintering process, extra powders fully covering the sintered pellet in the combustion boat protect the pellet from the contamination from the furnace and the combustion boat. Furthermore, selection of starting powders is vital to the impurity level in the final products. However, we only have the option to select products from different suppliers but are not able to control the impurity level or further purify the existing starting powders.

The starting CeO_2 powders in the lab are usually not of high purity. Most of them are 99.9% trace from Aldrich Chemistry with impurities $\leq$ 1500 ppm based on the provided Product

Specification. The 1500 ppm impurity level implies a small amount of contamination over the entire sample. However, if we consider grain boundary segregation, then the segregated impurities may be substantial when the enrichment factor is high. There are other CeO_2 powders of high purity which are 99.995% with impurities ≤ 55 ppm. These are the cleanest ceria powders found online and used in the synthesis of 0.2 at% Sm doped CeO_2 (SDC02) for electron holography and atom probe tomography study. The third CeO_2 samples are the fiberboard with purity > 99%. All the three sample were sintered at high temperature with similar density and grain size as shown in Figure 4.23 and in the Table 4.5 below.

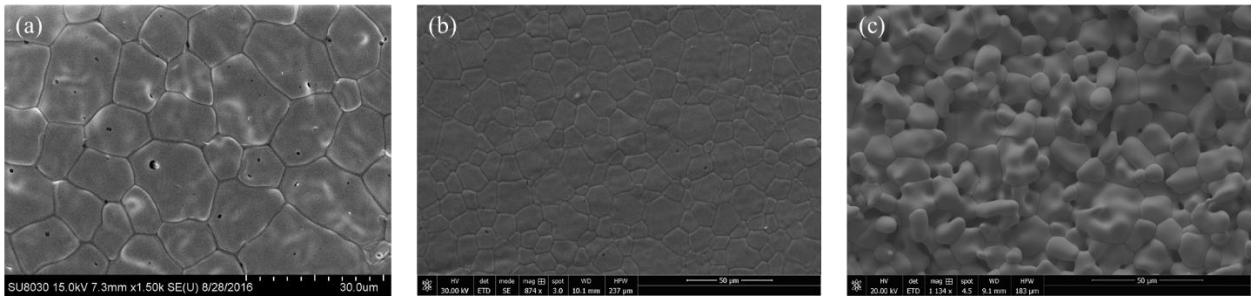

Figure 4.23 Scanning electron microscopy image of three ceria samples : (a) undoped ceria (grain size 10.0 ± 0.6 µm) made from starting powders CeO_2 >99.9%, Aldrich Chemistry; (b) 0.2% Sm doped cerium oxide (grain size 12.5 ± 1.2 µm) made from starting powder CeO_2 >99.995% and Sm_2O_3 >99.999%, Aldrich Chemistry; (c) ceria fiberboard (grain size 10.9 ± 0.7 µm) made from CeO_2 fibers >99%, Zircar, Inc.

	Undoped Ceria	0.2 at% Sm doped CeO2	Fiberboard
Impurity level	99.9%, ≤ 1500 ppm	CeO_2 (99.995%, ≤ 55 ppm), Sm_2O_3 (99.999%, ≤ 15ppm	99%
Grain size	10.7 ± 0.6 μm	10.9 ± 0.7 μm	12.5 ± 1.2 μm
Relative density	>96%	>96%	>96%
Sintering temperature	1550 °C	1500 °C	1500 °C

Table 4.5 Structure and impurity level of the three ceria samples

The bulk conductivity of the three samples is shown in Figure 4.24 (a). We can clearly observe that the high purity ceria powders even doped with 0.2 at% Sm has the lowest bulk conductivity, which is slightly lower than that of the fiberboard, but almost 4 orders lower than that of undoped ceria made of powders with 99.9% purity at 300 °C. When the temperature increases, the difference in bulk conductivity becomes smaller and vanishes when extrapolated beyond 700 °C. We also compare the bulk conductivity of some ceria samples in the literature. One is undoped ceria made of 99.999% high purity CeO_2 powders and the other is 0.1 at% Y doped CeO_2. Both samples have higher conductivity compared to that of the fiberboard and SDC02 by extrapolating data to low temperature range ~300 °C.

At such a low temperature, the electronic conductivity is extremely low and can be ignored. The only charge carrier is oxygen vacancy, the concentration of which is dominated by dopant level. In nominal undoped ceria, those species such as alkaline earth elements Mg, Ca, Ba which are common impurities in CeO_2, can replace Ce atoms and sit on Ce sites generating oxygen vacancies by

$$MO \xrightarrow{CeO_2} M''_{Ce} + V_O^{\bullet\bullet} + O_O^{\times} \qquad (4.7)$$

Thus, high bulk conductivity means the high substitutional species in the bulk region. Among the ceria samples, SDC02 shows the lowest impurity level in the bulk.

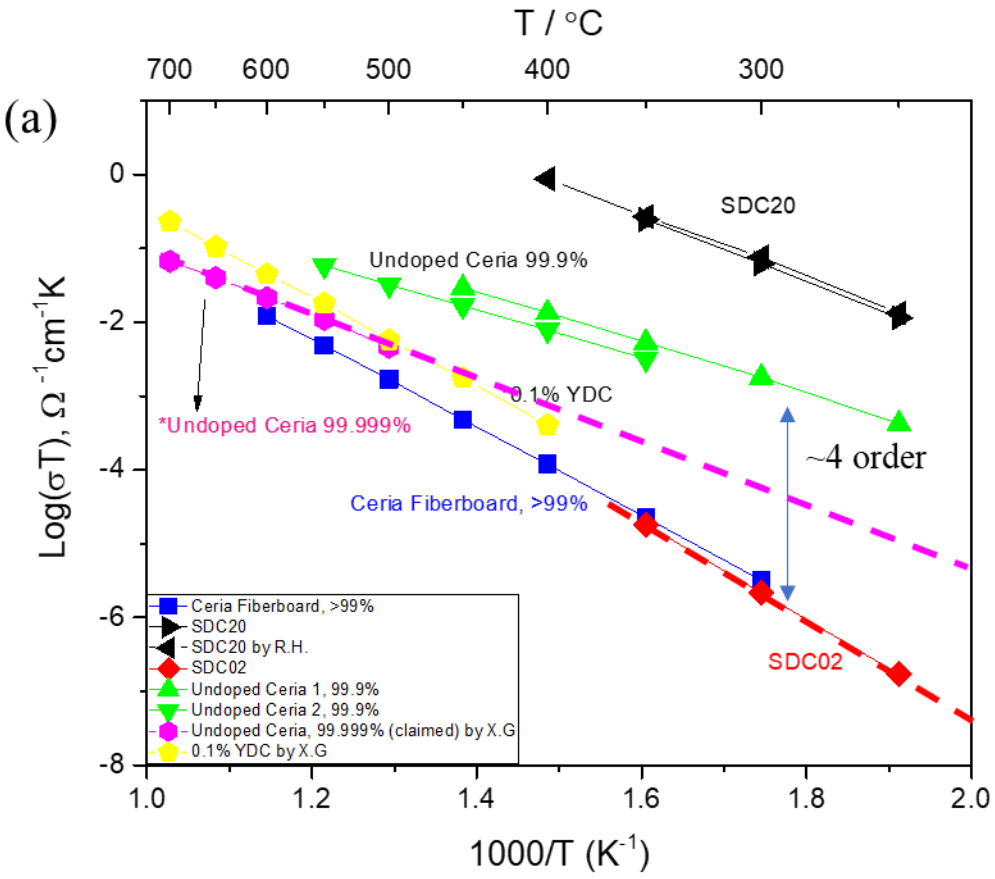

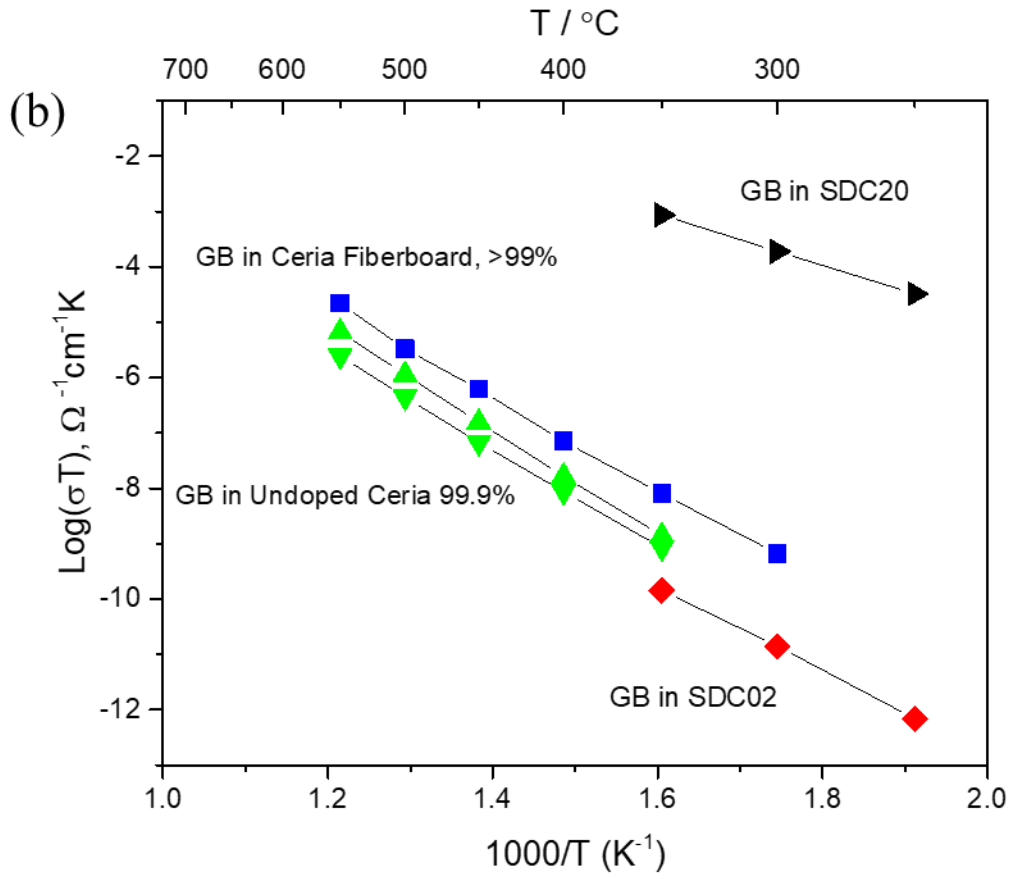

Figure 4.24 Arrhenius plot of ceria samples : (a) bulk conductivity, and (b) grain boundary conductivity of a series of ceria samples including undoped ceria (99.9%), undoped ceria (99.999%), 0.1 at% Y doped ceria, 0.2 at% Sm doped ceria and 20 at% Sm doped ceria either in the lab or literature.

Grain boundary conductivity is also plotted in Figure 4.24 (b). We observe that the grain boundary conductivity of the fiberboard is the highest while the SDC02 is the lowest among the three ceria samples. The difference is as high as 2 orders in grain boundary conductivity. The

reason for such a large difference is unknown. From our previous finding, the impurity level at grain boundary core is responsible for electrical conductivity of grain boundary. Those interstitial cation impurities such as Al and Si will introduce a positive charge to grain boundary core. While those substitutional cations such as alkaline earth elements counter the positive charge at grain boundary core. Therefore, to explain the difference in grain boundary conductivity requires the knowledge of impurity amounts and defect type. However quantitative measurement of impurity level and determination of defect type at grain boundary core is difficult due to the need for high spatial resolution and high sensitivity. To further study and compare impurity level in different ceria samples is beyond the scope of study and will be passed down to others who are interested. Besides, whether the impurity level at grain boundaries is correlated with grain boundary misorientation is unclear and still needs more investigation. But the most important point I would like to bring up here is that the impurity effect especially at grain boundaries may determine the electrical performance at low temperatures. Even if those impurities are in the level of ppm and generally ignored, it is vital to electrical conductivity of ionic oxides at intermediate or even low temperatures, the ideal operation temperature range that solid-state fuel cells aim for.

4.7 Summary

In this work, we develop a type of novel device and design an ultrahigh impedance station for in-plane impedance measurements at elevated temperatures. The resistance of this device without loading samples exceeds 800 GΩ at 450 ºC in air while resistance as high as TΩ and capacitance as low as 0.01 pF are measurable by using the ultrahigh impedance station. The coating of mixed conductors SCN20 on top of Pt layers effectively decreases the electrochemical resistance between the interface of electrodes and samples, which assists in unveiling single grain boundary resistances. Large variability in grain boundary conductivity is observed, which is up to 3 orders among the six fibers with the space charge potential spanning from 0.25 V to 0.41 V. This puts into question the traditional grain boundary transport theory in polycrystalline materials which assumes a single value of space charge potential. Misorientation is obtained by electron backscatter diffraction on each fiber, which shows that all fibers have unique misorientations, even though they are from the same batch materials. The fiber of [111] / 54.2 º has the lowest conductivity while the fiber of [110] / 7.7° has the highest. Si, Al, Ca and Mg are found segregated at grain boundary cores with variation from grain boundary to grain boundary. This matches our finding from the APT study on 0.2 at% Sm doped ceria which also found grain boundary segregation of those species. Similarly, we believe that Si and Al segregation at grain boundary cores are responsible for positive charged grain boundaries while divalent substitutional dopants are able to counter the charge of tetravalent interstitial impurities and therefore increase grain boundary conductivity in ceria. The device developed here facilitates the observation of current saturation across grain boundaries. This validates the space charge theory with a unique point of evidence.

5 Summary & Conclusion

In this study, the charge transport of single grain boundaries was investigated in ceria, one of the most significant oxide electrolytes in materials community, with systematic studies on the electrical conductivity, misorientation and chemical composition. We primarily tackle two problems which are usually overlooked in ionic materials due to a lack of relevant experimental evidence. The first problem is the assumption that every grain boundary is approximately the same with single values of properties since many models of material behavior rely on this assumption. The second problem is the origin of grain boundary barriers to ionic conductivity.

With results from electron holography and impedance spectroscopy on single grain boundaries in ceria, we have strong evidence to show that a large variability of grain boundary properties is directly observed in terms of space charge potential varying from 1.15 V to negligible, and ionic conductivity of many orders difference. Selected area diffraction and electron backscatter diffraction show that each grain boundary has unique misorientation. This misorientation study found that large tilt angle grain boundaries favor high boundary barriers. Atom probe tomography and secondary ion mass spectroscopy study on single grain boundaries reveal that Al, Si and alkaline earth species enriched at grain boundary cores at different levels. All of the direct observation has put into question models of material behavior that assume uniform grain boundary properties in samples. Furthermore, the direct grain boundary study unveils the space charge origins in solid-state ionic materials. Si, Al and those interstitial impurities at the grain boundaries may be entirely responsible for the high interfacial positive charge. Segregation of trivalent and divalent substitutional dopants to the grain boundaries is able to counter the charge of interstitial impurities, and may be the reason for the substantially higher grain boundary conductivity in

heavily doped fluorites than in those which are lightly doped, as studied here. Thus the space charge origin is primarily driven by a chemical cause intead of thermochemical one. This provides us with clear guidance on how to tune interfacial charge and transport in ionic materials: substitutional dopants that reduce space charge potential favor positive carrier transport while interstital impurities that increase space charge potential assist negative carrier transport. We are hoping this study will assist in many research fields of the future that can utilize grain boundary engineering such as intermediate temperature fuel cells, solid-state batteries, thermochemical cells, memristors and electrocatalysts.

References

1. Luo, J. Interfacial engineering of solid electrolytes. *Journal of Materiomics* **1**, 22–32 (2015).
2. Zhang, T. S., Ma, J., Chan, S. H., Hing, P. & Kilner, J. A. Intermediate-temperature ionic conductivity of ceria-based solid solutions as a function of gadolinia and silica contents. *Solid State Sciences* **6**, 565–572 (2004).
3. Kim, S., Kim, S. K., Khodorov, S., Maier, J. & Lubomirsky, I. On determining the height of the potential barrier at grain boundaries in ion-conducting oxides. *Phys. Chem. Chem. Phys.* **18**, 3023–3031 (2016).
4. Lei, Y., Ito, Y., Browning, N. D. & Mazanec, T. J. Segregation Effects at Grain Boundaries in Fluorite-Structured Ceramics. *Journal of the American Ceramic Society* **85**, 2359–2363 (2002).
5. N. Vikrant, K. S., C. Chueh, W. & Edwin García, R. Charged interfaces: electrochemical and mechanical effects. *Energy & Environmental Science* **11**, 1993–2000 (2018).
6. Maier, J. Ionic conduction in space charge regions. *Progress in Solid State Chemistry* **23**, 171–263 (1995).
7. Sato, K. Probing Charge-State Distribution at Grain Boundaries Varied with Dopant Concentration for Ceria Ceramics. *J. Phys. Chem. C* **121**, 20407–20412 (2017).
8. Guo, X. & Maier, J. Grain Boundary Blocking Effect in Zirconia: A Schottky Barrier Analysis. *J. Electrochem. Soc.* **148**, E121–E126 (2001).
9. Fleig, J. & Maier, J. Finite-Element Calculations on the Impedance of Electroceramics with Highly Resistive Grain Boundaries: I, Laterally Inhomogeneous Grain Boundaries. *Journal of the American Ceramic Society* **82**, 3485–3493 (1999).

10. Guo, X. & Waser, R. Electrical properties of the grain boundaries of oxygen ion conductors: Acceptor-doped zirconia and ceria. *Progress in Materials Science* **51**, 151–210 (2006).
11. Gregori, G., Merkle, R. & Maier, J. Ion conduction and redistribution at grain boundaries in oxide systems. *Progress in Materials Science* **89**, 252–305 (2017).
12. Kim, S., Fleig, J. & Maier, J. Space charge conduction: Simple analytical solutions for ionic and mixed conductors and application to nanocrystalline ceria. *Physical Chemistry Chemical Physics* **5**, 2268–2273 (2003).
13. Rodewald, S., Fleig, J. & Maier, J. Microcontact Impedance Spectroscopy at Single Grain Boundaries in Fe-Doped SrTiO3 Polycrystals. *Journal of the American Ceramic Society* **84**, 521–530 (2001).
14. Zhang, Z. *et al.* Comparative studies of microstructure and impedance of small-angle symmetrical and asymmetrical grain boundaries in SrTiO3. *Acta Materialia* **53**, 5007–5015 (2005).
15. R. Diercks, D. *et al.* Three-dimensional quantification of composition and electrostatic potential at individual grain boundaries in doped ceria. *Journal of Materials Chemistry A* **4**, 5167–5175 (2016).
16. Eguchi, K., Setoguchi, T., Inoue, T. & Arai, H. Electrical properties of ceria-based oxides and their application to solid oxide fuel cells. *Solid State Ionics* **52**, 165–172 (1992).
17. Mogensen, M., Sammes, N. M. & Tompsett, G. A. Physical, chemical and electrochemical properties of pure and doped ceria. *Solid State Ionics* **129**, 63–94 (2000).
18. Gellings, P. J. *Handbook of Solid State Electrochemistry*. (CRC Press, 2019).

19. Nernst, W. On the electrolytic conduction of solid bodies at high temperatures. *Z. Electrochem* **6**, 41–43 (1899).
20. Chueh, W. C. & Haile, S. M. Ceria as a Thermochemical Reaction Medium for Selectively Generating Syngas or Methane from H2O and CO2. *ChemSusChem* **2**, 735–739 (2009).
21. Kaneko, H. *et al.* Reactive ceramics of CeO2–MOx (M=Mn, Fe, Ni, Cu) for H2 generation by two-step water splitting using concentrated solar thermal energy. *Energy* **32**, 656–663 (2007).
22. Chueh, W. C. *et al.* High-Flux Solar-Driven Thermochemical Dissociation of CO2 and H2O Using Nonstoichiometric Ceria. *Science* **330**, 1797–1801 (2010).
23. Tuller, H. L. & Nowick, A. S. Doped Ceria as a Solid Oxide Electrolyte. *J. Electrochem. Soc.* **122**, 255–259 (1975).
24. Fergus, J., Hui, R., Li, X., Wilkinson, D. P. & Zhang, J. *Solid Oxide Fuel Cells: Materials Properties and Performance*. (CRC Press, 2016).
25. Wang, D. Y. & Nowick, A. S. The "grain-boundary effect" in doped ceria solid electrolytes. *Journal of Solid State Chemistry* **35**, 325–333 (1980).
26. Bauerle, J. E. Study of solid electrolyte polarization by a complex admittance method. *Journal of Physics and Chemistry of Solids* **30**, 2657–2670 (1969).
27. Beekmans, N. M. & Heyne, L. Correlation between impedance, microstructure and composition of calcia-stabilized zirconia. *Electrochimica Acta* **21**, 303–310 (1976).
28. Schouler, E., Giroud, G. & Kleitz, M. Applications selon Bauerle du tracé des diagrammes d'admittance complexe en électrochimie des solides - II. — Étude de la conductivité de la zircone stabilisée à l'yttrium. *J. Chim. Phys.* **70**, 1309–1316 (1973).

29. Gerhardt, R. & Nowick, A. S. Grain-Boundary Effect in Ceria Doped with Trivalent Cations: I, Electrical Measurements. *Journal of the American Ceramic Society* **69**, 641–646 (1986).

30. Chiang, Y. -M., Lavik, E. B., Kosacki, I., Tuller, H. L. & Ying, J. Y. Defect and transport properties of nanocrystalline CeO2−x. *Appl. Phys. Lett.* **69**, 185–187 (1996).

31. Tschöpe, A., Sommer, E. & Birringer, R. Grain size-dependent electrical conductivity of polycrystalline cerium oxide: I. Experiments. *Solid State Ionics* **139**, 255–265 (2001).

32. Kim, S. & Maier, J. On the Conductivity Mechanism of Nanocrystalline Ceria. *J. Electrochem. Soc.* **149**, J73–J83 (2002).

33. Gouy, M. Sur la constitution de la charge électrique à la surface d'un électrolyte. *J. Phys. Theor. Appl.* **9**, 457–468 (1910).

34. Chapman, D. L. LI. A contribution to the theory of electrocapillarity. *The London, Edinburgh, and Dublin Philosophical Magazine and Journal of Science* **25**, 475–481 (1913).

35. Göbel, M. C., Gregori, G. & Maier, J. Numerical calculations of space charge layer effects in nanocrystalline ceria. Part I: comparison with the analytical models and derivation of improved analytical solutions. *Phys. Chem. Chem. Phys.* **16**, 10214–10231 (2014).

36. Lee, J.-S. & Kim, D.-Y. Space-charge concepts on grain boundary impedance of a high-purity yttria-stabilized tetragonal zirconia polycrystal. *Journal of Materials Research* **16**, 2739–2751 (2001).

37. Thompson, A. W. Calculation of true volume grain diameter. *Metallography* **5**, 366–369 (1972).

38. Lehmann, M. & Lichte, H. Electron Holography. in *Transmission Electron Microscopy* (eds. Carter, C. B. & Williams, D. B.) 215–232 (Springer International Publishing, 2016). doi:10.1007/978-3-319-26651-0_8

39. Larson, D. J., Prosa, T. J., Ulfig, R. M., Geiser, B. P. & Kelly, T. F. *Local Electrode Atom Probe Tomography*. (Springer New York, 2013). doi:10.1007/978-1-4614-8721-0

40. Vespucci, S. *et al.* Digital direct electron imaging of energy-filtered electron backscatter diffraction patterns. *Phys. Rev. B* **92**, 205301 (2015).

41. *Electron backscatter diffraction in materials science*. (Springer, 2009).

42. Cloete, K. J. Ion Beam, Synchrotron Radiation, and Related Techniques in Biomedicine: Elemental Profiling of Hair. *Accelerator Physics - Radiation Safety and Applications* (2018). doi:10.5772/intechopen.72076

43. Wang, F., Zhou, Q., He, T., Li, G. & Ding, H. Novel SrCo1−yNbyO3−δ cathodes for intermediate-temperature solid oxide fuel cells. *Journal of Power Sources* **195**, 3772–3778 (2010).

44. Zhou, W., Jin, W., Zhu, Z. & Shao, Z. Structural, electrical and electrochemical characterizations of SrNb0.1Co0.9O3−δ as a cathode of solid oxide fuel cells operating below 600°C. *International Journal of Hydrogen Energy* **35**, 1356–1366 (2010).

45. Cascos, V., Martínez-Coronado, R. & Alonso, J. A. New Nb-doped SrCo1−xNbxO3−δ perovskites performing as cathodes in solid-oxide fuel cells. *International Journal of Hydrogen Energy* **39**, 14349–14354 (2014).

46. Huang, S. *et al.* Cerium and niobium doped SrCoO3−δ as a potential cathode for intermediate temperature solid oxide fuel cells. *Journal of Power Sources* **251**, 357–362 (2014).

47. Langford, R. M., Wang, T.-X. & Ozkaya, D. Reducing the resistivity of electron and ion beam assisted deposited Pt. *Microelectronic Engineering* **84**, 784–788 (2007).
48. Louie, M. Electrocatalysis in solid acid fuel cells. (California Institute of Technology, 2011).
49. Modulab XM Electrochemical System User Guide. (2014).
50. Guo, X., Sigle, W. & Maier, J. Blocking Grain Boundaries in Yttria-Doped and Undoped Ceria Ceramics of High Purity. *Journal of the American Ceramic Society* **86**, 77–87 (2003).
51. C. Chueh, W., Yang, C.-K., M. Garland, C., Lai, W. & M. Haile, S. Unusual decrease in conductivity upon hydration in acceptor doped, microcrystalline ceria. *Physical Chemistry Chemical Physics* **13**, 6442–6451 (2011).
52. Yeh, T. C., Perry, N. H. & Mason, T. O. Nanograin Composite Model Studies of Nanocrystalline Gadolinia-Doped Ceria. *Journal of the American Ceramic Society* **94**, 1073–1078 (2011).
53. Williams, D. B. & Carter, C. B. *Transmission electron microscopy: a textbook for materials science*. (Springer, 2008).
54. Haile, S. M., West, D. L. & Campbell, J. The role of microstructure and processing on the proton conducting properties of gadolinium-doped barium cerate. *Journal of Materials Research* **13**, 1576–1595 (1998).
55. J. Avila-Paredes, H., Choi, K., Chen, C.-T. & Kim, S. Dopant-concentration dependence of grain-boundary conductivity in ceria: A space-charge analysis. *Journal of Materials Chemistry* **19**, 4837–4842 (2009).
56. Tschöpe, A., Kilassonia, S. & Birringer, R. The grain boundary effect in heavily doped cerium oxide. *Solid State Ionics* **173**, 57–61 (2004).

57. Rau, W. D., Schwander, P., Baumann, F. H., Höppner, W. & Ourmazd, A. Two-Dimensional Mapping of the Electrostatic Potential in Transistors by Electron Holography. *Phys. Rev. Lett.* **82**, 2614–2617 (1999).

58. Wang, Y. G. & Dravid, V. P. Determination of electrostatic characteristics at a 24°, [001] tilt grain boundary in a SrTiO3 bicrystal by electron holography. *Philosophical Magazine Letters* **82**, 425–432 (2002).

59. Ravikumar, V., Rodrigues, R. P. & Dravid, V. P. Space-Charge Distribution across Internal Interfaces in Electroceramics Using Electron Holography: II, Doped Grain Boundaries. *Journal of the American Ceramic Society* **80**, 1131–1138 (1997).

60. Ravikumar, V., Rodrigues, R. P. & Dravid, V. P. Direct Imaging of Spatially Varying Potential and Charge across Internal Interfaces in Solids. *Phys. Rev. Lett.* **75**, 4063–4066 (1995).

61. McCartney, M. R. & Gajdardziska-Josifovska, M. Absolute measurement of normalized thickness, t/λi, from off-axis electron holography. *Ultramicroscopy* **53**, 283–289 (1994).

62. Malis T., Cheng S. C. & Egerton R. F. EELS log-ratio technique for specimen-thickness measurement in the TEM. *Journal of Electron Microscopy Technique* **8**, 193–200 (2005).

63. Shibata, N., Oba, F., Yamamoto, T. & Ikuhara §, Y. Structure, energy and solute segregation behaviour of [110] symmetric tilt grain boundaries in yttria-stabilized cubic zirconia. *Philosophical Magazine* **84**, 2381–2415 (2004).

64. Bokov, A. *et al.* Energetic design of grain boundary networks for toughening of nanocrystalline oxides. *Journal of the European Ceramic Society* **38**, 4260–4267 (2018).

65. Harbison, T. ANISOTROPIC GRAIN BOUNDARY ENERGY FUNCTION FOR URANIUM DIOXIDE. 272

66. Rittner, J. D. & Seidman, D. N. ⟨110⟩ symmetric tilt grain-boundary structures in fcc metals with low stacking-fault energies. *Phys. Rev. B* **54**, 6999–7015 (1996).

67. Rohrer, G. S. Grain boundary energy anisotropy: a review. *J Mater Sci* **46**, 5881–5895 (2011).

68. Harscher, A. & Lichte, H. Experimental study of amplitude and phase detection limits in electron holography. *Ultramicroscopy* **64**, 57–66 (1996).

69. Lichte, H. Performance limits of electron holography. *Ultramicroscopy* **108**, 256–262 (2008).

70. Kirkland, E. J. *Advanced Computing in Electron Microscopy*. (Springer US, 1998). doi:10.1007/978-1-4757-4406-4

71. Rez, D., Rez, P. & Grant, I. Dirac–Fock calculations of X-ray scattering factors and contributions to the mean inner potential for electron scattering. *Acta Cryst A, Acta Cryst Sect A, Acta Crystallogr A, Acta Crystallogr Sect A, Acta Crystallogr A Found Crystallogr, Acta Crystallogr Sect A Found Crystallogr* **50**, 481–497 (1994).

72. Seidman, D. N. Three-Dimensional Atom-Probe Tomography: Advances and Applications. *Annual Review of Materials Research* **37**, 127–158 (2007).

73. Hellman, O. C., Vandenbroucke, J. A., Rüsing, J., Isheim, D. & Seidman, D. N. Analysis of Three-dimensional Atom-probe Data by the Proximity Histogram. *Microscopy and Microanalysis* **6**, 437–444 (2000).

74. Ge, L., Ni, Q., Cai, G., Sang, T. & Guo, L. Improving SiO2 impurity tolerance of Ce0.8Sm0.2O1.9: Synergy of CaO and ZnO in scavenging grain-boundary resistive phases. *Journal of Power Sources* **324**, 582–588 (2016).

75. Cho, P.-S. *et al.* Effect of CaO concentration on enhancement of grain-boundary conduction in gadolinia-doped ceria. *Journal of Power Sources* **183**, 518–523 (2008).

76. Kim, D. K. *et al.* Mitigation of Highly Resistive Grain-Boundary Phase in Gadolinia-Doped Ceria by the Addition of SrO. *Electrochem. Solid-State Lett.* **10**, B91–B95 (2007).

77. Cho, Y. H. *et al.* Enhancement of grain-boundary conduction in gadolinia-doped ceria by the scavenging of highly resistive siliceous phase. *Acta Materialia* **55**, 4807–4815 (2007).

78. Shannon, R. D. Revised effective ionic radii and systematic studies of interatomic distances in halides and chalcogenides. *Acta Cryst A* **32**, 751–767 (1976).

79. Souza, E. C. C., Chueh, W. C., Jung, W., Muccillo, E. N. S. & Haile, S. M. Ionic and Electronic Conductivity of Nanostructured, Samaria-Doped Ceria. *J. Electrochem. Soc.* **159**, K127–K135 (2012).

80. ModuLab XM ECS Brochure. (2015).

81. K. Kim, S., Khodorov, S., Lubomirsky, I. & Kim, S. A linear diffusion model for ion current across blocking grain boundaries in oxygen-ion and proton conductors. *Physical Chemistry Chemical Physics* **16**, 14961–14968 (2014).

82. K. Kim, S., Khodorov, S., Chen, C.-T., Kim, S. & Lubomirsky, I. How to interpret current–voltage relationships of blocking grain boundaries in oxygen ionic conductors. *Physical Chemistry Chemical Physics* **15**, 8716–8721 (2013).

83. Iguchi, F., Chen, C.-T., Yugami, H. & Kim, S. Direct evidence of potential barriers at grain boundaries in Y-doped BaZrO3 from dc-bias dependence measurements. *J. Mater. Chem.* **21**, 16517–16523 (2011).

84. Guo, X., Mi, S. & Waser, R. Nonlinear Electrical Properties of Grain Boundaries in Oxygen Ion Conductors: Acceptor-Doped Ceria. *Electrochem. Solid-State Lett.* **8**, J1–J3 (2005).

85. Hölbling, Th. & Waser, R. Simulation of the charge transport across grain boundaries in p-type SrTiO3 ceramics under dc load: Debye relaxation and dc bias dependence of long-term conductivity. *Journal of Applied Physics* **91**, 3037–3043 (2002).

86. Shirpour, M., Merkle, R., T. Lin, C. & Maier, J. Nonlinear electrical grain boundary properties in proton conducting Y–BaZrO 3 supporting the space charge depletion model. *Physical Chemistry Chemical Physics* **14**, 730–740 (2012).

87. Chernatynskiy, A., Bai, X.-M. & Gan, J. Systematic investigation of the misorientation- and temperature-dependent Kapitza resistance in CeO2. *International Journal of Heat and Mass Transfer* **99**, 461–469 (2016).

88. Vyas, S., W. Grimes, R., H. Gay, D. & L. Rohl, A. Structure, stability and morphology of stoichiometric ceria crystallites. *Journal of the Chemical Society, Faraday Transactions* **94**, 427–434 (1998).

89. De Souza, R. A. *et al.* Electrical and Structural Characterization of a Low-Angle Tilt Grain Boundary in Iron-Doped Strontium Titanate. *Journal of the American Ceramic Society* **86**, 922–928 (2003).

90. De Souza, R. A. *et al.* Electrical resistance of low-angle tilt grain boundaries in acceptor-doped SrTiO3 as a function of misorientation angle. *Journal of Applied Physics* **97**, 053502 (2005).